

The Probe of Inflation and Cosmic Origins

A Space Mission Study Report
December, 2018

Principal Investigator:

Steering Committee:

Executive Committee:

Contributors:

Endorsers:



{fig:PICOsci_prob}

The Probe of Inflation and Cosmic Origins

A Space Mission Study Report December, 2018

Principal Investigator: Shaul Hanany

Steering Committee: Charles Bennet, Scott Dodelson, Lyman Page

Executive Committee: **May be incomplete** Jamie Bock, Julian Borrill, Brendan Crill, Mark Devlin, Raphael Flauger, Shaul Hanany (PI), William Jones, Lloyd Knox, Al Kogut, Charles Lawrence (ex-officio), Clem Pryke, Amy Trangsrud (ex-officio)

Authors

Marcelo Alvarez
Peter Ashton
Jonathan Aumont
Ranajoy Banerji
Belen Barreiro
James G. Bartlett
Soumen Basak
Nicholas Battaglia
Jamie Bock
Kim Boddy
Matteo Bonato
Julian Borrill
Francois Boulanger
Blakesley Burkhart
David Chuss
Susan E. Clark
Brendan Crill

Jacques Delabrouille
Joy Didier
Olivier Doré
Alexander van Engelen
Josquin Errard
Tom Essinger-Hileman
Stephen Feeney
Jeff Fillippini
Laura Fissel
Raphael Flauger
Vera Gluscevic
Kris Gorski
Dan Green
Brandon Hensley
Diego Herranz
Colin Hill

Eric Hivon
Johannes Hubmayr
Brad Johnson
William Jones
Terry Jones
Lloyd Knox
Al Kogut
Charles Lawrence
Alex Lazarian
Zack Li
Mathew Madhavacheril
Jean-Baptiste Melin
Mattia Negrello
Giles Novak
Roger O'Brient
Chris Paine
Tim Pearson

Levon Pogosian
Clem Pryke
Mathieu Remazeilles
Graca Rocha
Marcel Schmittfull
Ian Stephens
Brian Sutin
Maurizio Tomasi
Amy Trangsrud
Eleonora Di Valentino
Flavien Vansyngel
Qi Wen
Siyao Xu
Karl Young
Andrea Zonca
Gianfranco De Zotti

Endorsers

Zeeshan Ahmed
Jason Austermann
Darcy Barron
Karim Benabed
Federico Bianchini
J. Richard Bond
Xingang Chen
Jens Chluba
Francis-Yan Cyr-Racine
Tijmen de Haan
Shirokoff, Erik

Aurelien Fraisse
Piacentini Francesco
Bouchet FranÃ§ois
Silvia Galli
Ken Ganga
Tuhin Ghosh
Jon E. Gudmundsson
Marc Kamionkowski
Reijo Keskitalo
Rishi Khatri
Ely Kovetz

Daniel Lenz
Marilena Loverde
Carlos Martins
Silvia Masi
Lorenzo Moncelsi
Pavel Motloch
Tony Mroczkowski
Pavel Naselsky
Federico Nati
Elena Orlando
Giuseppe Puglisi

Christian Reichardt
Anirban Roy
Maria Salatino
Sarah Shandera
Anže Slosar
Aritoki Suzuki
Grant Teply
Matthieu Tristram
Scott Watson
Edward J. Wollack

Contents

1	Executive Summary	1
2	Science	4
2.1	Introduction	4
2.2	Science Objectives	6
2.2.1	Fundamental Physics	6
2.2.2	Cosmic Structure Formation and Evolution	12
2.2.3	Galactic Structure and Star Formation	18
2.3	Cosmological Legacy Surveys	21
2.3.1	Early phases of galaxy evolution	21
2.3.2	Early phases of cluster evolution	23
2.3.3	Additional products of PICO surveys	24
2.4	Complementarity with Other Surveys and with Sub-Orbital Measurements	24
2.4.1	Complementarity with Astrophysical Surveys in the 2020s	24
2.4.2	Complementarity with Sub-Orbital Measurements	25
2.5	Signal Separation	26
2.5.1	PICO Foreground Separation Methodology	28
2.5.2	Results and Discussion	28
2.6	Systematic Uncertainties	29
2.6.1	List of Systematics	31
2.6.2	Absolute polarization angle calibration	31
2.6.3	Gain Stability	32
2.6.4	Far Sidelobe Pickup	33
2.6.5	Key Findings	33
2.7	Measurement Requirements	34
3	Instrument	36
3.1	Telescope	36
3.2	Focal plane	37
3.2.1	21–462 GHz bands	37
3.2.2	555–799 GHz bands	39
3.2.3	Sensitivity	39
3.3	Detector readout	39
3.4	Thermal	41
3.4.1	cADR sub-kelvin cooling	41
3.4.2	4 K Cooler	41
3.4.3	Radiative cooling	44
3.5	Instrument integration and test	44
4	Design reference mission	45
4.1	Concept of operations	45
4.1.1	Mission design and launch	46
4.1.2	Survey design	46

4.2	Ground segment	47
4.3	Spacecraft	47
4.3.1	Attitude determination and control	48
5	Technology maturation	49
5.1	Three-color antenna-coupled bolometers	49
5.2	High-frequency direct absorbing arrays	50
5.3	Environmental testing	51
5.4	Multiplexing	51
5.5	Simulation	52
5.6	Technology descopes	52
5.7	Enhancing technologies	52
6	Project management, heritage, risk, and cost	54
6.1	PICO Study Participants	54
6.2	Project management plan	54
6.3	Heritage	55
6.4	Risk assessment	55
6.4.1	Pre-mission risks	55
6.4.2	Development risks	56
6.4.3	Operations risks	56
6.5	Mission cost	56
6.5.1	Instrument cost	58

1 Executive Summary

The cosmic microwave background (CMB) comes to us from the furthest reaches of the observable Universe, and its photons experience all of cosmic history. Created when the Universe was a hotter, simpler place, CMB photons probe fundamental physics, provide exquisite measurements of the constituents of the cosmos, and tests of relativity. On their journey they feel the impact of the gravitational potentials formed from the assembling cosmic web of superclusters, clusters and galaxies. They interact with the ionized gas in the inter- and circum-galactic medium, gas that eventually fuels star and galaxy formation. Superposed upon the CMB is the emission from multiple extragalactic sources and from our Galaxy. All of this leaves an imprint which sensitive measurements can disentangle so that CMB studies impact essentially every aspect of cosmology and astrophysics.

Building upon a long legacy of successful measurements, the next decade holds tremendous potential for new, exciting CMB discoveries. Such discoveries, delivered by the Probe of Inflation and Cosmic Origins (PICO), promise to be revolutionary, affecting physics, astrophysics, and cosmology. PICO is an imaging polarimeter that will scan the sky for 5 years with 21 frequency bands spread between 21 and 800 GHz; see Table 2.1. It will produce 10 independent full sky surveys of intensity and polarization with a final combined-map noise level equivalent to 3250 *Planck* missions for the baseline required specifications, though in our current best-estimate (CBE) it would perform as 6400 *Planck* missions. It will produce the first ever full sky polarization maps at frequencies above 350 GHz, and it will have diffraction limited resolution of 1' at 800 GHz.

With these unprecedented capabilities, unmatched by any other existing or proposed platform, PICO will have compelling and broad science deliverables. The mission will respond to 7 science objectives (SOs), which are listed in Table 2.2. Delivering this set was the basis for selecting PICO's design and for setting instrument requirements. But PICO's science reach is far broader than the baseline set.

PICO could determine the energy scale of inflation and give a first, direct probe of quantum gravity; this is SO1 (§ 2.2.1). If the signal is not detected PICO will constrain broad classes of inflationary models, and exclude at 10σ models for which the characteristic scale in the potential is the Planck scale (SO1 and SO2). The combination of PICO with LSST can constrain features in the inflationary potential, the field content during inflation and could rule out all models of slow-roll single-field inflation, marking a watershed in studies of inflation.

The mission will have a deep impact on particle physics by measuring the expected sum of the neutrino masses in two independent ways, each with at least 4σ confidence, rising to 7σ if the sum is near 0.1 eV (SO3). **this is not quite right; the cluster constraint will require follow up, so the second way is not from the mission** The measurements will either detect or strongly constrain deviations from the standard model of particle physics by counting the number of light particles in the early universe at an energy range that is up to 400 times higher than available today **this needs to be modified** (SO4). The data will constrain dark matter candidates by pushing down *Planck* constraints on the dark matter annihilation cross section by a factor of 25, specifically at low energy scales that are not accessible to direct detection experiments. The data will probe the existence of cosmic fields that could give rise to cosmic birefringence. **what about dark energy?**

PICO will transform our knowledge of the structure and evolution of the universe. It will measure the redshift at which the universe reionized, impacting physical models describing when and how the first luminous objects formed (SO5). **more quantitative regarding τ ?** It will make a map

{acro:CMB}

of the projected matter throughout the universe with a signal-to-noise ratio exceeding 500. This will constrain the mass of dark matter halos hosting galaxies, groups, and clusters from the present day to the very first such objects. [more quantitative?](#) The map will be cross-correlated with other next-decade galaxy surveys, such as LSST, to measure the growth of large-scale structure with sub-percent precision. An extraordinary amount of information about the role of 'energetic feedback' on structure formation will come from correlating PICO's map of the thermal Sunyaev-Zel'dovich effect with galaxy and lensing maps from WFIRST and LSST. The correlation – forecast to have a signal-to-noise of 3000 with LSST weak lensing – will enable measurements in dozens of tomographic redshift bins, giving extraordinarily detailed information about the evolution of thermal energy injection over cosmic time.

Magnetic fields thread galaxies and affect their structure and evolution, but the origins of these magnetic fields is a hotly debated question. PICO will test whether galactic magnetic fields have been seeded by primordial magnetic fields of cosmic origin. It will map the entire Milky Way in polarization with unprecedented detail at many frequency bands. Such maps are not planned by any other survey, and can not be produced other than in space. From these unique maps we will map the Galactic magnetic field structure elucidating the relative roles of turbulence and magnetic fields in the observed low star formation efficiency, and we will strongly constrain the properties of the diffuse interstellar medium, including dust grain composition, temperature and emissivities (SO6 and SO7).

The cosmic infrared background (CIB) encodes information from star-formation, obscured or unobscured, across cosmic time and PICO will improve upon existing measurements of CIB clustering by an order of magnitude [what is CIB clustering?](#) By discovering 150,000 clusters, 50,000 proto-clusters (up to $z=4.5$), and 4500 strongly lensed galaxies (up to $z=5$), PICO will enable a unique view into early galaxy and cluster evolution. The window PICO provides because of its high frequency bands is entirely unique and not available to any other experiment. PICO's sub-mm maps will provide ancillary information (including polarization) for all future measurements anywhere on the sky. [dark energy science removed; put back?](#)

This scientifically ground-breaking mission is based on technologies that are being used actively today by ground- and balloon-based experiments, but over a more restricted range of frequency band. These technologies will continue to mature by a host of recently funded sub-orbital activities well before the mission's Phase-A. Section ?? now here include: [single instrument, simple scan; need funding for foregrounds and systematics](#)

All the implementation aspects are mature, benefiting from thousands of person-years of experience studying the sky at these wavelengths. These span over more than 50 years of mapping the CMB and include three enormously successful space missions. This combined experience unambiguously shows that the unlimited frequency coverage and thermally benign environment aboard a space-based platform give unparalleled capability to separate the combination of galactic and cosmological signals and to control systematic uncertainties. These qualities, which are critical ingredients for any next-decade experiment, make PICO the optimal platform for a next generation CMB experiment.

Table 2.1: Mission Specifications

Bands	GHz	21	25	30	36	43	52	62	75	90	108	129	155	186	223	268	321	385	462	555	666	799	Combined Map Depth
FWHM	arcmin	38.4	32.0	28.3	23.6	22.2	18.4	12.8	10.7	9.5	7.9	7.4	6.2	4.3	3.6	3.2	2.6	2.5	2.1	1.5	1.3	1.1	μK_{CMB} arcmin
Baseline Polarization	μK_{CMB} arcmin	23.9	18.4	12.4	7.9	7.9	5.7	5.4	4.2	2.8	2.3	2.1	1.8	4.0	4.5	3.1	4.2	4.5	9.1	45.8	177.2	1047	Baseline
Map Depth	Jy/sr	8.3	10.9	11.8	12.9	19.5	23.8	45.4	58.3	59.3	77.3	96.0	119.1	433.1	604.2	433.4	577.8	429.1	551.1	1580	2075	2884	CBE
Cost	\$100M	Mission length 5 years				Launch mass 2147 kg				Total power 1526 W													

{tab:specs}

Table 2.2: Science Traceability Matrix (STM)

Science Goals from NASA Science Plan	Science Objectives	Scientific Measurement Requirements						Instrument (single instrument, single mode)				Mission Functional Requirements
		Model Parameters		Physical Parameters		Observables		Functional Requirements	Projected Performance			
<i>Explore how the Universe began (Inflation)</i>	SO1. Probe the physics of the big bang by detecting the energy scale at which inflation occurred if it is above 4×10^{15} GeV, or place an upper limit if it is below (§ 2.2.1)	Tensor-to-scalar ratio r : $\sigma(r) = 1 \times 10^{-4}$ at $r = 0$; $r < 5 \times 10^{-4}$ at 5σ confidence level ^a	CMB polarization BB power spectrum for modes $2 < \ell < 300$ to cosmic-variance limit, and CMB lensing power spectrum for modes $2 < \ell < 1000$ to cosmic-variance limit	Linear polarization across $60 < v < 300$ GHz over entire sky; foreground separation requires $20 < v < 800$ GHz	Frequency coverage: central frequencies v_c from 20 to 800 GHz.	Sun-Earth L2 orbit with Sun-Probe-Earth $< 15^\circ$.	5 yr survey with $\geq 95\%$ survey efficiency.					
	SO2. Probe the physics of the big bang by excluding classes of potentials as the driving force of inflation (§ 2.2.1, Fig. 2.2)	Spectral index (n_s) and its derivative (n_{run}): $\sigma(n_s) < 0.0015$; $\sigma(n_{\text{run}}) < 0.002$	CMB polarization BB power spectrum for modes $2 < \ell < 1000$ to cosmic-variance limit	Intensity and linear polarization across $60 < v < 220$ GHz over the entire sky	Frequency resolution: $\Delta v/v_c = 25\%$. Sensitivity: See Table 3.2. Combined instrument weight of $< 0.87 \mu\text{K}_{\text{CMB}} \sqrt{\text{s}}$.	Frequency coverage: See Table 3.2. 21 bands with v_c from 21 to 799 GHz.	Full sky survey: Spin instrument at 1 rpm; boresight 69° off spin axis; spin axis 26° off anti-Sun line, precessing $360^\circ / 10\text{hr}$.					
<i>Discover how the Universe works (neutrino mass and N_{eff})</i>	SO3. Determine the sum of neutrino masses. (§ 2.2.1, Fig. 2.4)	Sum of neutrino masses (Σm_ν): $\Sigma m_\nu < 15$ meV with DESI or Euclid ^b	CMB polarization BB power spectrum for modes $2 < \ell < 4000$ to cosmic-variance limit; CMB intensity maps (to give Compton Y map from which we extract clusters)	Intensity and linear polarization across $60 < v < 220$ GHz over the entire sky; foreground separation enveloped by SO1	Angular resolution [for delensing and foreground separation]: $\text{FWHM} = 6.2' \times (155 \text{ GHz}/v_c)$. Sampling rate: $(3/\text{BeamFWHM}) \times (336'/\text{s})$. Angular resolution: See Table 3.2.	Frequency resolution: $\Delta v/v_c = 25\%$. Sensitivity: See Table 3.2. Combined instrument weight of $0.43 \mu\text{K}_{\text{CMB}} \sqrt{\text{s}}$.	Pointing control: Spin axis $60'$ (3σ , radial). Spin 1 ± 0.1 rpm (3σ)	Pointing stability: Drift of spin axis $< 1'/1\text{min}$ (3σ , radial); jitter $< 20''/20\text{ ms}$ (3σ , radial).				
	SO4. Tightly constrain the thermalized fundamental particle content of the early Universe (§ 2.2.1, Fig. 2.3)	Number of neutrino effective relativistic degrees of freedom (N_{eff}): $\sigma(N_{\text{eff}}) < 0.03$	CMB temperature and EE polarization power spectra $2 < \ell < 4000$ to cosmic-variance limit	Intensity and linear polarization across $60 < v < 300$ GHz over entire sky; foreground separation enveloped by SO1	Sampling rate: $(3/\text{BeamFWHM}) \times (336'/\text{s})$. Angular resolution: See Table 3.2.	FWHM = $6.2' \times (155 \text{ GHz}/v_c)$; $1.1'$ for $v_c = 799$ GHz.	Pointing knowledge (telescope boresight): $10''$ (3σ , each axis) from spacecraft attitude $1''$ (3σ , each axis) final reconstructed	Return and process instrument data: 1.5 Tbits/day (after 4× compression)				
<i>Explore how the Universe evolved (reionization)</i>	SO5. Distinguish between models that describe the formation of the earliest stars in the Universe (§ 2.2.2, Fig. 2.5)	Optical depth to reionization (τ): $\sigma(\tau) < 0.002$	CMB polarization EE power spectrum for modes $2 < \ell < 20$ to cosmic-variance limit	Intensity and linear polarization across $60 < v < 300$ GHz over entire sky; foreground separation enveloped by SO1	Sampling rate: See Table 3.1. $(3/\text{BeamFWHM}) \times (336'/\text{s})$.	Sampling rate: See Table 3.1. $(3/\text{BeamFWHM}) \times (336'/\text{s})$.	Thermally isolate instrument from solar radiation and from spacecraft bus					
	SO6. Determine if magnetic fields are the dominant cause of low Galactic star-formation efficiency (§ 2.2.3)	Ratio of cloud mass to maximum mass that can be supported by magnetic field ("Mass to flux ratio" μ); ratio of turbulent energy to magnetic energy (Alfvén Mach number \mathcal{M}_A) on scales 0.05–100 pc	The turbulence power spectrum on scales 0.05–100 pc; magnetic field strength (B) as a function of spatial scale and density; hydrogen column density; gas velocity dispersion	Intensity and linear polarization with < 1 pc resolution for thousands of molecular clouds and with < 0.05 pc for the 10 nearest molecular clouds; maps of polarization with $1'$ resolution over the entire sky	Enveloped by SO1–4, except: Angular resolution: $\leq 1.1'$ (at highest frequency)	Angular resolution: $\leq 1.1'$ (at highest frequency)	Sensitivity at 800 GHz: 27.4 kJy/s					
<i>Explore how the Universe evolved (Galactic structure and dynamics)</i>	SO7. Constrain the temperatures and emissivities characterizing the Milky Way's interstellar diffuse dust (§ 2.2.3)	Intrinsic polarization fractions of the components of the diffuse interstellar medium to accuracy better than 3% when averaged over $10'$ pixels	Fractional polarization and intensity as a function of frequency	Intensity and linear polarization maps in 12 frequency bands between 108 and 800 GHz.	Sensitivity at 800 GHz: 27.4 kJy/s	Sensitivity at 800 GHz: 27.4 kJy/s	Sensitivity at 800 GHz: 27.4 kJy/s					

^a The values predicted include delensing and foreground subtraction; see Section 2.2.1.^b Using the PICO τ and BB lensing power spectrum, and BAO from DESI or Euclid. The same strength constraint can be derived independently using clusters detected by PICO, if their redshift becomes available, and using σ_8 from LSST.

2 Science

2.1 Introduction

The Probe of Inflation and Cosmic Origins (PICO) is an imaging polarimeter designed to survey the entire sky at 21 frequencies between 21 and 800 GHz, with a polarization sensitivity that is 57 or 82 times that of the *Planck* mission for the PICO baseline and current best estimate (current best estimate (CBE)) configurations, respectively.

{sec:science}

The mission requirements, which define our baseline design, flow down from a small set of key science objectives listed in Table 2.2. As outlined in this report, this baseline gives rise to a mission that will reach an extraordinarily broad set of science targets, ranging from inflation, to constraints on fundamental particles and fields, to cosmic structure formation and galactic science.

{acro:CBE}

According to inflation, quantum fluctuations in the space-time metric created a background of gravitational waves that imprint a unique signature on the polarization of the CMB. A detection of this inflationary gravity wave (IGW) signal "would be a watershed discovery", a quote from the 2010 decadal panel report [1]. It would be the first observational evidence for quantum gravity, and the signal would also give important clues about the nature of inflation, in particular the energy scale at which it occurred. The strength of the signal is commonly parameterized by r , the tensor-to-scalar ratio. The combination of data from *Planck* and the BICEP/Keck Array give the strongest constraint to date, $r < 0.06$ (95%) [2].

{acro:IGW}

Emission within our own Galaxy is a source of confusion that must be separated with high fidelity before definitive discovery, or stronger upper limits, can be claimed [3]. For the levels of r targeted in the next decade, PICO has both the frequency coverage and sensitivity to measure and separate sources of foreground confusion and is thus poised to detect or place unprecedented constraints on the physics of inflation. Its measurements of the spectral index of primordial fluctuations will give the strongest constraints yet on specific models of inflation.

A few hundred million years after the Big Bang, the neutral hydrogen gas permeating the Universe was reionized by photons emitted by the first luminous sources to have formed. The nature of these sources (e.g., star-forming galaxies or high-redshift quasars) and the exact history of this epoch are key missing links in our understanding of structure formation. Various measurements, including *Planck*'s determination of the optical depth to reionization $\tau = 0.054 \pm 0.007$, have indicated that reionization concluded by $z \approx 6$, but its onset at higher redshift is poorly constrained. PICO will yield a breakthrough in this context via a cosmic-variance-limited¹ measurement of τ , with $\sigma(\tau) = 0.002$, which can only be directly measured in large-scale CMB polarization fluctuations (this is SO5). The only proven method to date for measuring this signal, which requires exquisite control of systematics and foreground contamination, is a space-based platform.

Lensing of the CMB photons by structures as they traverse the Universe provides a projected map of all the matter in the Universe from the epoch of decoupling until today. The non-zero mass of neutrinos affects the clustering of matter and thus can be inferred from maps of the projected matter distribution. The quantity that can specifically be inferred is the sum of the neutrino masses. The current constraint from the combination of *Planck* and large-scale structure data is $\sum m_\nu < 0.12$ eV (95%). This is approaching the minimum summed mass allowed in the inverted neutrino hierarchy of ≈ 0.1 eV and is within a factor of two of the minimal mass allowed in the normal hierarchy of ≈ 0.06 eV. A detection thus appears imminent. However, the precision of determining

¹The cosmic variance limit is the statistical limit arising from observing a single universe.

the neutrino mass scale, using the CMB or *any* other cosmological probe, is limited by knowledge of τ , due to the strong degeneracy between τ and the amplitude of matter fluctuations. PICO’s map of the projected matter, with signal-to-noise ratio (SNR) exceeding 500 – a result of its low noise and high angular resolution – *and* its own cosmic-variance-limited measurement of τ , will give a 4σ detection of $\sum m_\nu$ in the normal hierarchy, rising to 7σ for the inverted hierarchy; see SO3.

{acro:SNR}

The CMB offers a unique window into the thermal history of the Universe, from the time of reheating through today. It is during these eras that the matter and radiation that fill the Universe were produced and evolved to form the structures observed at low redshifts. Measurements of the CMB on small angular scales are sensitive to the many components that make up the Universe including the baryons, cosmic neutrinos, dark matter, and a wide variety of particles motived by extensions of the Standard Model. The Standard Model of particle physics posits three neutrino families, but it also allows for additional light, relativistic particles, if they existed early enough during the evolution of the Universe. We count the total number light particles thermalized in the early Universe using N_{eff} . Light particles thermalized in the early Universe leave a universal contribution to N_{eff} that is sensitive to the freeze-out temperature and the spin of the particle. The current *Planck* measurement of $N_{\text{eff}} = 2.99 \pm 0.17$ (1σ) is sensitive to particles thermalized after the QCD phase transitions. PICO’s measurement with $\sigma(N_{\text{eff}}) = 0.03$ (SO4), enabled by low noise levels, high resolution, and full-sky coverage, will reach back to times when the temperature of the Universe was orders of magnitude hotter than we have probed today, and a period that is still largely unexplored.

These same experimental features are advantageous not only for N_{eff} but for any new physics with signatures on the CMB. Of particular interest is the nature of dark matter and its interactions. PICO will place constraints that are more than one order of magnitude stronger than *Planck* for a dark matter particle of MeV mass range, which can not be probed by direct detection experiments. PICO will thus reveal important clues to the nature of the fundamental physical laws and our cosmic origins.

Secondary anisotropies in the CMB² provide a wealth of information on the growth and evolution of structure in our Universe. CMB lensing, the thermal and kinematic Sunyaev-Zel’dovich (SZ) effects, and extragalactic point sources all contribute significantly to the CMB intensity fluctuations on small angular scales (note that lensing is also present in polarization fluctuations). Immense progress in mapping these sources is enabled by PICO’s depth, broad frequency coverage, and relatively high resolution. The all-sky, projected mass map reconstructed from CMB lensing that PICO will provide can be correlated with tracers of large-scale structure to tomographically probe the growth of structure at unprecedented SNR levels. The thermal SZ effect provides a map of the integrated free-electron pressure along the line of sight, and the peaks in this map trace the locations of all galaxy clusters in the Universe. PICO will find all the massive, virialized, galaxy clusters at any redshift. The epoch of reionization imprints information on the statistical moments of the kinematic SZ signal. The combination of these kSZ statistical moments with the cosmic-variance-limited τ measurement from PICO will provide tight constraints on the global properties of the sources responsible for reionization of the Universe.

{acro:SZ}

Our understanding of magnetic fields is rooted in observations of the very local Universe: the Milky Way and nearby galaxies. Magnetic fields are observed to be a foremost agent of the Milky Way’s ecology. Understanding magnetic fields is crucial for making progress on important issues

²Secondary anisotropies arise from sources other than primordial density and IGW fluctuations

in the astrophysics of galaxies: the dynamics and energetics of the multiphase interstellar medium; the efficiency of star formation; the acceleration and propagation of cosmic rays; and the impact of feedback on galaxy evolution. Through its detailed high-resolution polarization measurements of Galactic dust emission, PICO will produce an unprecedented data set, mapping Galactic magnetic fields and providing answers to these questions (SO6).

Learning about magnetic fields has impact beyond understanding the dynamics and evolution of galaxies. The very origin of magnetic fields in galaxies, and their possible evolution from primordial, early Universe cosmic magnetic fields is a topic of intense debate. PICO is poised to provide definitive answer as to whether early Universe magnetic fields provide the seeds for the magnetic fields observed in most current galaxies.

The magnetized ISM in the solar neighborhood presents a challenge for the investigation of cosmological signals. The signals of interest, such as CMB B-mode polarization, CMB spectral distortions, and 21cm line emission from the cosmic dawn and the reionization epoch, are obscured by Galactic dust and synchrotron emission that can be orders of magnitude brighter. PICO's detailed mapping of these signals will strongly constrain the physical properties of the ISM and thus models of dust grain composition, temperature, and emissivities (SO7).

The PICO deep and high resolution maps will yield a treasure trove of point source that will be mined for years. The mission will provide a full-sky catalog of tens of thousands of extragalactic millimeter and sub-millimeter point sources, which are beacons for active galactic nuclei (in the radio) and dust emission from vigorously star-forming galaxies at $z \sim 2$ and earlier (in the far-IR).

2.2 Science Objectives

2.2.1 Fundamental Physics

Inflation and Gravitational waves

{sec:fundamentals}

Measurements of the CMB together with Einstein's theory of general relativity imply that the observed density perturbations must have been created long before the CMB was released, and rather remarkably even before the Universe became filled with a hot and dense plasma of fundamental particles. Understanding the mechanism generating these perturbations, which evolved to fill the Universe with structures, is one of the most important open questions in cosmology.

PICO's precision measurements of temperature and *E*-mode polarization anisotropy will provide additional detailed information about the statistical properties of the primordial density perturbations generated during this epoch.

The mechanism responsible for the generation of density fluctuations may also produce gravitational waves. PICO will be exquisitely sensitive to the faint imprint that gravitational waves present during recombination leave on the polarization of the CMB. Unlike density perturbations, they not only generate primordial temperature and *E*-mode polarization, but also primordial *B*-mode polarization [4, 5]. Any detection of primordial *B*-mode polarization by PICO would constitute evidence for gravitational waves from the same primordial period that created the density perturbations and open a new window onto this early epoch.

Because the dynamics of gravitational waves is essentially unaffected by the plasma, they would be a pristine relic from the earliest moments of our Universe, and their properties would shed light on the mechanism that created the primordial perturbations.

Inflation, a period of nearly exponential expansion of the early Universe [6–9], is the leading paradigm explaining the origin of the primordial density perturbations [10–14]. It predicts a

nearly scale-invariant spectrum of primordial gravitational waves originating from quantum fluctuations [15]. In this sense, a detection of primordial *B*-modes would be the first observation of a phenomenon associated with quantum gravity [16].

Because the spectrum is scale-invariant, one may hope to detect primordial gravitational waves over a wide range of frequencies including, for example, at LIGO or LISA frequencies. However, as a consequence of the expansion of the Universe, the energy density in the gravitational waves rapidly dilutes with increasing frequency, and observations of the CMB provide the easiest, and for the foreseeable future only way to detect gravitational waves at this scale.

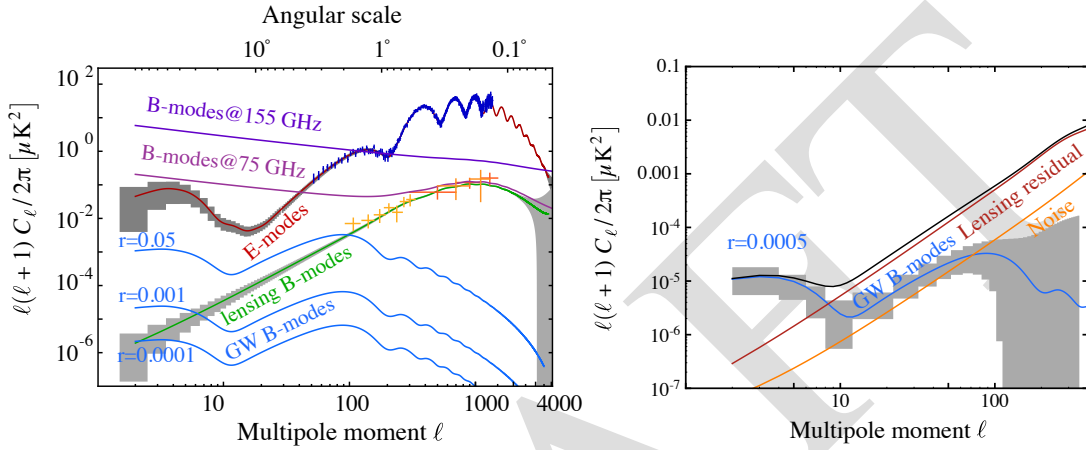


Figure 2.1: *Left panel:* *EE* (red) and lensing *BB* (green) angular power spectra and their measurement uncertainties predicted for PICO (gray), as well as the *BB* power spectrum produced by IGW with different values of r . Also shown are measurements of lensing from current experiments (orange) and *Planck* measurements of the *E* mode (dark blue) [17–21]. The *BB* spectra of Galactic emission on the cleanest 60% of the sky at 75 and 155 GHz (purple) dominate the cosmological signals except at $\ell = 1000$ and over a narrow frequency band. *Right panel:* Predicted uncertainties for a detection of primordial gravitational waves with $r = 0.0005$ for PICO (gray), together with the signal (blue), the instrumental noise (orange), and the lensing residual after internal delensing (red).

{fig:clbb}

The strength of the signal, often quantified by the tensor-to-scalar ratio r , is a direct measure of the expansion rate of the Universe during inflation. Together with the Friedmann equation, this reveals one of the most important characteristics of inflation, its energy scale. PICO’s goal is to detect primordial gravitational waves if inflation occurred at an energy scale of at least 4×10^{15} GeV, or equivalently a tensor-to-scalar ratio of $r = 3 \times 10^{-4}$. A detection would have profound implications for fundamental physics because it would provide evidence for a new energy scale tantalizingly close to the energy scale associated with grand unified theories, and would allow us to probe physics at energies far beyond the reach of terrestrial colliders.

Even in the absence of a detection PICO’s measurements would contain invaluable information about the early Universe. There are only two classes of slow-roll inflation in agreement with current data that naturally explain the observed value of the spectral index of primordial fluctuations n_s . The first class is characterized by potentials of the form $V(\phi) \propto \phi^p$. This class includes many of the simplest models of inflation, some of which have already been strongly disfavored by existing observations (Fig. 2.1, right panel). If the constraints on the spectral index tighten by about a factor two with the central value unchanged, and the upper limits on r improve by an order of magnitude,

this class would be ruled out. Select models in this class are shown as blue lines in Fig. 2.2

The second class is characterized by potentials that approach a constant as a function of field value, either like a power law or exponentially. Two representative examples in this class are shown as the green and gray bands in Fig. 2.2. This class also includes R^2 inflation, which predicts a tensor-to-scalar ratio of $r \sim 0.004$. All models in this class with a characteristic scale in the potential that is larger than the Planck scale predict a tensor-to-scalar ratio of $r \gtrsim 0.001$. Different values of characteristic scales are indicated by the darker lines in Fig. 2.2. Many microphysical models in this class possess a characteristic scale that is super-Planckian, but there are models such as the Goncharov-Linde model with a somewhat smaller characteristic scale that predict a tensor-to-scalar ratio of $r \sim 4 \times 10^{-4}$ [22].

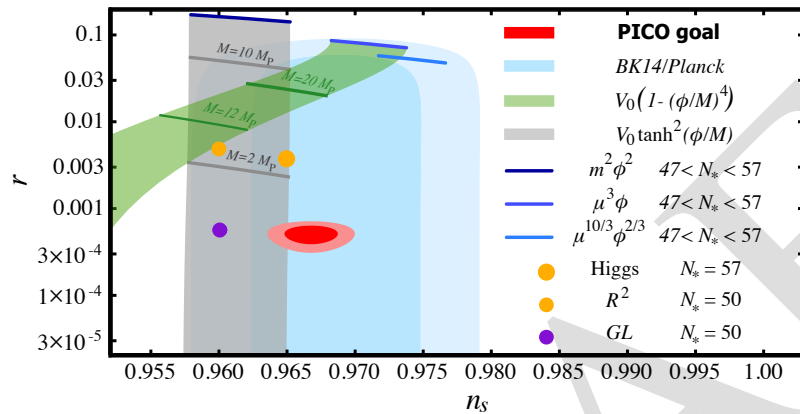


Figure 2.2: Current 1 and 2σ limits on r and n_s (blue) and forecasted constraints for a fiducial model with $r = 0.0005$ for PICO. Also shown are predictions for the selected models of inflation discussed in the text.

{fig:nsr}

In the absence of a detection, PICO will limit the amount of gravitational waves to $r < 10^{-4}$ at 95% CL and will exclude all these models.

Let us now take a closer look at the signal. As shown in Fig. 2.1, it has two contributions, one on degree angular scales or multipoles of $\ell \sim 80$, typically referred to as the recombination peak, and another contribution for multipoles of $\ell \lesssim 10$ from the epoch of reionization.

The contribution from reionization is expected to be brightest relative to the ‘lensing’ B -modes created from E -modes by the deflection of photons by large scale structure on their way to us from the last scattering surface. However, no sub-orbital experiment has yet measured modes at $\ell < 40$. The temporal stability, absence of atmospheric noise, and full-sky coverage offered by a satellite like PICO make it the most suitable instrument to reach these lowest multipoles and detect the reionization ‘bump.’

When the tensor-to-scalar ratio $r \simeq 0.01$, the BB lensing power spectrum and the primordial BB power spectrum are comparable around the recombination peak. For lower levels of r , the lensing B -mode dominates, but the B -mode maps can be ‘delensed’ [23, 24]. The effect of lensing on E and B maps can be determined and undone if these maps are measured with few arcmin resolution and sufficient depth. Forecasts for PICO show that at least 73% of the lensing B -mode power can be removed for the baseline configuration, after accounting for foreground subtraction. 80% will be removed if the foregrounds do not degrade the inherent SNR significantly, rising to 85% for the CBE configuration. Delensing will improve PICO’s determination of r by a factor of five to six. We emphasize that PICO will be relying on its own data to conduct the delensing and foreground cleaning, thus avoiding reduced efficacy arising from the need to cross-calibrate experiments, identify common observing areas on the sky, not having frequency band coverage at

the appropriate resolution to remove foregrounds, or from other systematic uncertainties.

Models of the early Universe differ in their predictions for the scalar spectral index n_s and its scale dependence, often referred to as the running of the spectral index n_{run} . With its high resolution and low noise levels, PICO will improve the constraints on n_s and n_{run} by a factor of about two. In addition, PICO will probe the statistical properties of the primordial fluctuations over a wide range of scales with exquisite precision and improve constraints on departures from Gaussianity by a factor of two to three. By cross-correlating the lensing map with large-scale structure data from LSST it may even be possible to reach a theoretically important threshold (see, e.g. [25] and references therein) and constrain local non-Gaussianity to better than $\sigma(f_{NL}) = 1$. This is discussed in more detail in section 2.2.2.

Fundamental Particles: Light relics, Dark Matter, and Neutrinos

- **Light Relics** In the inflationary paradigm, the Universe was reheated to temperatures of at least 10 MeV and perhaps as high as 10^{12} GeV. At these high temperatures, even very weakly interacting or very massive particles, such as those arising in extensions of the Standard Model of particle physics, can be produced in large abundances [26, 27]. As the Universe expands and cools, the particles fall out of equilibrium, leaving observable signatures in the CMB power spectra. Through these effects the CMB is a sensitive probe of neutrino and of other particles' properties.

One particularly compelling target is the effective number of light relic particle species N_{eff} . The canonical value with three neutrino families is $N_{\text{eff}} = 3.046$. Additional light particles contribute a universal change to N_{eff} that is a function only of the decoupling temperature and the effective degrees of freedom of the particle, g . Furthermore, the range of ΔN_{eff} is quite restricted even for widely varying decoupling temperatures T_F with the range $0.027 g \leq \Delta N_{\text{eff}} \leq 0.07 g$ corresponding to decoupling at higher temperatures during post-inflation reheating ($0.027 g$) to lower temperatures shortly prior to the QCD phase transition ($0.07 g$).

Performance forecasts for N_{eff} are shown in Fig. 2.3. For an experiment like PICO, which has sufficient resolution to reach cosmic-variance-limited measurement of EE up to $\ell = 2300$, the two additional most important parameters for improving constraints are the fraction of sky observed f_{sky} and the noise. Achieving both larger f_{sky} and lower noise are strengths of PICO compared to other platforms. The PICO requirement is to constrain $\Delta N_{\text{eff}} < 0.06$ at 95%. The corresponding improvement in reach in T_F is shown in the right panel of Fig. 2.3. The large improvement over Planck ($\Delta N_{\text{eff}} < 0.28$, 95%) corresponds to a factor of 400 improvement in the limit on the decoupling temperature for any particle with spin.

Many light relics of the early Universe are not stable. They decay, leaving faint evidence of their past existence on other tracers. The relics with sufficiently long lifetime to survive few minutes, past the epoch of light element synthesis, leave a signature on the helium fraction Y_p . If they decay by the time of recombination, their existence through this period is best measured through the ratio of N_{eff} to Y_p . At both CBE and Baseline sensitivity, PICO can simultaneously measure N_{eff} and Y_p with $\sigma(N_{\text{eff}}) = 0.08$ and $\sigma(Y_p) = 0.005$. Alternatively, PICO can measure Y_p at fixed N_{eff} with $\sigma(Y_p) = 0.002$ to independently determine the primordial helium abundance with the same precision as astrophysical measurements. The combination of these measurements is a sensitive test of physics between big bang nucleosynthesis and recombination.

- **Dark Matter** Cosmological measurements have already confirmed the existence of one relic that lies beyond the Standard Model: dark matter. For a conventional WIMP candidate, the CMB places very stringent constraints on its properties through the signature of its annihilation [28–30].

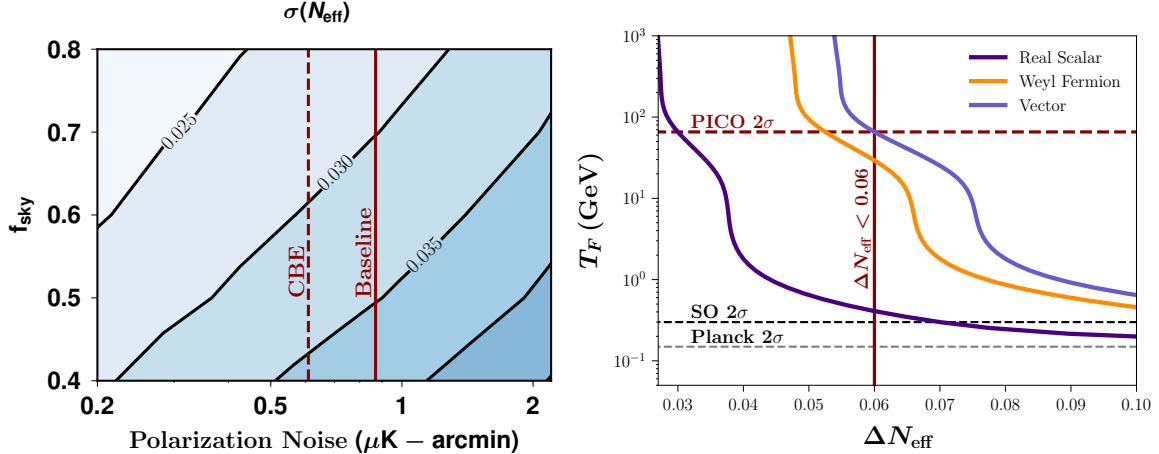


Figure 2.3: *Left:* N_{eff} uncertainty as a function of noise and sky fraction. The resolution assumed is $5'$. Vertical lines denote the expected performance of the baseline mission. *Right:* Reach in the freeze-out temperature for various species, given a measurement of ΔN_{eff} . We see an exclusion of $\Delta N_{\text{eff}} < 0.06$ is a nearly two order of magnitude improvement over Planck and SO. The vertical lines are normalized to the T_f for a single vector particle. | [fig:Neff_future](#)

Most of this information is in the EE power spectrum at $50 < \ell < 300$ and is well-measured by *Planck* and will approach the cosmic variance limit with existing ground based surveys [31, 32]. An entirely complementary way to probe dark matter is to search for evidence of its interactions with other species in cosmological data. Since a lower mass translates to a higher number density of scattering centers, CMB is particularly sensitive to the low-mass regime and is sensitive to large, nuclear-scale cross sections.

Interactions between dark matter and protons in the early Universe creates a drag force between the two cosmological fluids, damping acoustic oscillations and suppressing power in density perturbations on small scales. As a result, the CMB temperature, polarization, and lensing power spectra are suppressed at high multipoles relative to a Universe without such drag forces. This effect has been used to search for evidence of dark matter-proton scattering over a range of masses and couplings, and to provide consistency tests of dark matter in the context of the anomalous 21-cm signal reported by the EDGES collaboration [33–41]

In Fig. 2.4, we present current and projected upper limits on the dark matter-proton interaction cross section as a function of dark matter mass, for a spin-independent velocity-independent scattering (chosen as our fiducial model). Regions above the curves are excluded at the 95% confidence level. We compare current limits obtained from *Planck* (from [36]) with projections for PICO sensitivity. We note that PICO can deliver a substantial improvement over the current limits, across the entire dark matter mass range considered. Most of the constraining power in case of PICO (and ground-based next-generation measurements with similar white-noise levels) comes from the measurement of $C_\ell^{\phi\phi}$.

• **Neutrino Mass** The origin and structure of the neutrino masses is one of the great outstanding questions about the nature of the Standard Model particles. Measurements of neutrinos in the lab have revealed much about the mass differences and mixing angles. Cosmology offers a measurement of the sum of the neutrino masses $\sum m_\nu$ through the gravitational influence of the non-relativistic cosmic neutrinos. The measurement of $N_{\text{eff}} = 2.99 \pm 0.17$ [42] already confirms the existence of these neutrinos at $> 10\sigma$ and their mass implies that they will contribute to the

| [neutrino_fundam](#)

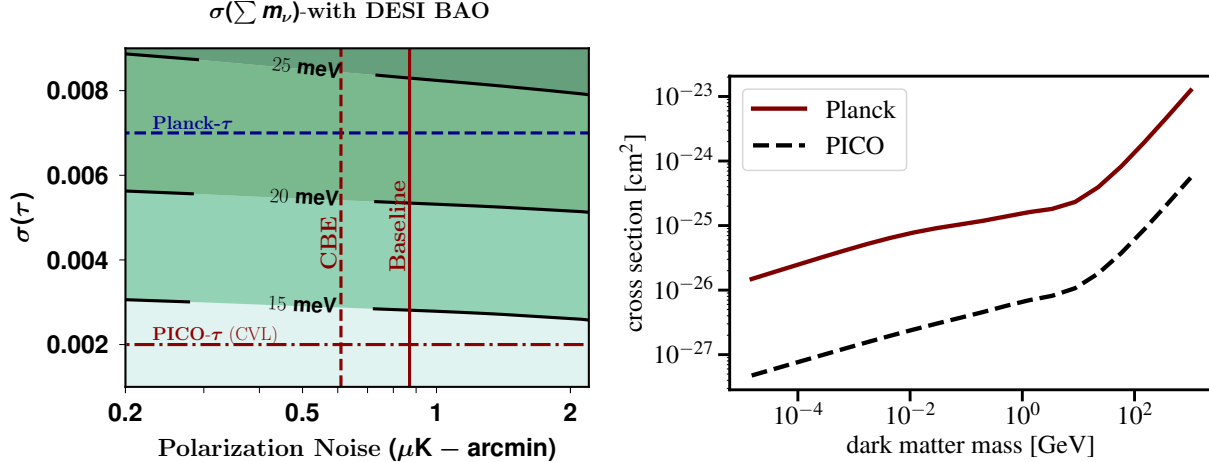


Figure 2.4: *Left:* Forecasts for the sum of neutrino masses uncertainty, including DESI BAO, as a function of noise and the uncertainty in the measurement of τ , for 0.7 sky fraction. The upper blue dashed line is the current *Planck* limit; the lower grey dashed line is the limit from cosmic variance limited measurement of τ . *Right:* Upper limits on DM-proton interaction cross section as a function of DM mass, for a spin-independent velocity-independent scattering. Areas above the curves are excluded at 95% confidence-level. Shown are the current limits from *Planck*([36]) and a forecast for PICO.

{fig:DM_baryons}

matter density at low redshifts. The best current mass constraint arises from a combination of Planck and BOSS barion acoustic oscillations (BAO) giving $\sum m_\nu < 0.12$ eV (95%) [42].

Cosmological measurements are primarily sensitive to the suppression of power on small scales after the neutrinos become non-relativistic, which can be measured via CMB lensing or weak lensing in a galaxy survey. However, these measurements are limited by our knowledge of the amplitude of the primordial fluctuation power spectrum, A_s . In practice, CMB observations most directly constrain $A_s e^{-2\tau}$ and thus do not provide a high precision measurement of either A_s or τ separately.

Although many surveys hope to detect $\sum m_\nu$, any detection of the minimum value expected from particle physics $\sum m_\nu = 58$ meV at more than 2σ will require a better measurement of τ . The best constraints on τ come from E modes with $\ell < 20$ which require measurements over the largest angular scales. To date, the only proven method for such a measurement is from space. The current limit of $\sigma(\tau) = 0.007$ is from *Planck* [43]. Forecasts for a CMB measurement of $\sum m_\nu$ using the lensing B mode [44] are shown in Fig. 2.4. With the current uncertainty in τ one is limited to $\sigma(\sum m_\nu) \gtrsim 25$ meV (after including BAO); no other survey or cosmological probe would improve this constraint. But PICO will reach the cosmic variance limit uncertainty on τ , $\sigma(\tau) \sim 0.002$, and will therefore reach $\sigma(\sum m_\nu) < 15$ meV when combined with measurements of BAO from DESI or Euclid [45]. Robustly detecting neutrino mass at $> 3\sigma$ in any cosmological setting is only possible with an improved measurement of τ like the one achievable with PICO. The measurement would give $\sum m_\nu > 0$ at greater than 4σ or would exclude the inverted hierarchy ($\sum m_\nu > 100$ meV) at 95% confidence, depending on the central value of the measurement. Lab-based measurement could determine the hierarchy before PICO but only cosmology can measure $\sum m_\nu$.

Fundamental Fields: Primordial Magnetic Fields and Cosmic Birefringence

- **Primordial Magnetic Fields** One of the long standing puzzles in astrophysics is the origin of observed 1-10 μG strength galactic magnetic fields [46]. Producing such fields through a dynamo

mechanism requires a primordial seed field [47]. Moreover, μG strength fields have been observed in proto-galaxies that are too young to have gone through the number of revolutions necessary for the dynamo to work. A primordial magnetic field (PMF), present at the time of galaxy formation, could provide the seed or even eliminate the need for the dynamo altogether. Specifically, a ~ 0.1 nG field in the intergalactic plasma would be adiabatically compressed in the collapse to form a $\sim 1 \mu\text{G}$ galactic field [48]. PMFs could have been generated in the aftermath of phase transitions in the early Universe [49], during inflation [50, 51], or at the end of inflation [52]. A detection of PMF with the CMB would be a major discovery as it would establish the field's primordial origin, signal new physics beyond standard models of particle physics and cosmology, and discriminate among different theories of the early Universe [53–55].

The current CMB bounds on PMF strength are $B_{1\text{Mpc}} < 1.2$ nG at 95% CL for the scale-invariant PMF spectrum [56], based on measurements of the TT , TE , EE and BB spectra. The much more accurate measurement of BB by PICO would only marginally improve the PMF bound because CMB spectra scale as $B_{1\text{Mpc}}^4$. However, Faraday rotation provides a signature that scales linearly with the strength of PMF [57]. It converts E modes into B modes, generating mode-coupling EB and TB correlations. So far this signature was out of reach because prior experiments didn't have sufficient sensitivity. Using Faraday rotation, PICO's sensitivity and resolution would allow to probe PMFs as weak as 0.1 nG (1σ), a limit that already includes the effects of imperfect lensing subtraction, Galactic foregrounds [58–60], and other systematic effects. With this limit PICO will conclusively rule out the purely primordial (i.e, no-dynamo driven) origin of the largest galactic magnetic fields.

• **Cosmic Birefringence** The simplest model for late-time acceleration of the Universe is with a slowly-evolving scalar field – the quintessence [61]. Such a field generically couples to electromagnetism through a Chern Simons-like term, and causes linear polarization of photons propagating cosmological distances to rotate. This is known as cosmic birefringence [61]. The birefringence converts primordial E mode into B mode. It thus produces parity-violating TB and EB cross-correlations whose magnitude depends on the statistical properties of the rotation field in the sky [62, 63]. There are no theoretical predictions for the level of birefringence, but if observed, it would be evidence for physics beyond the standard model and a potential probe of dark-energy microphysics [63–65]. Using the sensitivity of only the 155 GHz, PICO will improve current constraints on cosmic birefringence (from POLARBEAR [66]) by a factor of 300. The constraints will be even stronger when including all frequency bands.

2.2.2 Cosmic Structure Formation and Evolution

The Formation of the First Luminous Sources The reionization of the Universe imprints multiple signals in the temperature and polarization of the CMB. In polarization, the most important signal is an enhancement in the EE power spectrum at large angular scales $\ell \lesssim 20$ (Fig. 2.1). This signal gives a direct measurement of the optical depth to the reionization epoch τ , and thus to the mean redshift of reionization z_{re} , with very little degeneracy with other cosmological parameters (Fig. 2.5). The mean redshift of reionization z_{re} (when 50% of the cosmic volume was reionized) depends sensitively on the nature of the ionizing sources. It is currently unknown whether star-forming galaxies or more exotic sources such as supermassive black holes drove the reionization process. What was the mean free path of ionizing photons during this epoch? What was the efficiency with which such photons were produced by ionizing sources? What were the masses and environments of the dark matter halos that hosted the sources? These properties all affect z_{re} . Fur-

{ sec:extragalactics
{ luminoussources }

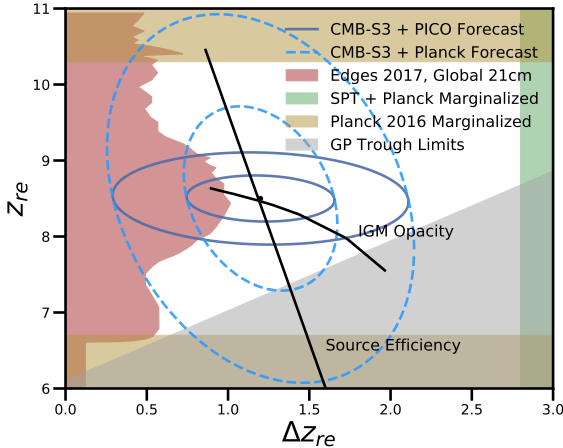


Figure 2.5: [fig:ReionizationPICO](#) Contours of 1 and 2σ constraints on the mean redshift and duration of reionization using PICO and CMB-S3 data (solid dark blue), and comparison with *Planck* and CMB-S3 (dash light blue). Source Efficiency and IGM Opacity (dark lines) are two physical parameters controlling the reionization process in current models. The PICO measurements together with higher resolution data of the kSZ effect will significantly the range of models allowed. We also include other constraints from *Planck*, EDGES, the Gunn-Peterson (GP) trough , and *Planck*+ the South Pole Telescope (SPT) [42, 69–71].

thermore, the detailed shape of the low- ℓ E -mode power spectrum is sensitive to the reionization history itself (i.e., $d\tau/dz$), and will provide information beyond that captured in τ alone. For example, it has been argued that *Planck* data show evidence for an extended tail of reionization out to $z \approx 15$ -20 [67]. A cosmic-variance-limited measurement of the large-scale E modes, as obtained by PICO, will settle this question.

Large-scale EE power spectrum measurements are a unique and crucial observable for many aspects of cosmology, particularly the growth of structure. If measurements of τ are not improved beyond the current uncertainties from *Planck*, inference of several new signals of cosmological physics will be severely hindered. A canonical example is the inference of the sum of the neutrino mass (Page 10), but any cosmological inference related to the growth of structure will be affected to some extent, including constraints on dark energy and modified gravity from weak lensing, cluster counts, and similar structure probes. PICO is the ideal experiment to resolve this issue. Its noise level and frequency coverage permit a cosmic-variance-limited constraint on τ , i.e., $\sigma(\tau) \approx 0.002$, which we have verified with explicit forecasts including separation of foregrounds.

In temperature, an important imprint of reionization is that sourced at small angular scales by the “patchy” kinematic Sunyaev-Zel’dovich (kSZ) effect, due to the peculiar velocities of free electron bubbles around ionizing sources. Measurements of the small- scale kSZ power spectrum, with instruments that have higher resolution than PICO, can give constraints on the duration of reionization Δz_{re} [68]. Fig. 2.5 presents forecasts for reionization constraints in the $z_{re} - \Delta z_{re}$ parameter space obtained from PICO’s measurement of τ in combination with ground-based Stage-III CMB experiments measurements of the kSZ power spectrum. The PICO measurement of τ is essential for breaking degeneracies and allowing simultaneous, precise constraints to be placed on both the mean redshift and duration of reionization. The figure also shows curves of constant efficiency of production of ionizing photons in the sources, and of intergalactic medium opacity. These are two parameters that quantify models of reionization. The curves shown are illustrative; families of models, that would be represented by parallel ‘source efficiency’ and ‘IGM Opacity’ lines, are allowed by current data. PICO’s data will give simultaneous constraints on these physical parameters, yielding important information on the nature of the first luminous sources. For example, galaxies or quasars predict significantly different values for these parameters.

In addition to these signals, reionization also leaves specific non-Gaussian signatures in the CMB. In particular, patchy reionization induces non-trivial 4-point functions in both temperature [72] and polarization [73]. The temperature 4-point function can be used to separate reion-

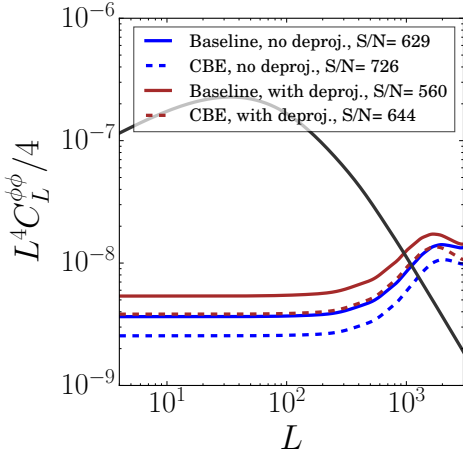


Figure 2.6: The theoretically predicted lensing power spectrum $C_L^{\phi\phi}$ (black) and forecasted PICO noise levels, with (red), and without (blue) deprojection, that is removal, of foregrounds. PICO will make a map of ϕ at angular scales where the noise is below the signal.

ization and late-time kSZ contributions. Combinations of temperature and polarization data can be used to build quadratic estimators for reconstruction of the patchy τ field, analogous to CMB lensing reconstruction. These estimators generally require high angular resolution, but also rely on foreground-cleaned CMB maps. Thus, while PICO alone may not enable high SNR reconstructions, its high-frequency bands — which have better than 2 arcmin resolution and cover frequencies that are not suitable for observations from the ground — will enable these estimators to be robustly applied to ground-based CMB data sets, a strong example of ground-space complementarity.

Probing Structure Formation via Gravitational Lensing Matter between us and the last-scattering surface deflects the path of photons through gravitational lensing, imprinting the 3-dimensional matter distribution across the volume of the Universe onto the CMB maps. The specific quantity being mapped by the data is the projected gravitational potential ϕ that is lensing the photons. From the lensing map, which receives contributions from all redshifts between us and the CMB with the peak of the distribution at $z \simeq 2$, we infer the angular power spectrum $C_L^{\phi\phi}$. Both the temperature and polarization maps of the CMB, and by extension the angular power spectra, are affected by lensing.

Planck's ϕ map had SNR of ~ 1 per L mode over a narrow range of scales, $30 < L < 50$. PICO's map would represent true mapping, with $\text{SNR} \gg 1$ per each mode down to scales of approximately ten arcminutes ($L \sim 1000$, Fig. 2.6)³. On smaller scales, the map will still contain statistical information. While *Planck* had an SNR of 40 integrated across the $C_L^{\phi\phi}$ power spectrum [74], the PICO combination of resolution, sensitivity, and sky coverage enables a measurement with SNR of 638 and 737 for the baseline and CBE configurations, respectively. When accounting for possible foreground contamination, its broad frequency coverage leads to a reduction of SNR of less than 20% (Fig. 2.6).

The value of the reconstructed lensing map is immense, as has already been demonstrated with the much lower SNR map from *Planck*. The unprecedented constraints on neutrino mass, discussed in page 10, are a direct result of this deep map. Tomographic cross-correlations of the lensing map with samples of galaxies and quasars will yield constraints on structure formation. The measurements will constrain the properties of quasars and other high-redshift astrophysics, e.g., a precise determination of the quasar bias (and hence host halo mass) as a function of their

³We use L to refer to multipoles in the CMB lensing and galaxy clustering fields, in contrast to the use of ℓ for the CMB itself.

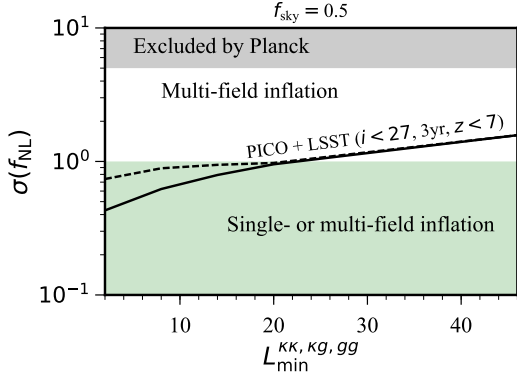


[fig:fnlconstraint](#)

Figure 2.7: [Forecasted sensitivity to the parameter describing primordial non-Gaussianity of the local type for the PICO CMB lensing map together with three years of the LSST survey, as a function of the minimal multipole used in the analysis. A value of $\sigma(f_{\text{NL}}) \simeq 1$ is a well-motivated theoretical target.

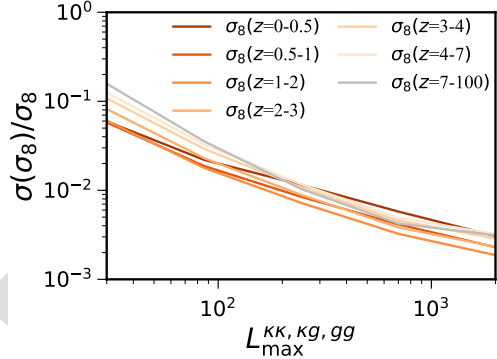


[fig:sigma8constraint](#)

Figure 2.8: [Forecasted sensitivity to the parameter describing the amplitude of structure in various redshift bins, as a function of the maximal multipole used in the analysis. Percent-level constraints on these parameters allow for stringent tests of physics beyond Λ CDM that modify the rate of growth of structure.

properties, such as (non-)obscuration. The map will be cross-correlated with other large scale tracers to probe fundamental physics. For instance, one can use correlations between large scale structure tracers with different clustering bias factors to effectively cancel cosmic variance [75, 76] and constrain physics that affects the biasing of objects on large scales, such as primordial local non-Gaussianity [77]. In Fig. 2.7 we show the expected constraints for the CMB lensing field as reconstructed with PICO, in cross correlation with three years of the LSST survey. It can be seen that depending on the minimal multipole that can be used in the cross correlation, which is uncertain in both LSST and the PICO lensing map, the well-motivated theory target of $\sigma(f_{\text{NL}}) \simeq 1$ [25] can be within reach. Values of f_{NL} at or above this level are a generic prediction of multi-field inflationary models.

Using the same cross-correlation techniques, it is also possible to constrain the evolution of the amplitude of structure as a function of redshift. Fig. 2.8 shows constraints on the amplitude of linear structure in several redshift bins. This is a model-independent representation of the structure growth constraints; these measurements will yield constraints on dark energy or modified gravity, in the context of specific models. The measurements can also be used for a neutrino mass constraint that is complementary to and competitive with that inferred from the CMB lensing auto-power spectrum described earlier.

Lensing will also be used to weigh dark matter halos hosting galaxies, groups, and clusters of galaxies. Calibrating the masses of galaxy clusters is the most uncertain and crucial step in the cluster cosmology program, in which CMB lensing has already begun to play an important role. In this approach, known as CMB halo lensing, we focus on the small-scale effects of gravitational lensing around these objects [78–80]. The technique holds great potential for measuring halo masses out to high redshifts where gravitational lensing of galaxies (i.e., gravitational shear) no longer works because of the lack of background sources.

This is illustrated in Fig. 2.9, which shows the mass sensitivity of PICO using a spatial filter optimized for extracting the mass of halos [81]. The curves give the one-sigma noise in a mass measurement through the filter as a function of redshift. Their flattening at high redshift reflects

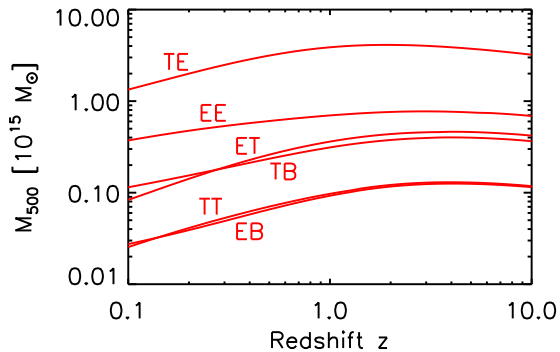


[fig:Halolensing](#)
Figure 2.9: PICO sensitivity for CMB halo lensing. Curves for different CMB signal correlations give the one-sigma sensitivity of an optimal mass filter [81]. The curves are flat at high redshift, demonstrating the essential property that CMB halo lensing can be applied over a very wide redshift range, and well beyond the $z = 2$ limit of the figure. For PICO, the EE and TT estimators are roughly equivalent, offering important cross-validation of measurements because the systematics are very different for temperature and polarization.

the fact that CMB lensing is sensitive over a broad range of redshifts, extending well beyond the limit of $z = 2$ of the figure. We see that PICO can measure the mass of individual low-mass clusters ($\sim 10^{14} M_\odot$) over a wide redshift range, and by stacking we can determine the mean mass of much smaller halos, including those hosting individual galaxies.

Halo lensing will enable calibration of the galaxy cluster mass scale, which is critical for our cosmological analysis of PICO cluster counts, as mentioned above. It also gives a unique tool for measuring the relation between galaxies and their dark matter halos during the key epochs of cosmic star formation at $z \geq 2$, not reachable by other means. This will provide valuable insight into the role of environment on galaxy formation during the rise to and fall from the peak of cosmic star formation at $z \sim 2$. From a complementarity perspective, the high-resolution, high-frequency PICO channels will play an essential role in cleaning foregrounds for high-resolution ground-based halo lensing measurements at lower frequencies, particularly those derived from the temperature-based estimator, which is most contaminated by foregrounds.

Constraining Galaxy Formation via the Sunyaev-Zel'dovich (SZ) Effects Not all CMB photons propagate through the Universe freely; about 6% are Thomson-scattered by free electrons in the intergalactic medium (IGM) and intracluster medium (ICM). These scattering events leave a measurable imprint on CMB temperature fluctuations, which thereby contain a wealth of information about the growth of structures and the thermodynamic history of baryons. A fraction of these photons are responsible for the thermal and kinetic Sunyaev–Zel'dovich effects (tSZ and kSZ) [82, 83]. The amplitudes of the tSZ and kSZ signals are proportional to the integrated electron pressure and momentum along the line of sight, respectively. They thus contain information about the thermodynamic properties of the IGM and ICM, which are highly sensitive to astrophysical ‘feedback’. Feedback is the process of energy injection into the IGM and ICM from accreting supermassive black holes, supernovae, stellar winds, and other sources. The tSZ effect will be used to measure ensemble statistics of galaxy clusters, which contain cosmological information, as well as to provide uniform cluster samples for galaxy formation studies in dense environments.

• **Galaxy Clusters** Galaxy clusters found via the tSZ effect provide a well-defined sample with a simple-to-model selection function. Sample of clusters such as these are straightforward to use for cosmological inference and studies of galaxy evolution in dense environments. The tSZ-selected sample from PICO will provide all clusters with masses above $\sim 3 \times 10^{14} M_\odot$ (defined with respect to the radius within which the average density reaches 200 times the critical) out to high redshifts, as long as the clusters have started to virialize. We forecast that PICO will find $\sim 150,000$ galaxy clusters, assuming the cosmological parameters from *Planck* and applying a galaxy mask, using

{sz}

{clusters}

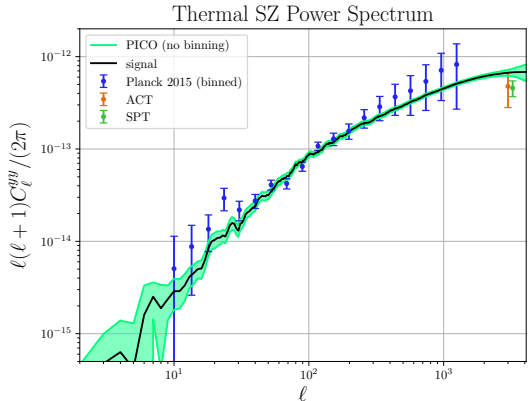


Figure 2.10: Constraints on the tSZ power spectrum from PICO and current data. A simulated tSZ power spectrum (black) is constrained at each multipole by PICO’s data (1σ , green). Binning in ℓ , would increase the SNR beyond the calculated value of 1270, which is already nearly 100 times larger than *Planck* (blue). We include current measurements by SPT and ACT, two ground-based programs [85, 86]

only 70% of the sky. With redshifts provided by optical surveys and infrared follow-up observations, the PICO tSZ-selected cluster sample will be an excellent cosmological probe, with mass calibration provided by CMB halo lensing described above and optical weak lensing for clusters with $z < 1.5$.

• **Compton-y map and tSZ auto-power spectrum** In addition to finding individual clusters, multifrequency CMB data also allow the reconstruction of full-sky maps of the tSZ signal. These are called ‘Compton-y maps’. With its extremely low noise and broad frequency coverage, which is essential for separating out other signals, PICO will yield a definitive Compton-y map over the full sky, with high SNR down to angular scales of a few arcminutes. We quantify this expectation by reconstructing the Compton-y field using the needlet internal linear combination (NILC) algorithm [84] applied to sky simulations generated with the *Planck* sky model, with maps at all PICO frequencies (with appropriate noise added). The error bars on the reconstructed tSZ power spectrum are shown in Fig. 2.10, in comparison to current measurements. The total SNR is 1270 for the PICO CBE configuration, with the PICO baseline configuration only $\approx 10\%$ lower. This is nearly two orders of magnitude higher SNR compared to *Planck*, which has already provided data with much higher SNR compared to ground-based experiments.

Extremely strong constraints on models of astrophysical feedback will be obtained from the analysis of the PICO y-map, both from its auto-power spectrum and from cross-correlations with galaxy, group, cluster, and quasar samples. Like the CMB lensing map described above, the legacy value of the PICO y-map will be immense. As an example, we forecast the detection of cross-correlations between the PICO y-map and galaxy weak lensing maps constructed from LSST and WFIRST data. Considering the LSST “gold” sample with a source density of 26 galaxies/arcmin² covering 40% of the sky, we forecast a detection of the tSZ – weak lensing cross-correlation with S/N = 3000. Cross-correlations with the galaxies themselves will be measured at even higher S/N. At this immense significance, the signal can be broken down into dozens of tomographic redshift bins, yielding a precise breakdown of the evolution of thermal pressure over cosmic time. For PICO and WFIRST (assuming 45 galaxies/arcmin² covering 5.3% of the sky), we forecast S/N = 1100 for the tSZ – weak lensing cross-correlation. The WFIRST galaxy sample extends to higher redshift, and thus this high-S/N measurement will allow the evolution of the thermal gas pressure to be probed to $z \approx 2$ and beyond, the peak of the cosmic star formation history. These transformative measurements will revolutionize our understanding of galaxy formation and evolution by distinguishing between models of feedback energy injection at high significance. Additional cross-correlations of the PICO y-map with quasar samples, filament catalogs, and other large-scale

{ymp}

structure tracers will further demonstrate its immense legacy value, providing valuable information on baryonic physics that is complementary to inferences from the lensing cross-correlations described earlier.

2.2.3 Galactic Structure and Star Formation

Observations of Galactic polarization are a highlight and a lasting legacy of the *Planck* space mission. Spectacular images combining the intensity of dust with the texture derived from polarization data have received world-wide attention and have become part of the general scientific culture [87]. Beyond their popular impact, the *Planck* polarization maps represented an immense step forward for Galactic astrophysics [88]. We expect an even greater leap forward from PICO based on the higher angular resolution dust polarization images obtained with the balloon experiment BLAST-Pol. PICO will provide all-sky maps of dust polarization at higher resolution than BLASTPol and with significantly higher sensitivity than *Planck* (Fig. 2.11.) Such a data set can only be obtained from a space mission. The data will complement a rich array of polarization observations including stellar polarization surveys to be combined with Gaia astrometry and synchrotron observations measuring Faraday rotation at radio wavelengths with the Square Kilometer Array and its precursors. Here, we focus on two key crucial Galactic science measurements that require PICO.

(1) *Testing Composition Models of Interstellar Dust:* PICO will enable spectral characterization of Galactic polarization. This in turn enables us to refine and test models of dust composition and grain alignment, which are of interest for the interpretation of dust polarization data at large.

(2) *Determining how magnetic fields affect the processes of molecular cloud and star formation:* By virtue of the strong dynamical coupling of dust and gas and the systematic alignment of dust grains with magnetic fields, dust polarization probes magnetic fields in the cold and warm neutral phases of the diffuse ISM (which contains the bulk of the ISM gas mass and turbulent energy) down to the scale of molecular clouds (which are where stars form). PICO will measure polarization across this broad range of scales to trace the role of magnetic fields through the entirety of the star formation process.

Dust Physics

Strong extinction features at 9.7 and 18 μm indicate much interstellar dust is in the form of amorphous silicates while features at 2175 Å, 3.3 μm , and 3.4 μm attest to abundant hydrocarbons. It is unknown, however, whether the silicate and carbonaceous materials coexist on the same grains or whether they are segregated into distinct grain populations. If there are indeed multiple grain species, this will induce additional challenges for modeling the emission from interstellar dust in both total intensity and polarization at levels relevant for B-mode science [90].

Spectropolarimetry of dust extinction features reveals robust polarization in the 9.7 μm silicate feature [e.g., 91], indicating that the silicate grains are aligned with the interstellar magnetic field. In contrast, searches for polarization in the 3.4 μm carbonaceous feature have yielded only upper limits, even along sightlines where silicate polarization is observed [92, 93]. These data are consistent with silicate and carbonaceous materials existing on separate grains with different alignment properties. However, the 3.4um feature arises only from aliphatic (chain-like) carbonaceous material, which may not trace all carbon-bearing grains. Additionally, the data are restricted to only a few highly-extincted sightlines that may not typify the diffuse ISM.

At odds with the spectropolarimetric evidence from dust extinction, current measurements of the polarization fraction of the far-infrared dust emission with *Planck* [94] and BLASTPol [95]

{sec:galacticsci}

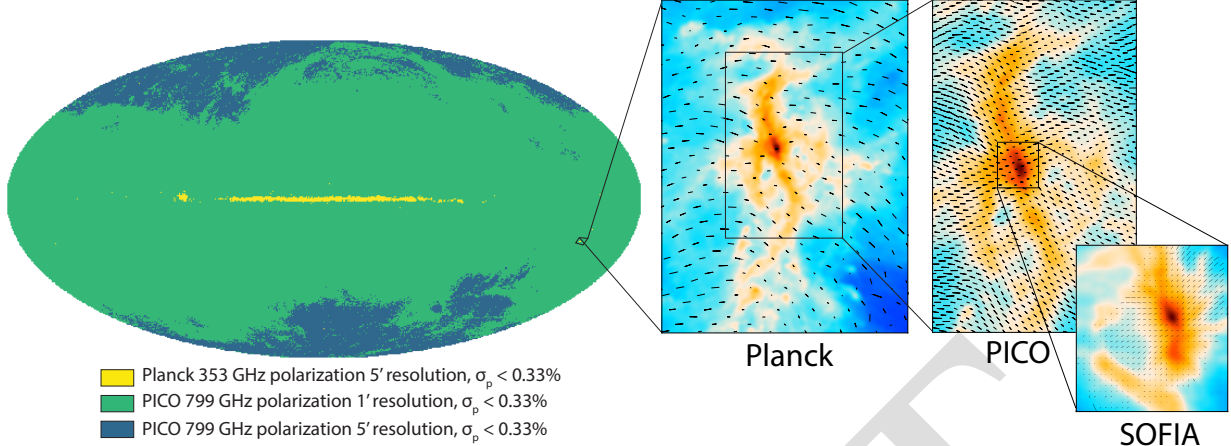


Figure 2.11: At 799 GHz, the PICO Baseline mission will map nearly the entire sky at $1'$ resolution with a sensitivity of 0.33% (The CBE will improve this to the entire sky at $1'$, $\sigma_p < 0.33\%$). PICO will significantly improve over Planck’s coverage and resolution, and thus PICO will be capable of characterizing magnetized turbulence from the diffuse ISM down to dense star forming cores, complementing high-resolution polarimetry from instruments such as HAWC+/SOFIA [89]

{fig:allsky}

betray little to no frequency dependence, as would be expected if two components with distinct polarization properties were contributing to the total emission. However, current uncertainties are relatively large and the data with $v > 353$ GHz are from high density sightlines that may not be representative of the diffuse ISM. With great polarization sensitivity even in diffuse regions, PICO will provide a definitive test of the two component paradigm.

To assess PICO’s ability to discriminate quantitatively, we employ the analytic two component dust mode of [96] which provided a better fit to IRAS and *Planck* data than one component models.

Applying the noise estimates from PICO, 1000 simulations were run for different combinations of polarization fractions of the two components in this model. Only frequency channels 107 GHz and above were used, and the simulated data were binned to the $7.9'$ beam of the PICO 107 GHz channel. Based on the variance of the simulation results, PICO can determine the intrinsic polarization fractions of the two components to a precision of 1-2%. PICO will therefore be able to validate or reject state-of-the-art dust models [e.g. 97, Hensley & Draine, in prep] and test for the presence of additional grain species with distinct polarization signatures, such as magnetic nanoparticles [98].

Are Magnetic Fields Responsible For Low Star Formation Efficiency?

Stars form out of dense, gravitationally unstable regions within molecular gas clouds. The efficiency of this conversion from molecular gas to stars is very low, due to regulation from supersonic turbulent gas motions, magnetic fields, and feedback from young stars [99]. Magnetic fields may play an important role in slowing the process of star formation by inhibiting movement of gas in the direction perpendicular to the field lines. Observations to date suggest that the outer envelopes of clouds can be supported against gravity by magnetic fields, but in dense cores gravity tends to dominate, and so these dense structures can collapse to form stars [100].

On larger scales, the formation of gravitationally unstable clouds is regulated by the flow of diffuse material into the molecular phase, a process that is mediated by magnetized turbulence in the low-density ISM. Structure formation in the diffuse ISM is poorly understood, but as a pre-

cursor to star formation it is crucial to understand what drives molecular cloud formation. Recent observations suggest that the structure of the diffuse medium is highly anisotropic, and strongly coupled to the local magnetic field [101–104].

However, the degree to which magnetic fields affect the formation of molecular clouds as well as stars within these clouds is poorly constrained, in large part due to the difficulty of making detailed maps of magnetic fields in the interstellar medium.

• **Formation of Stars within Magnetized Molecular Clouds** With full-sky coverage and a best resolution of $1.1'$, PICO will be able to map all molecular clouds with better than 1 pc resolution, out to a distance of 3.4 kpc. Extrapolating from the Bolocam Galactic Plane Survey [BGPS, 105], PICO is expected to make highly detailed magnetic field maps of over 2,000 molecular clouds with thousands to hundreds of thousands of independent measurements per cloud.

Our goal is to constrain both the strength of the magnetic field, B , within these clouds, as well as the energetic importance of the field compared to self-gravity (parameterized by the mass-to-flux ratio μ) and turbulence (parameterized by the Alfvén Mach number M_A) as a function of density. To measure these quantities we will apply a series of established polarization analysis techniques: (1) characterizing the relative orientation of cloud structures and the magnetic field [106–109]; (2) making probability distributions functions of polarization measurables [110, 111]; (3) comparing between the magnetic field and velocity gradient directions [112–114]; and (4) measuring the angular dispersion of the magnetic field [115–118]. By applying all four techniques to both PICO observations and synthetic polarization maps made from “observing” numerical simulations of star formation, we will quantitatively compare theory and observations. PICO’s large number of frequency bands will be used to better model the temperature and polarization efficiency of the cloud dust [119], which can then be used to generate more realistic generation of synthetic observations from simulations for comparison with PICO observations [120]. We can then compare the observed magnetization levels derived from the PICO observations to the levels of turbulence derived from molecular gas surveys (e.g.: (author?) 105, 121), and the efficiency of star formation, measured from near and far-IR observations of dense cores and protostars with *Herschel*, *Spitzer*, and *WISE*.

PICO’s ability to map thousands of clouds is not possible with any other current or proposed polarimeter. Planck, for example, was only able to map 10 nearby clouds to a similar level of detail [109]. This large sample of clouds is crucial because dust polarization observations are sensitive to only the magnetic field projected on the plane of the sky, and therefore polarization maps will look very different for molecular clouds observed at different viewing angles. By observing thousands of molecular clouds PICO will determine the role of magnetic fields in star formation as a function of cloud age and mass.

• **Formation of Magnetized Molecular Clouds from The Diffuse Interstellar Medium** Structure formation in the diffuse ISM is a key area of study motivating observations across the electromagnetic spectrum. PICO’s observations will complement recently completed high dynamic range neutral hydrogen (HI) surveys, such as HI4PI [122] and GALFA-HI [123], as well as planned surveys of interstellar gas, most prominently with the Square Kilometer Array (SKA) and its pathfinders. One of the open questions in diffuse structure formation is how gas flows within and between phases of the ISM. A planned all-sky absorption line survey with SKA-1 will increase the number of measurements of the ISM gas temperature by several orders of magnitude [124]. Quantitative comparisons of the ISM temperature distribution from SKA-1 and estimates of the magnetic field strength and coherence length scale from PICO will elucidate the role of the magnetic field in ISM

phase transitions.

A comprehensive understanding of the magnetized diffuse ISM is challenging because of its diverse composition, its sheer expanse, and the multi-scale nature of the physics that shapes it. To understand how matter and energy are exchanged between the diffuse and dense media, it is essential to measure the properties of the magnetic field over many orders of magnitude in column density. PICO is unique in its ability to do this in the diffuse ISM. *Planck* achieved measurements of the diffuse sky at $60'$ resolution, resulting in $\sim 30,000$ independent measurements of the magnetic field direction in the diffuse ISM. With $1.1'$ resolution PICO will expand the number of independent polarization measurements in the diffuse ISM to $\sim 86,000,000$. This will allow us to robustly characterize turbulent properties like M_A across a previously unexplored regime of parameter space.

Galactic Legacy Science

PICO will also produce legacy datasets that will revolutionize our understanding of how magnetic fields influence physical processes ranging from planet formation to galaxy evolution. For 10 nearby clouds ($d < 500$ pc) PICO will resolve magnetic fields on the crucial 0.1 pc size scale associated with dense cores and filaments, and observe how the magnetic fields on these scales directly influence the formation structure of cores. By comparing the orientation of the core-scale magnetic field with respect to the orientation and sizes of protoplanetary disks, PICO will directly test whether there is evidence that magnetic breaking inhibits the growth of protoplanetary disks [125, 126].

On larger scales, PICO's tens of millions of independent measurements of magnetic field orientation will allow us to directly probe magnetized turbulence and study how magnetic fields are generated through a combination of turbulence and large scale gas motions [127]. Key processes in the diffuse ISM, including heat transport [128], streaming of cosmic rays [129], and magnetic reconnection [130] are dramatically dependent on the level of magnetization.

Finally, PICO observations will create detailed magnetic field maps of approximately 70 nearby galaxies, with more than 100 measurements of magnetic field direction per galaxy. These observations will be used to study the turbulence on galactic scales, determine whether the magnetic fields of the Milky Way in the diffuse ISM are consistent with other galaxies, and directly study how interaction between large scale magnetic fields, turbulence, and feedback from previous generations of star formation affect galaxy evolution and star formation efficiency.

2.3 Cosmological Legacy Surveys

2.3.1 Early phases of galaxy evolution

PICO will have a crucial role in providing answers to major, still open issues on galaxy formation and evolution. Which are the main physical mechanisms shaping the galaxy properties [136, 137]: in situ processes, interactions, mergers, or cold flows from the intergalactic medium? How do feedback processes work? To settle these issues we need direct information on the structure and the dynamics of high- z galaxies. But these are compact, with typical sizes of 1–2 kpc [138]), corresponding to angular sizes of 0.1–0.2 arcsec at $z \simeq 2$ –3. Thus they are hardly resolved even by ALMA and by HST. If they are resolved, high enough SNR per resolution element are achieved only for the brightest galaxies, which are probably not representative of the general population.

Strong gravitational lensing provides a solution to these problems. PICO will detect galaxies whose flux densities are boosted by large factors (Fig. 2.12, right panel). Since lensing conserves

Table 2.3: Cosmological Legacy Science

{tab:STM2}

Catalog	Impact	Science
1. Proto-Clusters	Discover $\sim 50,000^a$ mm/sub-mm protoclusters distributed over the sky and back to $z \sim 4.5$. Current knowledge: <i>Planck</i> data expected to yield a few tens.	Probe the earliest phases of cluster evolution, well beyond the reach of other instruments; test the formation history of the most massive virialized halos; investigate galaxy evolution in dense environments.
2. Strongly Lensed Galaxies	Discover 4500^a highly magnified dusty galaxies across redshift. Current knowledge: 13 sources confirmed in <i>Planck</i> data; few hundred candidates in <i>Herschel</i> , SPT and ACT data.	Gain unique information about the physics governing early, $z \simeq 5$, galaxy evolution, taking advantage of magnification and extra resolution enabled by gravitational lensing; learn about dark matter sub-structure in the lensing galaxies.
4. Polarized Point Sources	Detect 2000^b radio and several thousand dusty galaxies in polarization. Current knowledge: ~ 200 up to 100 GHz; 1 polarization measurement of a dusty galaxy.	Give information on the jets of extragalactic sources, close to their active nuclei. Determine the large-scale structure of magnetic fields in dusty galaxies. Determine the importance of polarized sources as a foreground for CMB polarization science.

^a Confusion (not noise) limited

^b Noise and confusion limited

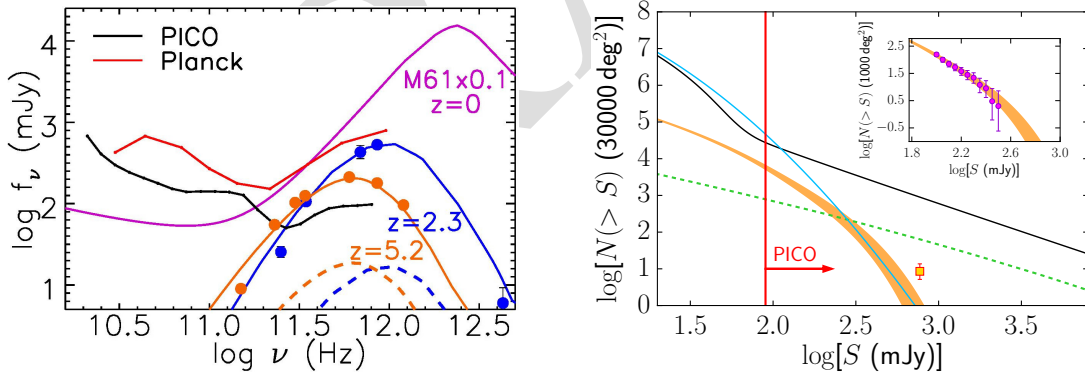


Figure 2.12: **Left panel.** Example spectral energy distributions (SEDs) of dusty star-forming galaxies detectable by PICO, compared with its point source detection limits (black line) and with the *Planck* 90% completeness limits (red line [131]). PICO will detect nearby galaxies, like M61 (magenta), whose SED was scaled down by a factor of ten, and high- z strongly lensed galaxies, like SMM J2133-0102 (blue) at $z = 2.3$ [132] and HLSJ091828.6+514223 (orange) at $z = 5.2$ [133]. The dashed lines are corrected for lensing magnification. **Right panel.** Integral counts at $500\mu\text{m}$ (600 GHz) of unlensed, low- z (black) and strongly lensed, high- z (orange) star-forming galaxies based on fits of *Herschel* counts (inset [134]), also shown are predicted radio source counts (green). The PICO detection region (right of vertical red line) will yield a factor of 1000 increase in strongly lensed galaxies relative to *Planck* (yellow square), and $\sim 50,000$ proto-clusters (blue) [135].

{fig:SED3}

the surface brightness, the effective angular size is stretched on average by a factor $\mu^{1/2}$, where μ is the gravitational magnification, thus substantially increasing the resolving power. A spectacular example are ALMA observations of the strongly lensed galaxy PLCK_G244.8+54.9 at $z \simeq 3.0$ with $\mu \simeq 30$ [139]. ALMA observation with a $0.1''$ resolution reached the astounding spatial resolution of $\simeq 60\text{pc}$, substantially smaller than the size of Galactic giant molecular clouds. Other high- z galaxies spatially resolved thanks to gravitational lensing, with less extreme magnifications, are reported by (author?) [140], and others [141, 142].

Cañameras et al. [139] have also obtained CO spectroscopy, measuring the kinematics of the molecular gas with an uncertainty of 40–50 km/s. This spectral resolution makes possible a direct investigation of massive outflows driven by AGN feedback at high z . In this way (author?) [143] were able to detect a fast (800 km/s) molecular outflow due to feedback in a strongly lensed galaxy at $z = 5.3$. The outflow carries mass at a rate close to the SFR and can thus remove a large fraction of the gas available for star-formation.

Herschel surveys have demonstrated that, at the PICO detection limit at $\simeq 500\,\mu\text{m}$ (600 GHz), about 25% of all detected extragalactic sources are strongly lensed; for comparison, at optical/near-IR and radio wavelengths, were intensive searches have been carried out for many years, the yield is of only 0.1%, i.e. more than two orders of magnitude lower [144]. To add to the extraordinary sub-mm bonanza, the selection of strongly lensed galaxies detected by sub-mm surveys is extremely easy because of their peculiar sub-mm colors (Fig. 2.12, left panel), resulting in a selection efficiency close to 100% [145].

A straightforward extrapolation of the *Herschel* counts to the much larger area covered by PICO shows that its surveys will yield $\sim 4,500$ strongly lensed galaxies with a redshift distribution peaking at $2 \lesssim z \lesssim 3$ [134] but extending up to $z > 5$ (Fig. 2.12, left panel). If objects like the $z = 5.2$ strongly lensed galaxy HLSJ091828.6 + 514223 exist at higher redshifts, they will be detectable by PICO up to $z > 10$.

An intensive high spectral and spatial resolution follow up campaign of such a large sample will be challenging but also extremely rewarding since it will allow a giant leap forward towards the understanding of the processes driving early galaxy evolution, in addition to opening many other exciting prospects both on the astrophysical and on the cosmological side (cf., e.g., ref. [144]). The PICO all-sky surveys will select the brightest objects in the sky, maximizing the efficiency of the effort.

2.3.2 Early phases of cluster evolution

PICO will open a new window for the investigation of early phases of cluster evolution, when their member galaxies were actively star forming but the hot IGM was not necessarily in place. In this phase, traditional approaches to cluster detection (X-ray and SZ surveys, searches for galaxy red sequences) work only for the more evolved objects; indeed these methods have yielded only a handful of confirmed proto-clusters at $z \gtrsim 1.5$ [146]⁴. *Planck* has demonstrated the power of low-resolution surveys for the study of large-scale structure [147] but its resolution was too poor to detect individual proto-clusters [135]. Studies of the high- z 2-point correlation function [107, 135] and *Herschel* images of the few sub-mm bright protoclusters detected so far, at z of up to 4 [148–150], all of which will be detected by PICO, indicate sizes of $\simeq 1'$ for the cluster cores, nicely matching the PICO FWHM at the highest frequencies.

⁴More high- z proto-clusters have been found targeting the environment of tracers of very massive halos, such as radio-galaxies, QSOs, sub-mm galaxies. These searches are however obviously biased.

PICO will detect many tens of thousands of these objects – this is the blue line in the right-hand panel of Fig. 2.12 – as peaks in its sub-mm maps, in addition to the evolved ones, detected by the SZ effect. This will constitute a real breakthrough in the observational validation of the formation history of the most massive dark matter halos, traced by clusters, a crucial test of models for structure formation. Follow-up observations will characterize the properties of member galaxies, probing the galaxy evolution in dense environments and shedding light on the complex physical processes driving it.

2.3.3 Additional products of PICO surveys

PICO will also yield a complete census of cold dust, available to sustain star formation in the nearby Universe, by detecting tens of thousands galaxies mostly at $z \lesssim 0.1$. Its statistics will allow us to investigate the distribution of such dust as a function of galaxy properties (morphology, stellar mass, etc.).

Moreover, PICO will increase by orders of magnitude the number of blazars selected at sub-mm wavelengths and will determine the SEDs of many hundreds of them up to 800 GHz and up to $z > 5$. Blazar searches are the most effective way to sample the most massive BHs at high z because of the Doppler boosting of their flux densities. Its surveys of the largely unexplored mm/sub-mm spectral region will also offer the possibility to discover new transient sources [151] or events, such as blazar outbursts.

PICO will also make a giant leap forward in the determination of polarization properties of both radio sources and of dusty galaxies over a frequency range where ground based surveys are impractical or impossible. Thanks to its high sensitivity, it will detect in polarization both populations over a substantial flux density range, determining directly, for the first time, number counts in polarized flux density and allowing an accurate correction for their contamination of CMB maps.

The anisotropy of the cosmic infrared background (CIB), produced by dusty star-forming galaxies in a wide redshift range, is an excellent probe of both the history of star formation and the link between galaxies and dark matter across cosmic time. The *Planck* collaboration derived values of the star formation rate up to redshifts $z \sim 4$ [152–154]. It was quantified in [155] that the increased SNR and frequency coverage enabled by PICO will enable an order of magnitude improvement on the statistical errors on these parameters. Similar improvement will be achieved in constraining M_{eff} , the galaxy halo mass that is most efficient in producing star formation activity. PICO extra-frequencies and increased sensitivity to Galactic dust polarization will provide enhanced means to separate the largely unpolarized CIB from polarized Galactic dust, the limiting factor towards more extended reliable legacy CIB maps.

2.4 Complementarity with Other Surveys and with Sub-Orbital Measurements

2.4.1 Complementarity with Astrophysical Surveys in the 2020s

PICO has strong complementarity with forthcoming surveys. Here we summarize areas of synergy that have been mentioned in a number of earlier sections.

Any refinement of the cosmological constraint on the sum of the neutrino mass $\sigma(\Sigma m_\nu) < 25 \text{ meV}$ will require improving *Planck*'s measurement of the optical depth τ . In particular, this applies to all methods that rely on comparing low-redshift structures with the amplitude of the CMB at high redshift, such as galaxy clustering, weak lensing, or cluster counts. PICO therefore complements all efforts that probe the late time structure of the Universe; combining PICO with these low-redshift observations extends the scientific reach of all these experiments well beyond

{acro:CIB}

Characteristic	Ground	Balloon	Space
Sky coverage	Partial from single site	Partial from single flight	Full
Frequency coverage	70 GHz inaccessible ^a $v \geq 300$ GHz unusable limited atmospheric windows	70 GHz inaccessible ^a otherwise, almost unlimited	Unrestricted
Angular resolution at 150 GHz ^b	1.5' with 6 m telescope	6' with 1.5 m telescope	6' with 1.5 m telescope
Detector Noise	$265 \mu\text{K}_{CMB}\sqrt{s}^c$	$124 \mu\text{K}_{CMB}\sqrt{s}^c$	$36 \mu\text{K}_{CMB}\sqrt{s}^c$
Integration time	Unlimited	Weeks to a Month	Continuous, for years
Accessibility, repairability	Good	None. Multiple flights possible.	None

^a 70 GHz is the frequency at which large angular scale B -mode Galactic emissions have a minimum.

^b We give representative approximate telescope aperture values. Significantly larger apertures for balloons and in space result in higher mass, volume, and cost.

^c Noise equivalent temperature: timestream-based median at 95 GHz from BICEP3 [156]; pre-flight expectation at 94 GHz from SPIDER [157]; at 90 GHz from PICO CBE.

Table 2.4: Relative characteristics of ground, balloon, and space platforms for experiments in the CMB bands.^[tab:comparison]

what they could achieve on their own.

Reconstructing the CMB lensing ϕ map on very large angular scales, $L < 20$, requires exquisite control of systematic uncertainties over a large sky fraction, with sufficient angular resolution to perform the lensing reconstruction, and with breadth in frequency band to robustly separate Galactic emissions (see Section 2.5). PICO will provide these, complementing ground-based CMB lensing reconstructions that typically observe a smaller sky fraction, with a smaller number of frequency bands, and without access to the largest angular scales. As discussed in page 14, PICO will robustly measure the lensing signal with a power spectrum SNR larger than 10 *per mode* on very large scales. Such high-significance CMB lensing measurements on the very largest scales will be useful when combined with measurements of galaxy clustering from LSST, Euclid, and SPHEREx (if selected), to search for local primordial non-Gaussianity via its scale-dependent effect on galaxy bias; see Section 2.2.1.

2.4.2 Complementarity with Sub-Orbital Measurements

Since the first CMB measurements, more than 50 years ago, important observations have been made from the ground, from balloons, and from space. Each of the CMB satellites flown to date - COBE, WMAP, and *Planck*- has relied crucially on technologies and techniques that were first proved on ground and balloon flights, making these also crucial to the success of PICO. The phenomenal success of, and the immense science outcomes produced by, past space missions is a direct consequence of their relative advantages, as listed in Table 2.4. In every respect, with the exception of serviceability, space has an experimental advantage. These advantages used to come with higher relative costs. However, with the advent of massive ground-based experiments this balance shifts; the costs for a CMB experiment planned for the next decade are squarely within the cost window of this Probe. We can thus point to the following general guidelines for the next decade.

When the entire sky is needed, as for fluctuations on the largest angular scales, space is by far the most suitable platform, and for the search for the IGW signal it is absolutely necessary. When broad frequency coverage is needed, space will be required to reach the ultimate limits set by astronomical foregrounds. As Fig. 2.1 and 2.13 demonstrate, Galactic emission overwhelms the IGW signal on the largest angular scales, and they are dominant even at high ℓ , potentially limiting the process of delensing that is necessary for reaching levels of $r \lesssim 0.001$. The stability offered in space can not be matched on any other platform and translates to superb control of systematic uncertainties. There is a broad consensus within the CMB community that for levels of $r \lesssim 0.001$ the challenges in the measurement are the ability to control systematic uncertainties and to remove

Galactic emissions; modern focal plane arrays, like the one employed by PICO have ample raw sensitivity. The PICO r goal of $\sigma(r) = 1 \times 10^{-4}$ is beyond the reach of ground observations. However, for science requiring higher angular resolution, such as observations of galaxy clusters with ~ 1 arcmin resolution at 150 GHz, the ground has a clear advantage. An appropriately large aperture on the ground will also provide high resolution information at lower frequencies, which may be important for separating Galactic emissions at high ℓ . A recommended plan for the next decade is therefore to pursue a space mission, and complement it with an aggressive ground program that will overlap in ℓ space, and will add science at the highest angular resolution, beyond the reach of a space mission.

Balloon observations have been exceedingly valuable in the past. They co-lead discoveries of the temperature anisotropy and polarization, provided proving grounds for the technologies enabling the success of COBE, WMAP and *Planck*, and trained the scientists that then led NASA’s space missions. There are specific areas for which balloon missions can continue to play an important role, despite their inherently limited observing time. Balloon payload can access frequency bands above 280 GHz; currently there are no plans for any ground program to conduct observations at higher frequencies. These frequency bands will provide important, and perhaps critical information about polarized emission by Galactic dust, a foreground that is currently known to limit knowledge of the CMB signals. With flights above 99% of the atmosphere, balloon-borne observations are free from the noise induced by atmospheric turbulence, making them good platforms for observations of the low ℓ multipoles, and for characterizing foregrounds on these very large angular scales. From a technology point of view, the near-space environment is the best available for elevating detector technologies to TRL6; and balloon-platforms continue to be an excellent arena for training the scientists of tomorrow.

2.5 Signal Separation

Diffuse Milky Way emissions dominate the sky’s polarized intensity on the largest angular scales (Fig. 2.1 and 2.13). Polarized radiation arises primarily from the synchrotron emission of energetic electrons spiralling in the magnetic field of our own Galaxy, and from thermal emission from elongated interstellar dust grains. Although the levels of these foreground emissions decrease with decreasing angular scales, they can still be considerably brighter than the IGW peak around $\ell = 80$ when averaging over 60% of the sky. In fact, even in the cleanest, smaller patches of the sky, far from the Galactic plane and thus relatively low in Galactic emissions, their levels are expected to be substantial relative to the IGW for $r \lesssim 0.01$, and dominate it for $r \lesssim 0.001$. Separating the cosmological and Galactic emissions signals, also called foreground separation, together with control of systematic uncertainties are *the* challenges facing any next decade experiment attempting to reach these levels of constraints on r .

The foreground separation challenge would be easily surmountable if the Galactic emissions were precisely characterized, or were known to have simple, fittable spectral emission laws. But neither is true. To first order, the spectrum of Galactic synchrotron emission, arising from free electrons spiraling around Galactic magnetic fields, can be modeled as a power law $I_{\text{sync}} \propto \nu^\alpha$, with $\alpha \simeq -1$ (in brightness units). The spectrum of Galactic dust emission, arising from emission by Galactic dust grains, can be modeled as $I_{\text{dust}} \propto \nu^\beta B_\nu(T_{\text{dust}})$, where $\beta \simeq 1.6$, $T_{\text{dust}} \simeq 19$ K, and $B_\nu(T)$ is the Planck function; this is referred to as ‘modified black body emission’. If those models were exact, then in principle, an experiment that had 6 frequency bands could determine the three emission parameters as well as the three amplitudes corresponding to that of dust, syn-

{sec:signal_separa}

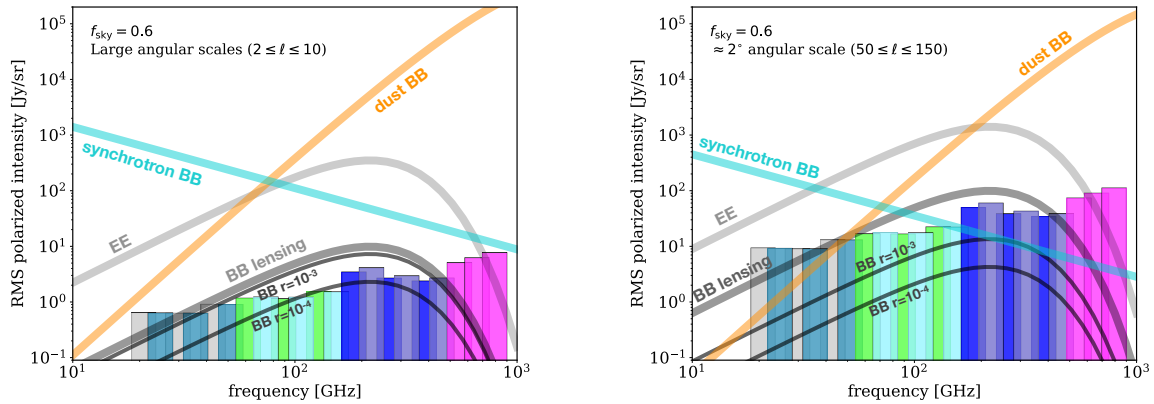


Figure 2.13: Polarization BB spectra of Galactic synchrotron and dust, compared to CMB polarization EE and BB spectra of different origins for two values of r and for two ranges of angular scales: large $\ell \leq 10$ corresponding to the reionization peak (left panel), and intermediate $50 \leq \ell \leq 150$ corresponding to the recombination peak (right panel). The location and sensitivity of the 21 PICO frequency channels is shown as vertical bands. (The color scheme is explained in Section 3.2.)

{fig:pico-channels}

chrotron, and the CMB. However, recent observations have shown that neither emission law is universal, that spectral parameters vary with the region of sky [158–160], and thus that the analytic forms and parameter values given above are valid only as averages across the sky. Also, while both emission laws are well-motivated phenomenological descriptions, the fundamental physics of emissions from grains of different materials, sizes and temperatures, and of electrons spiraling around magnetic fields implies that these laws are not expected to be exact, nor universal.

Additional polarized foregrounds may exist. ‘Anomalous microwave emission’ (AME) is observed at mm wavelengths, spatially correlated with thermal dust emission but with intensity peaked at frequencies near 30 GHz. While not known to be polarized, even a small (0.1%) fractional polarization would be appreciable for $\sigma(r) \lesssim 0.001$. Astrophysical emission from CO lines at mm wavelengths, and even small polarization of radio and infrared sources at shorter wavelengths could also complicate polarized signal separation [161, 162].

PICO will dramatically improve sensitivity to inflationary B-modes. The improved sensitivity requires concurrent improvements in foreground separation. Simple foreground models, suitable for the current generation of CMB measurements, will fail at the higher PICO sensitivity. For example, the Planck modified blackbody model assumes that interstellar dust emits at a single temperature, which is clearly an approximation to the more complicated emission along lines of sight spanning hundreds of pc. Several publications have demonstrated that fitting complicated temperature profiles using a simple one- or two-temperature model will bias the fitted CMB signal at levels $\delta r \lesssim 10^{-3}$, large compared to the PICO goal [163–167].

Foreground uncertainties, and the level of fidelity required in their characterization, also compel a transition in the way we assess and forecast the performance of a future experiment. We can no longer impose specific models upon the data; rather, the data collected should provide information to constrain Galactic emissions with sufficient accuracy. Two broad techniques are available. Parametric models use the frequency dependence of the data in each line of sight to determine the effective frequency dependence of foreground emission. Since the CMB spectrum is well determined, measurements with sufficiently broad frequency coverage can distinguish foreground

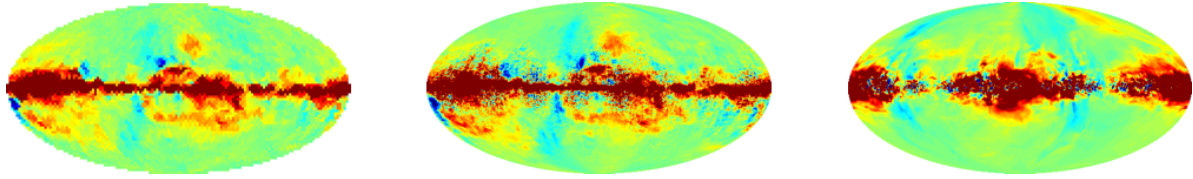


Figure 2.14: Foregrounds maps: Planck real sky (left) at 143 GHz, models at 155 GHz from PySM (middle) [168] and Galactic MHD simulations (right).

{fig:pysm_foreground}

emission from the CMB component by their different spectral dependences. Non-parametric techniques, in contrast, rely on the fact that CMB emission is uncorrelated with the foregrounds and use both spatial and frequency correlations within a spatial/frequency data cube to separate CMB from foreground components. Simulated data assess the efficacy of both techniques as a function of increasing complexity for the assumed foreground emission.

To investigate the capacity of PICO to address this foreground separation problem, we use the approach that has become the ‘gold standard’ in the community. In this approach we simulate sky maps that are constrained by available data, but otherwise have a mixtures of foreground properties. We ‘observe’ these maps just like a realistic experiment will do, and then apply foreground separation techniques to separate the Galactic and CMB emissions. We also provide forecasts using other techniques that use analytic calculations to estimate the efficacy of foreground separation, or others in which the simulated sky map is assumed to have specific Galactic emission models, which are then being fitted.

2.5.1 PICO Foreground Separation Methodology

For assessing the efficacy of foreground separation with PICO we used 8 different full-sky models. All models were broadly consistent with available data and uncertainties from WMAP and *Planck*. The range of models included one test case that had a very simple realization of foregrounds, and others with varying degree of complexity including spectral parameters varying spatially and along the line of sight, anomalous microwave emission up to 2% polarized, dust polarization that rotates slightly as a function of frequency because of projection effects, or dust spectral energy distribution that departs from a simple modified blackbody. All foreground maps were generated at native resolution of 6.8 arcmin pixels [169]. They were generated using PySM and/or PSM codes [168, 170]. Distinctly different realizations of the sky are allowed by current data, as demonstrated by Fig. 2.14.

For each of the 8 models we added CMB signals in both intensity and polarization matching a Λ CDM universe. The BB -lensing signal matched the level of 85% delensing forecasted for PICO. Each of these sky models had 100 different realization of the PICO CBE noise levels; 50 realizations had no IGW signal and 50 others had a level of $r = 0.003$. The sky models were analyzed with a variety of techniques which were based on the two broad categories described above.

Analytic forecasts were based on a Fisher information matrix approach [171] and included foreground separation using a parametric maximum-likelihood approach, assuming the foreground spectral indices are constant on patches of size 15 degrees across.

2.5.2 Results and Discussion

There is evidence that at levels of $r \simeq 0.001$ the combination of PICO’s sensitivity and broad frequency coverage are efficacious in foreground removal. Fig. 2.15 shows a result from the gold

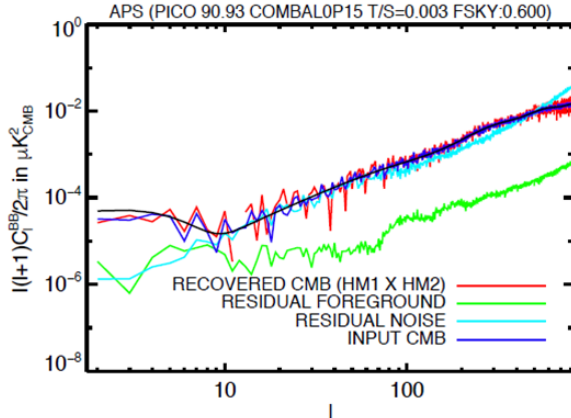


Figure 2.15: The power spectrum of residual BB foregrounds (green) has lower level than both the input CMB (blue) and the recovered CMB (red) which match well each other and the underlying cosmological model (black) after foreground separation with the NILC algorithm. This exercise assumed use of 60% of the sky. [fig:nilc](#)

standard process described above for one of the sky models and with an input IGW of $r = 0.003$. Residual foregrounds are below the cosmological signal over the important low ℓ range, where foregrounds are strongest. The residual spectra would likely be lower when analysis is carried out on only 50 or 40% of the sky, rather than the 60% used here.

Our results validate the need for a broad frequency coverage with a strong lever arm on Galactic emissions outside of the primary CMB bands. Fig. 2.16 shows that removing several of PICO’s frequency bands, particularly those that monitor dust and synchrotron at high and low frequencies, respectively, significantly biases the extracted BB power spectrum, particularly at the lowest ℓ values.

There is other evidence that PICO could reach its stated target of $\sigma(r) = 0.0001$. Map-based simulations that were carried out for the forthcoming CMB-S4 experiment have shown that it can reach levels of $\sigma(r) = 0.0005$ in small, 3%-size, clean patches of the sky. The PICO noise level per sky pixel is similar to that of CMB-S4, but PICO will have *full* sky coverage and thus access to *all* the clean patches available. Data from *Planck* indicate that there are ~ 10 patches as clean, or cleaner than those used for the CMB-S4 analysis, indicating that PICO’s $\sigma(r)$ could be about three times more stringent. This scaling is very conservative because it only assumes CMB-S4’s much narrower breadth of frequency coverage and its 7 bands; it neglects PICO’s much stronger rejection of foregrounds with 21 bands and up to 800 GHz. We note that if there *is* a detection of the IGW signal with $r = 0.001$, PICO will make it with high significance in multiple independent patches of the sky.

Results from the Fisher-based analytic calculations give $\sigma(r) = 9 \cdot 10^{-5}$, and indicate a very small foreground residual with an $r_{\text{eff}} = 9 \cdot 10^{-7}$.

While our results are encouraging, as they suggest that PICO’s frequency coverage and sensitivity will be adequate for this level of r , more work should be invested to gain complete confidence. This work includes running numerous realizations of different sky models, and analyzing them with various techniques; optimizing sky masks; and using combination of techniques to handle large, intermediate, and small angular scale foregrounds differently.

2.6 Systematic Uncertainties

Some of the PICO science goals attempt to detect extremely faint signals. The most ambitious one is to reach the signals characterizing an inflationary gravity wave with $r \lesssim 0.001$, with a B-mode polarization peak signal $\lesssim 10\text{nK}$ in amplitude at $\ell = 80$. It has long been recognized that exquisite control of systematic uncertainties will be required for any experiment attempting to reach these levels, and it is widely accepted that the stability provided aboard a space platform makes it best

{sec:systematics}

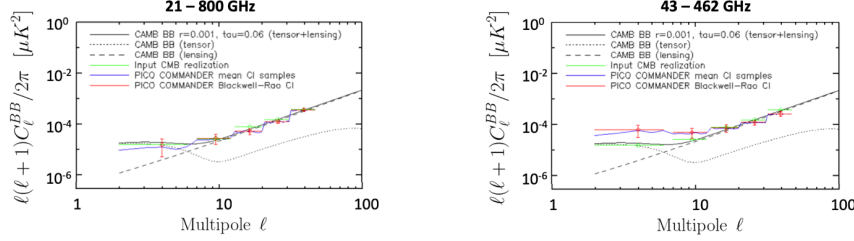


Figure 2.16: Foreground removal with all of PICO’s 21 frequency bands (left panel) recovers the input CMB (green) without any bias (red) using the Commander algorithm on the *Planck* sky model (with 4 deg pixels, and 50% sky fraction). Running the same algorithm on the same sky without several of the lowest and highest bands (right panel) produces an output spectrum (red) that is biased relative to the input (green) at low ℓ multipoles. The bias would be interpreted as higher value of r relative to the model input (solid black) with $r = 0.001$ (dots) and lensing (dash). | [fig:commander](#)

suited to control systematic uncertainties compared to other platforms. This is one of the most compelling reasons to observe the CMB from space. As WMAP and *Planck* demonstrated, an L2 orbit offers excellent stability as well as the flexibility in the choice of scan strategy. PICO takes advantage of an L2 orbit, using a rotating spacecraft (at 1 rpm) whose spin axes precesses with a 10 hour period, thus scanning the sky in a way that is crosslinked on many time scales and at many angles, without interference from the Sun, Earth, or Moon, thus reducing the effects of low frequency excess noise without additional modulation. The redundancy of observations allows the checking of consistency of results and an improved ability to calibrate and to correct systematic errors in post-processing analysis.

A rich literature investigates the types of systematic errors due to the environment, the instrumentation, observation strategies, and data analysis that confound the polarization measurement by creating a bias or an increased variance[172–174]. Every measurement to date has reached a systematic error limit, and have advanced many sophisticated techniques to mitigate systematics, finding both new technological solutions and new analysis techniques. As an example, the BICEP’s systematics limited it to $r=0.1$ [175] while through additional effort within the program, BICEP2 achieved a systematics limit of $r=6 \times 10^{-3}$ [176]. In the near term, the ground based and suborbital CMB community will continue to develop new techniques in handling systematics, particularly in developing the CMB-S4 project.

All prior on-orbit measurements of CMB polarization were limited by systematic errors until an in-depth study of the systematics was performed and the post-processing data analysis suppressed them[21, 43, 177]. Particularly we note Fig. 3 of [21] which quantifies *Planck*’s systematic error limits on the polarization power spectral measurements. Recently studied space missions, such as EPIC-IM, LiteBird and *CORE*, have placed systematic error mitigation at the forefront of the case for their mission and have developed tools and strategies for estimating and mitigating these[178–180].

Systematics are coupled with the spacecraft scan strategy, and the details of the data analysis pipeline. Thus, end-to-end simulation of the experiment is an essential tool, including realistic instabilities and non-idealities of the spacecraft, telescope, instrument and folding in data post-processing techniques used to mitigate the effects.

2.6.1 List of Systematics

The systematic errors faced by PICO can be categorized into three broad categories: 1) Intensity-to-polarization leakage, 2) stability, and 3) straylight, and are listed in Table 2.5. These were prioritized for further study using a risk factor incorporating the working group's assessment of how mission-limiting the effect is, how well these effects are understood by the community and whether mitigation techniques exist.

The three highest risk systematic errors were studied further and are discussed in subsections below. The PICO team used simulation and analysis tools developed for Planck[181] and *CORE*, adapting them for PICO.

Name	Risk	Effect	
Leakage			
Polarization Angle Calibration.....	5	$E \rightarrow B$	See Sect. 2.6.2
Bandpass Mismatch.....	4	$T \rightarrow P, E \rightarrow B$	
Beam mismatch	4	$T \rightarrow P, E \rightarrow B$	See Sect. 2.6.2
Time Response Accuracy and Stability.....	4	$T \rightarrow P, E \rightarrow B$	
Readout Cross-talk.....	4	spurious P	
Chromatic beam shape	4	spurious P	
Gain mismatch	3	$T \rightarrow P$	
Cross-polarization	3	$E \rightarrow B$	
Stability			
Gain Stability	5	$T \rightarrow P, E \rightarrow B$	See Sect. 2.6.3
Pointing jitter.....	3	$T \rightarrow P, E \rightarrow B$	
Straylight			
Far Sidelobes.....	5	spurious P	See Sect. 2.6.4
Other			
Residual correlated noise (1/f, cosmic ray hits)	3	increased variance	

Table 2.5: Systematic errors expected in PICO's measurement of CMB polarization. Each source of systematic errors was given a rating of the risk that a given systematic error will dominate the B-mode measurement. A risk level of 5 indicates that a systematic effect is highly significant because it is design-driving, has limited past experiments, and/or isn't well understood. Risk level of 4 indicates a systematic that is either known to be large but is understood reasonably well or a smaller effect that requires precise modeling. Risk level of 3 indicates that we expect the effect to be small, but it isn't necessarily well understood enough that modeling it should be done in detail in a mission Phase A. This study investigated the systematics with risk levels of 5 via simulations.

2.6.2 Absolute polarization angle calibration

CMB polarization can be rotated due to 1. a birefringent primordial Universe, or a Faraday rotation due a primordial magnetic field [182], 2. birefringent foregrounds, or interaction with the Galactic magnetic field, 3. systematic effects in the instrument, and in particular an error on the direction of polarization measured by each detector. While the first two sources create a rotation that may depend on scale, position and/or frequency, the latter depends mainly on the detector.

A rotation α of the direction of polarization mixes the Q and U Stokes parameters via $Q \pm iU \rightarrow e^{\mp i2\alpha} (Q \pm iU)$ and thus mixes the power spectra and their correlations as illustrated in Fig. 2.17.

The most recent constraints on cosmological birefringence [183] were limited by uncertainties on the detector orientations. In Planck, the detectors were characterized pre-launch to $\pm 0.9^\circ$ (rel.) $\pm 0.3^\circ$ (abs.) [184]. For PICO, the relative rotation of the detectors will be measured to a few $0.1'$ using the CMB, but the overall rotation is unlikely to be known pre-launch to better than Planck. Known polarized sources, such as the Crab Nebula, are not characterized well enough independently to serve as calibrators; (**author?**) [185] show that the current uncertainty of $0.33^\circ = 20'$ on the Crab polarization orientation, limits a B mode measurement to $r \sim 0.01$, far from PICO's target.

In the absence of other systematics and foregrounds, a polarization rotation error α of $10'$

{sec:angle}

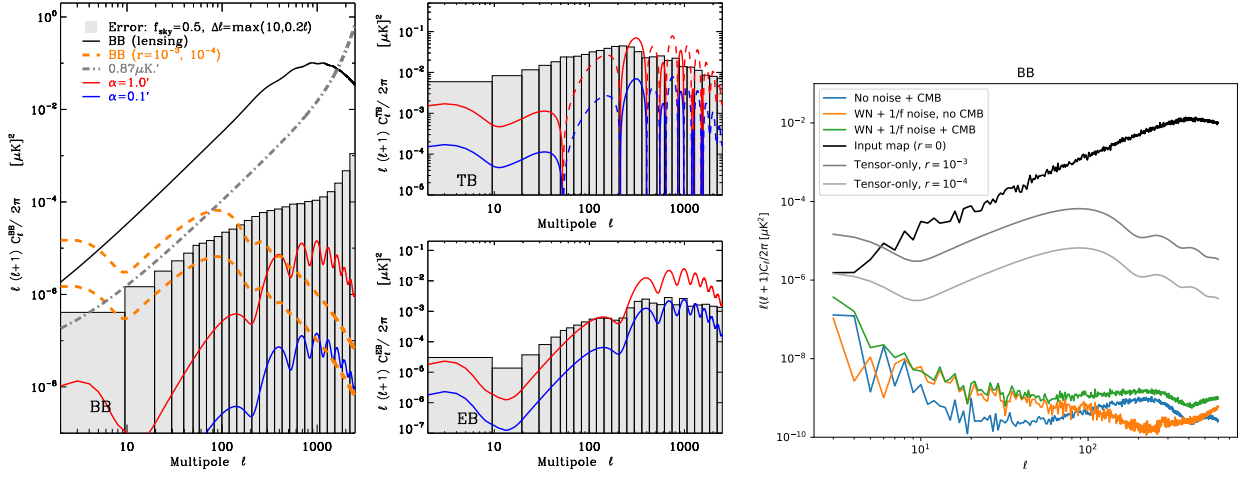


[fig:rot_bb_tb_eb](#)
Figure 2.17: |Left and center: Spurious power due to a rotation of the angle of polarization, assuming the Planck 2018 Λ -CDM model [42] with $\tau = 0.054$ and expected PICO noise performance, assuming removal of 85% of the lensing power. Right: residual power after removal of temporal gain drifts using the dipole.

degrades the error bar of r by 30%, while EB , TB and BB spectra can measure a rotation α at 3σ when $\alpha \sim 0.07, 0.2$ and $0.9'$ respectively on perfectly delensed maps, and $0.25, 0.9$ and $4.5'$ on raw maps.

In principle, the technique of using the TB and EB spectra can detect and measure a global polarization rotation error at levels ($0.1'$) below those affecting r measurements in BB ($> 1'$). However, a future mission should simulate additional aspects, such as delensing, the interaction with foregrounds, and $1/f$ noise in simulating and assessing the impact of an angle calibration error.

2.6.3 Gain Stability

Photometric calibration is the process of converting the raw output of the receivers into astrophysical units via the characterization of the *gain factor* $G(t)$ which we allow to vary with time. In space, $G(t)$ can be measured with the dipole. For the PICO concept study, we evaluated the impact of noise in the estimation of $G(t)$ using the tools developed for the Planck/LFI instrument and the CORE mission proposal. The quality of the estimate depends on the noise level of the receivers, but also on the details of the scanning strategy. To analyze the impact of calibration uncertainties on PICO, we performed the following analysis: 1. We simulated the observation of the sky, assuming four receivers, the nominal scanning strategy, and $1/f$ noise. The simulated sky contained CMB anisotropies, plus the CMB dipole. 2. We ran the calibration code to fit the dipole against the raw data simulated during step 1. 3. We again simulated the observation of the sky, this time using the values of G computed during step 2, which contain errors due to the presence of noise and the CMB signal.

The presence of large-scale Galactic emission features can bias the estimation of calibration factors. Ideally, a full data analysis pipeline would pair the calibration step with the component separation step, following a schema similar to Planck/LFI's legacy data processing[186]: the calibration code is followed by a component separation analysis, and these two steps are iterated until the solution converges.

Results of the simulation (neglecting foregrounds) are shown as power spectrum residuals in

{sec:gain}

Fig. 2.17. We estimate the gain fluctuations to better than 10^{-4} solving for the gain every 40 hours (4 precession periods). The scanning strategy employed by PICO allows for a much better calibration than Planck, thanks to the much faster precession.

2.6.4 Far Sidelobe Pickup

Measurement of each detector's response to signals off axis, which tends to be weak (-80dB less than the peak response) but spread over a very large solid angle, is difficult to do pre-launch, and may not even be done accurately after launch. Nonetheless, this far sidelobe can couple bright Galactic signal from many tens of degrees off-axis and confuse it with polarized signal from the CMB off the Galactic plane. To evaluate this systematic error, GRASP software⁵ was used to compute the PICO telescope's response over the full sky. The computed full-sky beams showed features peaking at about -80 dB of the on-axis beam. This full-sky beam was convolved with a polarized Galactic signal and a one-year PICO mission scan using the simulation pipeline and preliminarily shows that the far sidelobe pickup must be calculated accurately down to the 90 dB level in order to be removed from the measured B-mode signal to a level that does not appreciably increase the variance on the B-mode power measurement.

{sec:fsl}

2.6.5 Key Findings

Properly modeling, engineering for, and controlling the effects of systematic errors in a next-generation CMB probe is critical. As of today, we conclude that there is a clear path to demonstrate that state-of-the-art technology and data processing can take advantage of the L2 environment and control systematic errors to a level that enables the science goals of PICO. In particular we note:

- The raw sensitivity of the instrument should include enough margin that data subsets can independently achieve the science goals. This allows testing of the results in the data analysis and additional data cuts, if needed.
- In a PICO mission, a physical optics model of the telescope should be developed, enabling full-sky beam calculations, which should be validated as much as possible on the ground. This will be needed to characterize and remove far sidelobe pickup seen during the mission.
- NASA's support of ground-based and suborbital CMB missions will mitigate risk to a future space mission as PICO by continuing to develop analysis techniques and technology for mitigation of systematic errors.
- In a PICO mission's phase A, a complete end-to-end system-level simulation software facility would be developed to assist the team in setting requirements and conducting trades between subsystem requirements while realistically accounting for post-processing mitigation. Any future CMB mission is likely to have similar orbit and scan characteristics to those of PICO, thus there is an opportunity for NASA and the CMB community to invest in further development of this capability now.
- Low frequency excess noise (also called 1/f noise) should be studied in detail as part of a simulation effort to set detailed detector and systems level requirements. The systematics simulations performed here show that PICO's science goals can be achieved with no additional modulation and assuming current state-of-the-art levels of low frequency noise (a total knee frequency of 20 mHz) based on demonstrated TES performance, and system-level residuals achieved by Planck.

⁵<https://www.ticra.com>

2.7 Measurement Requirements

The set of physical parameters and observables that derive from the PICO science objectives place requirements on the depth of the mission, the fraction of sky the instrument scans, the frequency range the instrument probes and the number of frequency bands, the angular resolution provided by the reflectors, and the specific pattern with which PICO will observe the sky. We discuss each of these aspects.

• **Depth** We quantify survey depth in terms of the RMS fluctuations that would give a signal-to-noise ratio of 1 on a sky pixel that is 1 arcminute on a side. Depth in any frequency band is determined by detector sensitivity, the number of detectors in the focal plane, the sky area covered, and the duration of the mission. The science objective driving the depth requirement is SO1, the search for the IGW signal which requires a depth of $0.87 \mu\text{K} \cdot \text{arcmin}$. This requirement is a combination of the low-level of the signal, the need to separate the various signals detected in each band, and the need to detect and subtract systematic effects to anticipated levels. The CBE value is $0.61 \mu\text{K} \cdot \text{arcmin}$ coming from a realistic estimate of detector noise, and giving 40% margin on mission performance.

• **Sky Coverage** There are several science goals driving a full sky survey for PICO. The term ‘full sky’ refers to the entire area of sky available after separating other astrophysical sources of confusion. In practice this implies an area of 50-70% of the full sky for probing non-Galactic signals, and the rest of the sky for achieving the Galactic science goals.

(1) Probing the optical depth to the epoch of reionization (STM SO5) requires full sky coverage as the signal peaks in the EE power spectrum on angular scales of 20 to 90 degrees. Measuring this optical depth to limits imposed by the statics of the small number of available ℓ modes is crucial for minimizing the error on the neutrino mass measurement.

(2) If $r \neq 0$, the BB power spectrum due to IGW (STM SO1) has local maxima on large angular scales (20 to 90 degrees, $2 \leq \ell \leq 10$), and around 1 degree ($\ell \simeq 80$). A detection would strongly benefit from confirmation at *both* angular scales – a goal that is beyond the capabilities of ground-based instruments – and, for the $\ell = 80$ peak, *in several independent patches of the sky*, a goal PICO will achieve, but that is currently not planned for any next decade instrument.

(3) The PICO constraint on N_{eff} (STM SO4) requires a determination of the EE power spectrum to limits imposed by the statics of available ℓ modes. Full sky coverage is required to achieve this limit.

(4) Achieving the neutrino mass limits (STM SO3), giving two independent 4σ constraints on the minimal sum of 58 meV, requires a lensing map, and cluster counts from as large a sky fraction as possible.

(4) PICO’s survey of the Galactic plane and regions outside of it is essential to achieving its Galactic structure and star formation science goals (SO6, 7).

• **Frequency Bands** The multitude of astrophysical signals that PICO will characterize determine the frequency range and number of bands that the mission uses. The IGW signal peaks in the frequency range between 30 and 300 GHz. However, Galactic signals, which are themselves signals PICO strives to characterize, are a source of confusion for the IGW. The Galactic signals and the IGW are separable using their spectral signature. Simulations indicate that 21 bands, each with $\sim 25\%$ bandwidth, that are spread across the range of 20 - 800 GHz can achieve the separation at the level of fidelity required by PICO.

Characterizing the Galactic signals, specifically the make up of Galactic dust (SO7), requires

{requirements}

spectral characterization of Galactic dust in frequencies between 100 and 800 GHz.

• **Resolution** Several science objectives require an aperture of 1.5 m and the resolution per frequency listed in Table 2.2. To reach $\sigma(r) = 1 \cdot 10^{-4}$ we will need to ‘delens’ the E - and B -mode maps, as described in Sections 2.2.1 and 2.2.2. Delensing is enabled with a map that has a native resolution of 2-3 arcminutes at frequencies between 100 and 300 GHz. Similar resolution is required to achieve the constraints on the number of light relics (SO4), which will be extracted from the EE power spectrum at multipoles $100 \lesssim \ell \lesssim 2500$. The process of delensing may be affected by other signals, primarily the signal due to Galactic dust. It is thus required to map Galactic dust to at least the same resolution as at 300 GHz. Higher resolution is mandated by SO6 and 7, which require resolution of 1 arcminute at 800 GHz. We have thus chosen to implement diffracted limited resolution between 20 and 800 GHz.

• **Sky Scan Pattern** Control of polarization systematics uncertainties at anticipated levels is enabled by (1) making I , Q , and U Stokes parameters maps of the entire sky from each independent detector; and (2) by enabling sub-percent absolute gain calibration of the detectors through observations of the CMB dipole. With these requirements we chose a sky scan pattern that enables each detector to scan a given pixel of the sky in multitude of directions, satisfying requirement (1). The scan we chose also gives strong CMB dipole signals in every rotation of the spacecraft throughout the lifetime of the mission, satisfying requirement (2).

3 Instrument

PICO meets all of its science-derived instrument requirements (Table 2.2) with a single instrument: an imaging polarimeter with 21 frequency bands centered between 21 and 799 GHz. The instrument is built around a two-reflector Dragone-style telescope (§ 3.1) with an internal aperture stop between the primary and secondary. The focal plane is populated by 12,996 transition edge sensor (TES) bolometers (§ 3.2) read out using a time-domain multiplexing scheme (§ 3.3). The instrument employs a single science observing mode: fixed rotation-rate imaging while scanning the sky.

A V-groove radiator assembly provides passive cooling (§ 3.4.3). The instrument is configured inside the shadow of the V-grooves, thermally and optically shielded from the Sun. The sun shadow cone depicted in Figure 3.1 is 29° . The angle to the Sun during the survey, $\alpha = 26^\circ$ (§ 4.1.2 and Fig. 4.2), is supplemented with a margin of 3° to account for the radius of the sun (0.25°), pointing control error, design margin, and alignment tolerances.

The V-groove assembly is attached to the bipod struts that support the instrument structural ring. The ring supports the primary reflector and telescope box. The telescope box contains the actively cooled components (§ 3.4.1, § 3.4.2), including the secondary reflector, the focal plane and sub-kelvin adiabatic refrigerator structures. Just inside the box, a thermal liner serves as a cold optical baffle and aperture stop.

During the survey, the instrument is spun at 1 rpm (§ 4.1.2). Spacecraft control is simplified by mounting the instrument on a spinning spacecraft module, while a larger non-spinning module houses most spacecraft subsystems (§ 4.3). Instrument elements that act as heat sources are accommodated on the spinning module of the spacecraft. Instrument integration and test (I&T) is described in § 3.5.

3.1 Telescope

PICO telescope design is driven by a combination of science requirements and physical volume limits. The science requirements are: a large diffraction-limited field of view (DLFOV) sufficient to support $\sim 10^4$ detectors, arcminute resolution at 800 GHz, low spurious polarization, and low sidelobe response. All requirements are met with PICO’s 1.4 m aperture modified open-Dragone design. There are no moving parts in the PICO optical system.

The PICO optical design was selected following a trade study examining cross-Dragone, Gregorian Dragone, and open-Dragone designs [187]. The open-Dragone and crossed-Dragone offer more diffraction-limited focal plane area than the Gregorian Dragone [188], and are able to support enough detectors to provide the required sensitivity. The open-Dragone does not require the massive and voluminous baffles that the cross-Dragone does, and hence can satisfy the aperture size requirement within the shadow cone.

PICO’s initial open-Dragone design has been modified by adding an aperture stop and adding corrections to the primary and secondary reflectors to enlarge the DLFOV. The detailed geometric parameterization of the PICO optical design is described in [187]. The primary reflector ($270\text{ cm} \times 205\text{ cm}$) is passively cooled and the secondary reflector ($160\text{ cm} \times 158\text{ cm}$) is actively cooled. The highest frequency (900 GHz) sets the surface accuracy requirement of the reflectors to $\sim \lambda/14 = 24\mu\text{m}$. The focal ratio is 1.42. The slightly concave focal surface, which has a radius of curvature of 4.55 m, is telecentric to within 0.12° across the entire FOV.

An actively cooled circular aperture stop between the primary and secondary reflectors reduces

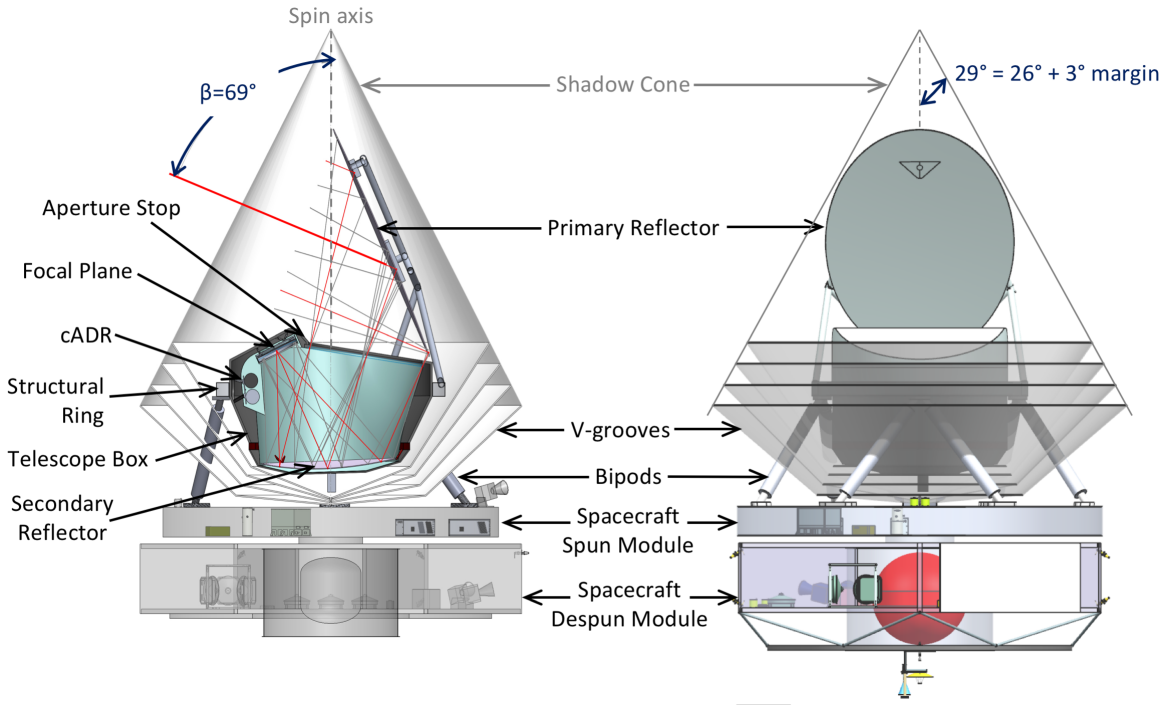


Figure 3.1: Detailed PICO instrument configuration. There are no moving or deployed parts. The spacecraft spun module accommodates warm instrument components: the 4 K cooler compressor and drive electronics, the sub-K cooler drive electronics, and the detector warm readout electronics. [Figure to be updated!](#)
fig:InstrumentCAD

detector noise and shields the focal plane from stray radiation. Stray-light analysis of the PICO open-Dragone design using GRASP confirms that the focal plane is protected from direct view of the sky, and that spillover past the primary is suppressed by 80 dB relative to the main lobe for both co-pol and cross-pol beams. Detailed baffle design will be performed during mission formulation.

3.2 Focal plane

PICO's focal plane is populated by an imaging array of transition edge sensor (TES) bolometers observing in 21 overlapping frequency bands with 25% fractional bandwidth and band centers ranging from 21 to 799 GHz. Polarization is measured by differencing the signals from pairs of polarization-sensitive bolometers. A conceptual layout of the PICO focal plane is shown in Figure 3.2 and detailed in Table 3.1.

Modern mm/sub-mm detectors are photon-noise limited, so the primary approach to increase sensitivity is to increase the number of detectors. The PICO focal plane has 12,996 detectors, 175 times the number flown on the *Planck* mission, providing a breakthrough increase in sensitivity with a comparably sized telescope. This breakthrough is enabled by development and demonstration in suborbital projects, which now commonly operate arrays of 10^3 – 10^4 detectors (§ 5).

3.2.1 21–462 GHz bands

The majority of the PICO FOV is populated with multichroic pixels (MCPs) [189, 190], which make optimal use of the focal plane area by feeding three photometric bands from a common broadband antenna, with two single-polarization bolometers per band and therefore six bolometers per pixel.

{sec:focal_plane}

{sec:low_freq_det}

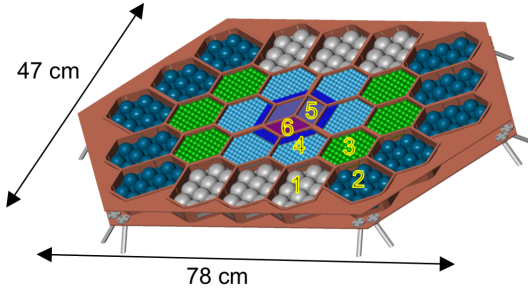


Figure 3.2: PICO focal plane. Detectors are fabricated on six types of tiles (shown numbered and colored as in Table 3.1). The wafers are located on the focal plane such that higher frequency bands, which require better optical performance, are placed nearer to the center.
[fig:FocalPlaneMechanical](#)

Table 3.1: PICO makes efficient use of the focal area with multichroic pixels (three bands per pixel, § 3.2.1). The sampling rate is based on the smallest beam (Table 3.2), with 3 samples per FWHM at a scan speed (360°/min) $\sin(\beta = 69^\circ) = 336^\circ/\text{min}$. [Table to be updated \[Tim\]](#).
[tab:focal_plane](#)

Tile type	N_{Tile}	Pixels / Tile	Pixel type	Bandcenters [GHz]	Sampling Rate [Hz]
1	6	10	A	21, 30, 43	45
2	10	10	B	25, 36, 52	55
3	6	61	C	62, 90, 129	136
4	6	85	D	75, 108, 155	163
		80	E	186, 268, 385	403
5	2	450	F	223, 321, 462	480
6	1	220	G	555	917
		200	H	666	
		180	I	799	

Several competing optical coupling technologies have matured over the past ten years using horn-coupling [191], antenna-array coupling [192], and sinuous antenna/lenslet-coupling [193], delivering quantum efficiency $> 70\%$ over more than an octave of bandwidth. Pixel size, number, and spacing are relatively agnostic to the coupling scheme, so multiple options are open to PICO (technology maturation plan described in § 5.2). For all of these schemes, niobium microstrips mediate the signals between the antenna and detectors, and partition the feed’s wide continuous bandwidth into narrow channels using integrated micro-machined filter circuits [194].

3.2.2 555–799 GHz bands

PICO’s highest three frequency channels are beyond the niobium superconducting band-gap, rendering microstrip filters a poor solution for defining the optical passband. In this regime, PICO instead measures a single band with each pixel using feedhorn-coupled polarization-sensitive bolometers. Radiation is coupled through horns directly to absorber in the throat of a waveguide. TES bolometers detect the incident power. The waveguide cut-off defines the lower edge of the band, and quasi-optical metal-mesh filters define the upper edge. Numerous experiments have successfully used similar approaches [195–197]. The technology maturation required for PICO is described in § 5.2.

3.2.3 Sensitivity

PICO’s Current Best Estimate (CBE) sensitivity meets the requirements of the baseline mission with $> 40\%$ margin (Table 3.2).

We developed an end-to-end noise model of the PICO instrument to predict full mission sensitivity and provide a metric by which to evaluate mission design trades. The model considers four noise sources per bolometer: photon, phonon, TES Johnson, and readout (from both cold and warm readout electronics). To validate our calculations, we compared two independent software packages that have been validated by test on several CMB instruments. The calculations agreed within 1% both for individual noise terms and for overall mission noise.

Laboratory experiments have demonstrated that TES detectors can be made background-limited in the low loading environment they would experience at L2 [198]. For PICO, the primary contributor to noise is the optical load. The sources of optical load are the CMB, reflectors, aperture stop, and low-pass filters. The CMB and stop account for the majority of the optical load at all frequencies. The CMB gives more than half the load in the middle and upper bands of the multichroic pixels, but the stop dominates the load in the lowest band of each pixel.

A detailed description of the PICO noise model and its inputs is available in [187]. Small differences from Table 3.2 are due to refinements of the component temperatures.

The sensitivity model assumes white noise at all frequencies. Sub-orbital submillimeter experiments have demonstrated TES detectors that are stable to at least as low as 20 mHz [199], meeting the requirements for PICO’s scan strategy (§ 4.1.2).

3.3 Detector readout

Suborbital experiment teams over the past ten years have chosen to use voltage-biased TESs because their current readout scheme lends itself to Superconducting Quantum Interface Device (SQUID) based multiplexing. Multiplexing reduces the number of wires to the cryogenic stages and thus the total thermal load that the cryocoolers must dissipate. This approach also simplifies the instrument design.

{sec:high_freq_det}

{sec:sensitivity}

{sec:detector_read}

Table 3.2: PICO measures in 21 broad overlapping frequency bands with band centers (v_c) from 21 GHz to 799 GHz and bandwidth $\Delta v/v_c = 25\%$. The beams are single mode, with FWHM sizes of $6.2' \times (155\text{GHz}/v_c)$. The Current Best Estimate (CBE) per-bolometer sensitivity is background limited (§ 3.2.3). The total number of bolometers for each band is equal to (number of tiles) \times (pixels per tile) \times (2 polarizations per pixel), from Table 3.1. Array sensitivity assumes 90% detector operability. The map depth assumes 5 yr of full sky survey at 95% survey efficiency, except the 25 and 30 GHz frequency bands, which are conservatively excluded during 4 hr/day Ka-band (26 GHz) telecom periods (§ 4.2).^{tab:bands}

Band Center [GHz]	Beam FWHM [arcmin]	CBE Bolo NET [$\mu\text{K}_{\text{CMB}}/\sqrt{\text{s}}$]	N_{bolo}	CBE Array NET [$\mu\text{K}_{\text{CMB}}/\sqrt{\text{s}}$]	Required (Baseline) Array NET [$\mu\text{K}_{\text{CMB}}/\sqrt{\text{s}}$]	Baseline Polarization Map Depth	
						$\mu\text{K}_{\text{CMB}}/\text{arcmin}$	Jy/sr
21	38.4	112.2	120	12.0	17.0	23.9	8.3
25	32.0	103.0	200	8.4	11.9	18.4	10.9
30	28.3	59.4	120	5.7	8.0	12.4	11.8
36	23.6	54.4	200	4.0	5.7	7.9	12.9
43	22.2	41.7	120	4.0	5.6	7.9	19.5
52	18.4	38.4	200	2.8	4.0	5.7	23.8
62	12.8	69.2	732	2.7	3.8	5.4	45.4
75	10.7	65.4	1020	2.1	3.0	4.2	58.3
90	9.5	37.7	732	1.4	2.0	2.8	59.3
108	7.9	36.2	1020	1.1	1.6	2.3	77.3
129	7.4	27.8	732	1.1	1.5	2.1	96.0
155	6.2	27.5	1020	0.9	1.3	1.8	119.1
186	4.3	70.8	960	2.0	2.8	4.0	433.1
223	3.6	84.2	900	2.3	3.3	4.5	604.2
268	3.2	54.8	960	1.5	2.2	3.1	433.4
321	2.6	77.6	900	2.1	3.0	4.2	577.8
385	2.5	69.1	960	2.3	3.2	4.5	429.1
462	2.1	132.6	900	4.5	6.4	9.1	551.1
555	1.5	657.8	440	23.0	32.5	45.8	1580
666	1.3	2212	400	89.0	125.8	177.2	2075
799	1.1	10430	360	525.9	743.8	1047	2884
		Total	12,996	0.43	0.61	0.87	

In the multiplexing circuitry, SQUIDs function as low-noise amplifiers and cryogenic switches. The current baseline for PICO is to use a time-domain multiplexer (TDM), which assigns each detector's address in a square matrix of simultaneously read columns, and sequentially cycles through each row of the array [200]. The PICO baseline architecture uses a matrix of 128 rows and 102 columns, requiring some technology maturation (§ 5.4). The thermal loading on the cold stages from the wire harnesses is subdominant to conductive loading through the mechanical support structures.

Because SQUIDs are sensitive magnetometers, suborbital experiments have developed techniques to shield them from Earth's magnetic field using highly permeable materials and superconducting materials [201]. Total suppression factors better than 10^7 have been demonstrated for dynamic magnetic fields [?]. PICO will use these demonstrated techniques to shield SQUID readout chips from the ambient magnetic environment, which is 20,000 times smaller than near Earth, as well as from fields generated by on-board components including the cADR, § 3.4.1). In addition, the cADR is delivered with its own magnetic shielding.

Redundant warm electronics boxes perform detector readout and instrument housekeeping using commercially available ASICs. The readout electronics compress the data before delivering it to the spacecraft. PICO detectors produce a total of 6.1 Tbits/day assuming 16 bits/sample, sampling rates from Table 3.1, and bolometer counts from Table 3.2. *Planck* HFI typically achieved $4.7 \times$ compression in flight with information loss increasing noise by $\sim 10\%$ [203, 204]. Suborbital work has demonstrated $6.2 \times$ lossless compression [202]. PICO assumes $4 \times$ lossless compression.

3.4 Thermal

Like the *Planck*-HFI instrument, PICO cools its focal plane to 0.1 K to enable detector operation (§ 3.4.1). To minimize detector noise due to instrument thermal radiation, the aperture stop and reflectors are cooled using both active and radiative cooling (§ 3.4.2, § 3.4.3, Fig. 3.3). All thermal requirements are met with robust margins (Table 3.3).

{sec:thermal}

3.4.1 cADR sub-kelvin cooling

A multi-stage continuous Adiabatic Demagnetization Refrigerator (cADR) cools the PICO focal plane to 0.1 K and the surrounding enclosure, filter, and readout components to 1 K. The cADR employs three refrigerant assemblies operating sequentially to absorb heat from the focal plane at 0.1 K and reject it to 1 K. Additionally, the cADR employs two assemblies operating sequentially to absorb this rejected heat at 1 K, cool other components to 1 K, and reject heat at 4.5 K. This configuration provides continuous cooling with small temperature variations at both the 0.1 K and 1 K. Heat straps connect the two cADR cold sinks to multiple points on the focal plane assembly, which has high thermal conductance paths built in, to provide spatial temperature uniformity and stability during operation. The detector arrays are thermally sunk to the mounting frame. Heat loads in the range of $20 \mu\text{W}$ at 0.1 K and 1mW at 1 K (time-average) are within the capabilities of current cADRs developed by GSFC [207, 208]. The PICO sub-kelvin loads are estimated at less than half of this capability.

{sec:cadr}

3.4.2 4 K Cooler

A cryocooler system similar to that used on JWST to cool the MIRI detectors [209, 210] removes the heat rejected from the cADR and cools the aperture stop and secondary reflector to 4.5 K. Both NGAS (which provided the MIRI coolers) and Ball Aerospace have developed such cool-

{sec:4kcooler}

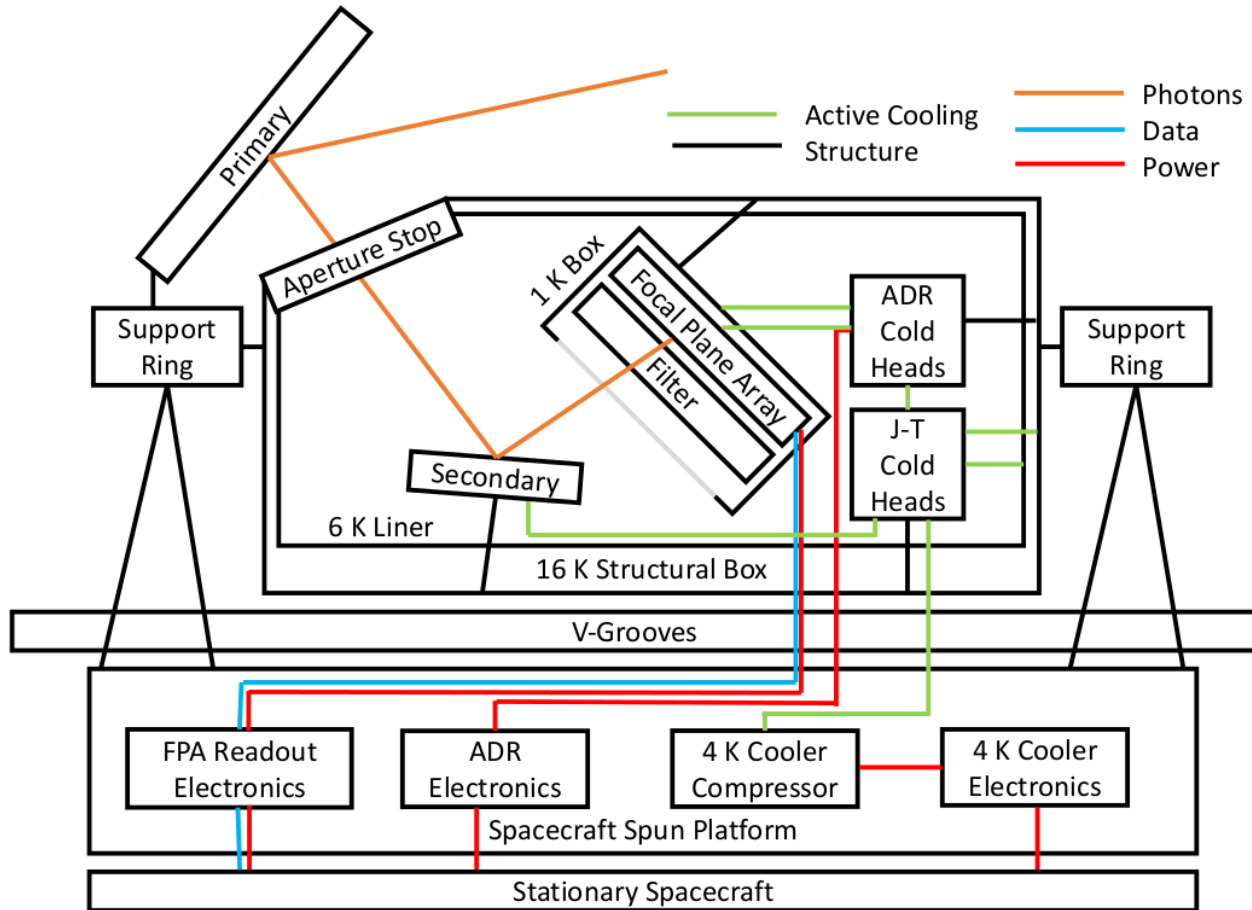


Figure 3.3: PICO instrument block diagram. Active coolers provide cooling to the 100 mK focal plane, the surrounding 1 K box, the 4.5 K secondary reflector, and the 4.5 K thermal liner that acts as a cold aperture stop. Data from the focal plane flows to (redundant, cross-strapped) warm readout electronics on the spun module of the spacecraft bus.
[fig:ArchitectureBlockDiagram](#)

Table 3.3: Projected cooler heat lift capabilities offer > 100 % heat lift margin, complying with community best practices [205]. The cADR lift capability at 1 K and 0.1 K is from a Goddard quote. Both NGAS and Ball project > 100 mW lift capability at 4.5 K using higher compression-ratio compressors currently in development (§ 3.4.2). The required loads were calculated using Thermal Desktop. Reference [206] was used to estimate the thermal conductive loads through mechanical supports. In addition to the listed components, the total 4.5 K heat load includes the intercept on the focal plane mechanical supports.^{tab:cooler}

Component	T Req'd	T CBE	Active heat lift		
			Req'd per model	Capability today	Projected capability
Primary reflector	< 40 K	17 K	N/A (radiatively cooled)		
Secondary reflector	< 8 K	4.5 K	42 mW total at 4.5 K	> 100 mW (§3.4.2, Figure 3.5)	
Aperture stop	4.5 K				
cADR heat rejection	4.5 K				
Focal plane enclosure and filter	1.0 K	1.0 K	0.36 mW	1.0 mW	
Focal plane	0.1 K	0.1 K	5.7 uW	16 uW	

ers under the NASA-sponsored Advanced Cryocooler Technology Development Program [211]. NGAS and Ball use slightly different but functionally-equivalent hardware approaches. A 3-stage precooler (acoustic Stirling by NGAS or mechanical Stirling by Ball) provides ~ 16 K precooling to a separate circulated-gas loop driven by a similar compressor modified for DC flow. The circulated-gas loop utilizes Joule–Thomson (J-T) expansion, further cooling the gas to 4.5 K. The entire precooler assembly and the J-T circulator compressor are located on the warm spacecraft, with relatively short tubing lengths conducting the gas flow from the precooling point to the J-T expansion point. All waste heat rejected by the cooler compressors and drive electronics is transferred to the spacecraft heat rejection system. Unlike JWST, the PICO cooler does not require deployment of the remote cold head.

The J-T expansion point is located close to the cADR heat rejection point, thereby providing the lowest temperature to the cADR. Subsequent to cooling the cADR, the gas flow intercepts conducted heat to the focal plane enclosure, then cools the aperture stop and the secondary reflector before returning in counterflow to the circulation compressor. Model-based projections indicate that the coolers delivered for MIRI could meet the PICO 4.5 K heat lift requirement with > 100 % margin with minimal changes: the replacement of the ⁴He gas used for MIRI with ³He, plus resizing of the gas counterflow heat exchangers to take advantage of the ³He properties.

It is highly likely that a better solution will be available before Phase A. NGAS and Ball are actively working on increasing the flow rate and compression ratio of the J-T compressor, which should result in significantly higher system efficiency, and in greater heat-lift margin above the PICO requirement. These improvements entail the implementation of well-known techniques (standard thermal engineering). The NGAS multi-stage J-T compressor has completed PDR-level development, and is expected to reach CDR level well before needed for PICO. Projected performance is shown in Figure 3.4. The Ball approach started with a larger compressor, required less modification to achieve comparable performance, and eliminated the cold bypass-precooling valve

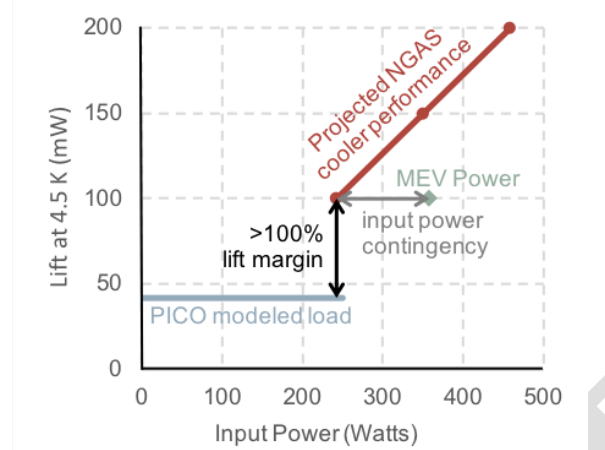


Figure 3.4: Projected performance of the NGAS cooler using a multi-stage compressor and ${}^4\text{He}$ [210] meets PICO’s requirements with $> 100\%$ margin. PICO conservatively carries additional input power contingency on the efficiency of the cooler.
fig:CoolerFigure

that was problematic for MIRI. The Ball approach uses ${}^3\text{He}$, while the NGAS approach uses ${}^4\text{He}$. Both employ re-optimized gas heat exchangers (trivial engineering changes).

3.4.3 Radiative cooling

A set of four V-groove radiators provides passive cooling. The outermost of the four V-groove shields shadows the interior shields from the Sun. The V-grooves radiate to space, each reaching successively cooler temperatures. The V-groove assembly is mechanically supported from the spacecraft bus by attachment to the low-conductance bipod struts that also carry the mechanical loads of the structural ring (Figure 3.1). The V-groove assembly provides a cold radiative environment to the primary reflector, structural ring, and telescope box, so radiative loads on those elements are smaller than the conductive loads through the mechanical support structures.

3.5 Instrument integration and test

PICO instrument I&T planning benefits greatly from heritage experience with the *Planck* HFI instrument [212].

PICO screens detector wafer performance prior to selection of flight wafers and focal plane integration. The cADR and 4 K cryocooler are qualified prior to delivery. The relative alignment of the two reflectors under thermal contraction is photogrammetrically verified in a thermal vacuum (TVAC) chamber.

PICO integrates the flight focal plane assembly and flight cADR in a dedicated sub-kelvin cryogenic testbed. Noise, responsivity, and focal-plane temperature stability are characterized using a representative optical load for each frequency band (temperature-controlled blackbody). Polarimetric and spectroscopic calibration are performed.

The focal plane is integrated with the reflectors and structures, and alignment verified photogrammetrically at cold temperatures in a TVAC chamber. The completely integrated observatory (instrument and spacecraft bus) is tested in TVAC to measure parasitic optical loading from the instrument, noise, microphonics, and radio-frequency interference (RFI). The observatory is 4.5 m in diameter and 6.1 m tall, with no deployables.

Table 4.1: PICO carries margin on key mission parameters. Maximum Expected Value (MEV) includes contingency.

Orbit type	Sun-Earth L2 Quasi-Halo
Mission class	Class B
Mission duration	5 years
Propellant (hydrazine)	213 kg (77% tank fill)
Launch mass (MEV)	2147 kg (3195 kg capability)
Max power (MEV)	1320 W (XX% of available area)
Onboard data storage	4.6 Tb (3 days of compressed data, enabling retransmission)
Survey implementation	Instrument on spin table
Attitude control	Zero-momentum 3-axis stabilized

{tab:mission_params}

4 Design reference mission

The PICO design reference mission is summarized in Table 4.1.

4.1 Concept of operations

The PICO concept of operations is similar to that of the successful *WMAP* [213] and *Planck* [214] missions. After launch, PICO cruises to a quasi-halo orbit around the Earth–Sun L2 Lagrange point (§ 4.1.1). A two-week decontamination period is followed by instrument cooldown, lasting about two months. After in-orbit checkout is complete, PICO begins the science survey.

PICO has a single science observing mode, surveying the sky continuously for 5 years using a pre-planned repetitive survey pattern (§ 4.1.2). Instrument data are compressed and stored onboard, then returned to Earth in daily 4-hr Ka-band science downlink passes (concurrent with science observations). Because PICO is observing relatively static Galactic, extragalactic, and cosmological targets, there are no requirements for time-critical observations or data latency. Presently, there are no plans for targets of opportunity or guest observer programs during the prime mission. The PICO instrument does not require cryogenic consumables (as the *Planck* mission did), permitting consideration of significant mission extension beyond the prime mission.

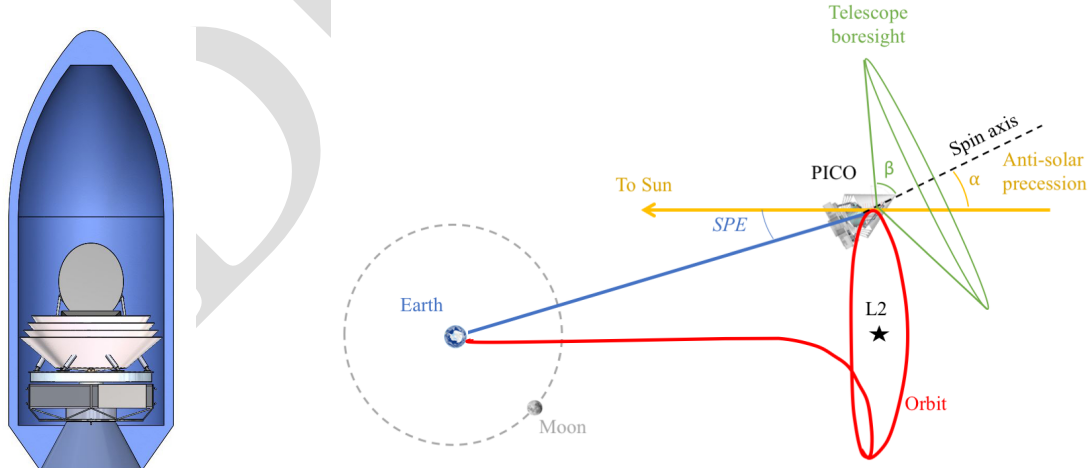


Figure 4.1: PICO is compatible with the Falcon 9.
fig:InFaifing

Figure 4.2: PICO surveys by continuously spinning the instrument about a precessing axis.
fig:MissionDesignFigure

4.1.1 Mission design and launch

PICO performs its science survey from a quasi-halo orbit around the Earth–Sun L2 Lagrange point. Predecessor missions *Planck* and *WMAP* both operated in L2 orbits.

L2 orbits provide favorable survey geometry (relative to Earth orbits) by mitigating viewing restrictions imposed by terrestrial and lunar stray light. The PICO orbit around L2 is small enough to ensure than the Sun–Probe–Earth (SPE) angle is less than 15° . This maintains the telescope boresight $> 70^\circ$ away from the Earth (Figure 4.2, $70^\circ = 180^\circ - \alpha - \beta - \text{SPE}$).

High data rate downlink to the Deep Space Network (DSN) is available from L2 using near-Earth Ka bands. L2 provides a stable thermal environment, simplifying thermal control. The PICO orbit exhibits no post-launch eclipses.

NASA requires that Probes be compatible with an Evolved Expendable Launch Vehicle (EELV). For the purpose of this study, the Falcon 9 [215] is used as the reference vehicle. Figure 4.1 shows PICO configured for launch in a Falcon 9 fairing. The Falcon 9 launch capability for ocean recovery exceeds PICO’s total launch mass (including contingency) by a $\sim 50\%$ margin.

Insertion to the halo manifold and associated trajectory correction maneuvers (TCMs) require 150 m s^{-1} of total ΔV by the spacecraft. The orbital period is ~ 6 months. Orbit maintenance requires minimal propellant (statistical $\Delta V \sim 2 \text{ m s}^{-1} \text{ year}^{-1}$). There are no disposal requirements for L2 orbits, but spacecraft are customarily decommissioned to heliocentric orbit.

4.1.2 Survey design

PICO employs a highly repetitive scan strategy to map the full sky. During the survey, PICO spins with a period $T_{\text{spin}} = 1 \text{ min}$ about a spin axis oriented $\alpha = 26^\circ$ from the anti-solar direction (Figure 4.2). This spin axis is forced to precess about the anti-solar direction with a period $T_{\text{prec}} = 10 \text{ hr}$. The telescope boresight is oriented at an angle $\beta = 69^\circ$ away from the spin axis. This β angle is chosen such that $\alpha + \beta > 90^\circ$, enabling mapping of all ecliptic latitudes. The precession axis tracks with the Earth in its yearly orbit around the Sun, so this scan strategy maps the full sky (all ecliptic longitudes) within 6 months.

PICO’s $\alpha = 26^\circ$ is chosen to be substantially larger than the *Planck* mission’s α angle (7.5°) to mitigate systematic effects by scanning across each sky pixel with a greater diversity of orientations [216]. Increasing α further would decrease the sun-shadowed volume available for the optics and consequently reduce the telescope aperture size. A deployable sun shade was considered but found not to be required, and was thus excluded in favor of a more conservative and less costly approach.

The instrument spin rate, selected through a trade study, matches that of the *Planck* mission. The study balanced low-frequency ($1/f$) noise subtraction (improves with spin rate) against implementation cost and heritage, pointing reconstruction ability (anti-correlated with spin rate), and data volume (linearly correlated with spin rate). The CMB dipole appears in the PICO data timestream at the spin frequency ($1 \text{ rpm} = 16.7 \text{ mHz}$). Higher multipole signals appear at harmonics of the spin frequency starting at 33 mHz , above the knee in the detector low-frequency noise (§ 3.2.3). A destriping mapmaker applied in data post-processing effectively operates as a high-pass filter, as demonstrated by *Planck* [217] (see § ??). PICO’s spin axis precession frequency is $> 400\times$ faster than that of *Planck*, greatly reducing the effects of any residual $1/f$ noise by spreading the effects more isotropically across pixels.

{sec:mission_desig}

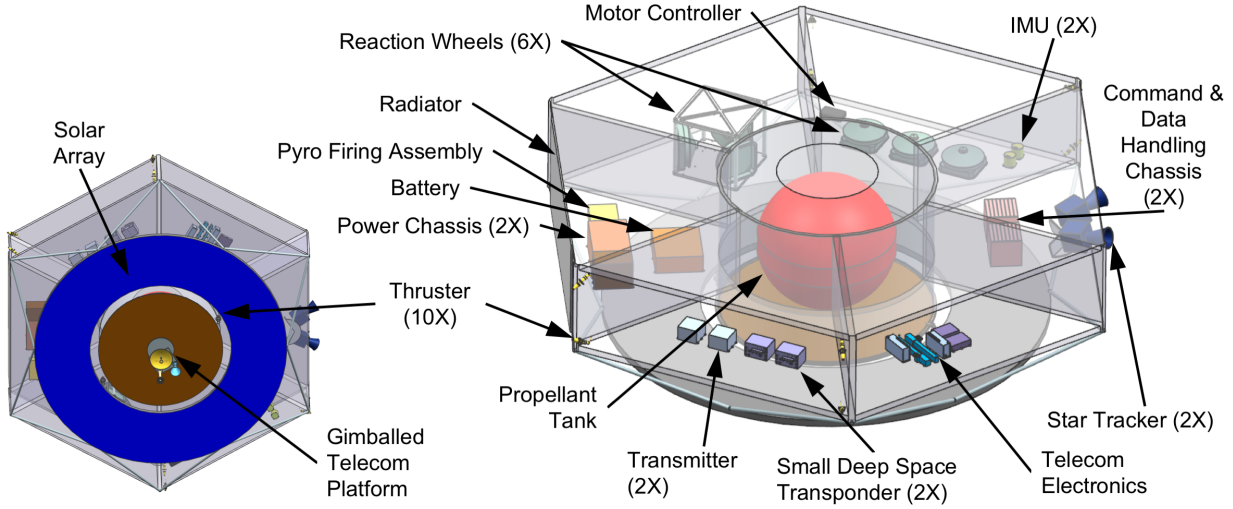


Figure 4.3: Modular equipment bays provide easy access to all components in the spacecraft de-spun module and enable parallel integration of spacecraft subsystems.
fig:Spacecraft

4.2 Ground segment

The PICO Mission Operations System (MOS) and Ground Data System (GDS) can be built with extensive reuse of standard tools. The PICO concept of operations is described in § 4.1. All space-ground communications, ranging, and tracking are performed by the Deep Space Network (DSN) 34 m Beam Wave Guide (BWG). X-band is used to transmit spacecraft commanding, return engineering data, and provide navigation information (S-band is a viable alternative, and could be considered in a future trade). Ka-band is used for high-rate return of science data. The baseline 150 Mb/s transfer rate (130 Mb/s information rate after CCSDS encoding) is an existing DSN catalog service [218]. The instrument produces 6.1 Tb/day, which is compressed to 1.5 Tb/day (§ 3.3). Daily 4 hr DSN passes return PICO data in 3.1 hr, with the remaining 0.9 hr available as needed for retransmission or missed-pass recovery.

4.3 Spacecraft

The PICO spacecraft bus is Class B and designed for a minimum lifetime of 5 years in the L2 environment. Mission critical elements are redundant. Flight spares, engineering models and prototypes appropriate to Class B are budgeted.

The aft end of the spacecraft (the “de-spun module”) is comprised of six equipment bays that house standard components (Figure 4.3). The instrument and V-grooves are mounted on bipods from the spacecraft “spun module,” which contains hosted instrument elements (Figure 3.1). A motor drives the spun module at 1 rpm to support the science survey requirements (§ 4.1.2). Reaction wheels on the despun module cancel the angular momentum of the spun module and provide three-axis control (§ 4.3.1).

The bipods that mechanically support the instrument are thermally insulating. The passively radiating V-groove assembly thermally isolates the instrument from solar radiation and from the bus (§ 3.4.3). Like *Planck* [214], the V-grooves are manufactured using honeycomb material. Additional radiators on the spun and despun spacecraft modules ($\sim 1 \text{ m}^2$ each) reject heat dissipated by spacecraft subsystems and hosted instrument elements.

PICO's avionics are dual-string with standard interfaces. Solid state recorders provide three days of science data storage (4.6 Tbit), enabling retransmission of missed data.

PICO employs a fully redundant Ka- and X-band telecommunications architecture. The Ka-band system uses a 0.3 m high-gain antenna to support a science data downlink information rate of 130 Mb/s to a 34 m BWG DSN ground station with a link margin of 4.8 dB. The X-band system provides command and engineering telemetry communication through all mission phases using medium and low gain antennas. Amplifiers, switches, and all three antennas are on a gimballed platform, enabling Ka and X-band downlink concurrent with science observations.

A 74 A-hr Li-ion battery is sized for a 3 hr launch phase with 44 % depth of discharge. Solar cells on the aft side of the bus provide positive power (with contingency) for all mission power modes after the launch phase (5.8 m^2 array, $\alpha = 26^\circ$ off-Sun). The driving mode is telecom concurrent with science survey (1320 W including 43 % contingency). Unused area in the solar array plane affords significant margin for growth (Figure 4.3). The heritage power electronics are dual-string.

The propulsion design is a simple mono-propellant blow-down hydrazine system with standard redundancy. Two aft-pointed 22 N thrusters provide ΔV and attitude control for orbit insertion and maintenance (§ 4.1.1), requiring 140 kg of propellant. Eight 4 N thrusters provide reaction wheel momentum management and backup attitude control authority (60 kg of propellant). Accounting for ullage (14 kg), the baseline propellant tank fill fraction is 77 %.

4.3.1 Attitude determination and control

PICO uses a zero net angular momentum control architecture with heritage from the SMAP mission (§ 6.3). PICO's instrument spin rate (1 rpm) matches that of the *Planck* mission, but the precession of the spin axis is much faster (10 hr vs 6 months), and the precession angle much larger (26° vs 7.5°). These differences make the spin-stabilized *Planck* control architecture impractical because of the amount of torque required to drive precession.

The PICO 1 rpm instrument spin rate is achieved and maintained using a spin motor. The spin motor drive electronics provide the coarse spin rate knowledge used for controlling the spin rate to meet the ± 0.1 rpm requirement.

Three reaction wheel assemblies (RWAs) are mounted parallel to the instrument spin axis and spin opposite to the instrument to achieve zero net angular momentum and keep the despun module three-axis stabilized. The spin axis is precessed using three RWAs mounted normal to the spin axis in a triangle configuration. Each set of three RWAs is sized such that two could perform the required function, providing single fault tolerance.

Spin axis pointing and spin rate knowledge are achieved and maintained using star tracker and inertial measurement unit (IMU) data. The attitude determination system is single-fault tolerant, with two IMUs each on the spun and despun modules, and two star trackers each on the spun and despun modules. Two sun sensors on the despun module are used for safe-mode contingencies and instrument Sun avoidance. All attitude control and reconstruction requirements are met, including spin axis control < 60 arcmin with < 1 arcmin/min stability, and reconstructed pointing knowledge < 10 arcsec (each axis, 3σ).

{ sec:attitude_deter }



Figure 5.1: SPT-3G operates a focal plane of three-color antenna-coupled pixels with $> 16,000$ total bolometers.
fig:spt_fp

5 Technology maturation

PICO builds off of the heritage of the *Planck* HFI instrument. Since *Planck*, suborbital experiments have used monolithically fabricated TES bolometers and multiplexing schemes to field instruments with thousands of detectors per camera (Fig. 5.1).

The remaining technology developments required to enable the PICO baseline design are:

1. Extension of three-color antenna-coupled bolometers down to 21 GHz and up to 462 GHz (§ 5.1).
2. Construction of high-frequency direct absorbing arrays and laboratory testing (§ 5.2).
3. Beam line and 100 mK testing to simulate the cosmic ray environment at L2 (§ 5.3).
4. Expansion of time-division multiplexing to support 128 switched rows per readout column (§ 5.4).
5. Simulation software (§ 5.5). **Shall to fill this in.**

We recommend APRA and SAT support to complete development of these technologies through the milestones described in Table 5.1.

5.1 Three-color antenna-coupled bolometers

Suborbital teams have successfully demonstrated a variety of optical coupling schemes, including horns with ortho-mode transducers (OMTs), lithographed antenna arrays, and sinuous antennas under lenslets (Figure 5.2). All have achieved background-limited performance in suborbital instruments with sufficient margin on design parameters to achieve this performance in the more demanding low background at L2. Experiments have covered many of PICO’s observing bands between 27 GHz and 270 GHz (Table 5.2). SPT-3G has used the PICO-baselined three-color pixel design to deploy 16,260 detectors covering 90–150–220 GHz. Other experiments have successfully deployed two-color pixels. All of these detector arrays have been packaged into modules and focal plane units in working cameras representative of the PICO integration.

To date, suborbital experiments have achieved statistical map depths of $3 \mu\text{K}_{\text{CMB}}$ arcmin on degree-scaled modes over small parts of the sky, within an order of magnitude of what PICO achieves over the entire sky (Table 3.2), and have demonstrated systematic control better than this level through full-pipeline simulations and null-test analysis (jackknife tests).

The baseline PICO instrument requires three-color dual-polarized antenna-coupled bolometers

{sec:technology_m}

{sec:bolometers}

Table 5.1: PICO technologies can be developed to TRL 5 prior to a 2023 Phase A start using the APRA and SAT programs.]

	Task	Current status	Milestone A	Milestone B	Milestone C	Current funding	Required Funding	TRL5 achieved
1a.	Three-color arrays $v < 90 \text{ GHz}$	2-color lab demos $v > 30 \text{ GHz}$	Field demo of 30–40 GHz (2020)	Lab demos 20–90 GHz (2022)	–	APRA & SAT funds	\$2.5M over 4 yr (1 APRA + 1 SAT)	2022
1b	Three-color arrays $v > 220 \text{ GHz}$	2-color lab demos $v < 300 \text{ GHz}$	Field demo of 150–270 GHz (2021)	–	APRA & SAT funds	\$3.5M over 4 yr (2 SATs)	2022	
2.	Direct absorbing arrays $v > 50 \text{ GHz}$	0.1–5 THz unpolarized	Design & prototype of arrays (2021)	Lab demo of 555 GHz (2022)	Lab demo 799 GHz (2023)	None	\$2M over 5 yr (1 SAT)	2023
3.	Cosmic ray studies	250 mK w/ sources	100 mK tests with sources (2021)	Beamline tests (2023)	–	APRA & SAT funds	\$0.5–1M over 5 yr (part of 1 SAT)	NA
4a.	Fast readout electronics	MUX66 demo	Engineering and Fab of electronics (2020)	Lab demo (2021)	Field demo (2023)	No direct funds	\$2.5M over 5 yr (1 SAT)	2023
4b.	System engineering; 128x MUX demo	MUX66 demo	Design of cables (2020)	Lab demo (2021)	Field demo (2023)	No direct funds		
5.	Simulation							

covering bands from 21 to 462 GHz and single-color dual-polarized direct-absorbing bolometers from 555 to 799 GHz (§ 3.2.1). The extension to lower frequencies requires larger antennas and therefore control of film properties and lithography over larger areas. Scaling to higher frequencies forces tighter critical dimensions and materials tend to exhibit higher losses. These challenges require tight control of cleanliness and full understanding of process parameters. All developments require careful characterization of beam properties and studies of associated systematic challenges for PICO.

The sinuous antenna has the bandwidth to service three colors per pixel, whereas horns and antenna arrays have only been used for two, so some version of the sinuous antenna will likely be needed to realize three-color pixels. However, the sinuous antenna couples to states that “wobble” log-periodically with frequency. There are potential solutions to this in the focal plane design, analysis, and free parameters of the antenna geometry. These will need to be explored subject to the uniformity and packing density constraints present at the extreme spectral bands. Systematics studies for field demonstrations will be particularly important. The PICO concept is robust to any challenges in developing three-color pixels; § 5.6 describes an option to descope to two-color pixels.

5.2 High-frequency direct absorbing arrays

The baseline PICO instrument requires single-color dual-polarized direct-absorbing bolometers from 555 to 799 GHz (§ 3.2.2).

Ground and balloon experiments have deployed focal planes with hundreds of horn-coupled spiderweb bolometers. SPT-Pol deployed dual-polarized versions of direct absorber horn-coupled bolometers. *Planck* used this style of bolometer, but with NTD-Ge thermistors instead of TESs (Fig. 5.3). Filled arrays of detectors such as Backshort Under Ground (BUG) bolometers are also

{ sec:dev_arrays }

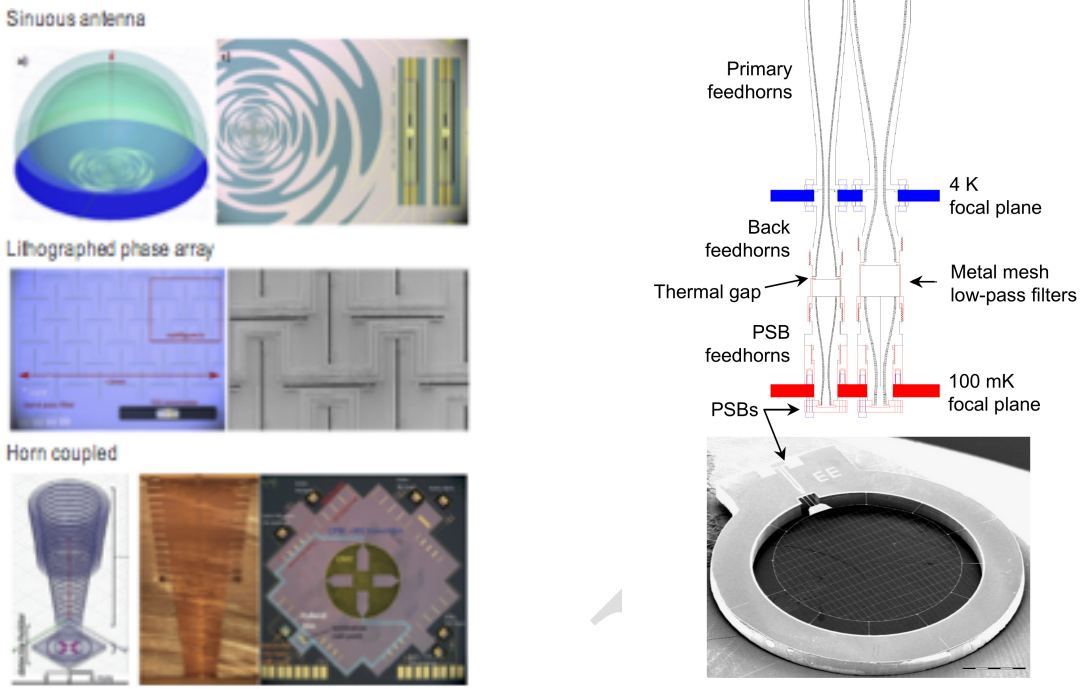


Figure 5.2: Multiple demonstrated optical coupling schemes are available to PICO. Images from CMB-S4 and coupling horns used in *Planck* for 143–343 GHz bands.
fig:OpticalCoupling fig:DirectAbsorbing

an option for these channels. The status of these efforts is summarized in Table 5.1.

Planck demonstrated the architecture of horns coupled to direct absorbing bolometers. For PICO’s high frequency detectors, this only needs to be generalized to dual polarized arrays. The greatest remaining challenge is the low-risk development of a packaging design. Such prototyping could culminate in a field demonstration, best performed in a balloon.

5.3 Environmental testing

Laboratory tests and in-flight data from balloons suggest that these TES bolometers are more naturally robust against cosmic rays than the individual NTD-Ge bolometers used in *Planck*. Cosmic ray glitches have fast recovery times and low coincidence rates [219].

So far, cosmic ray tests and in-flight analysis of TES bolometers are encouraging [219]. The CMB community can retire residual risk with 100 mK testing where the array heat sinking may be weaker, and beam-line tests to help control for background glitch rates.

5.4 Multiplexing

More than ten experiments have used TDM readout. SCUBA2 on JCMT has 10,000 pixels, nearly as many detectors as planned for PICO [221]. Most of these experiments have used 32-row multiplexing. Recently ACT has expanded this to 64-row multiplexing [200].

PICO’s sensitivity requirements dictate the use of $\sim 13,000$ transition edge sensor bolometers, requiring a highly multiplexed system. The PICO baseline design calls for time-division multiplexing with 128 switched rows per readout column (TDM-128 \times), which exceeds that of Advanced ACTPol’s recently demonstrated TDM-66 \times [200]. The leap to TDM-128 \times requires:

{sec:env_testing}

{sec:multiplexing}

Table 5.2: Multiple active suborbital efforts are advancing technologies relevant to PICO.^{tab:suborbital}

Project	Type	Polarized	Mono-lithic?	v_c [GHz]	Colors per pixel	N_{bolo}	Significance	Reference
PICO low frequency	Probe	Yes	Yes	21 – 462	Three	11,796		§ 3.2.1
SPT-3G	Ground	Yes	Yes	90 – 220	Three	16,260	Trichroic	[222]
Advanced ACT-pol	Ground	Yes	Yes	27 – 230	Two	3,072	Dichroic	[223]
BICEP/Keck	Ground	Yes	Yes	90 – 270	One	5,120	50 nK-deg	[224]
Berkeley, Caltech, NIST	Lab	Yes	Yes	30 – 270	Two	–	Band coverage	[201, 225, 226]
SPIDER	Balloon	Yes	Yes	90 – 150	One	2,400	Stable to 10 mHz	[199]
PICO high frequency	Probe	Yes	Yes	555 – 799	One	1,200		§ 3.2.2
Planck HFI	Flight	Yes*	No	143 – 857	One	48	TRL 9 absorbing bolometers	[197]
SPT-SZ	Ground	No	Yes	90 – 220	One	840	Monolithic array TESS	[195]
SPT-pol-90	Ground	Yes	No	90	One	180	Dual pol absorbing TESs	[227]

* 143–343 GHz only

- development of fast-switched room temperature electronics; and
- system engineering of room temperature to cryogenic row select cabling to ensure sufficiently fast row switch settling times.

The system engineering study should culminate in a demonstration of TDM-128× SQUID aliased noise below PICO detector sensitivity requirements.

5.5 Simulation

Shaul to write/delegate this section.

{sec:simulation}

5.6 Technology descopes

A descope from three-color to two-color pixels remains a viable alternative should the three-color technology not mature as planned. Descope studies suggest that a PICO-size focal plane using two-color pixels at the lower frequencies and the baseline one-color pixels at the higher frequencies would contain 8,840 detectors (compared to the baseline 12,966) and map in 19 colors (baseline 21). Because horns have a 2.3 : 1 bandwidth, each of the two bands in a pixel has 35 % bandwidth (compared to the baseline 25 %), which compensates for pixel count, resulting in $0.61 \mu\text{K}_{\text{CMB}}$ arcmin aggregate CBE map depth, which matches the PICO CBE map depth, and affords > 40 % margin against the $0.87 \mu\text{K}_{\text{CMB}}$ arcmin baseline requirement (Table 3.2), but with coarser spectral resolution.

5.7 Enhancing technologies

The following technologies are neither required nor assumed by the PICO baseline concept. They represent opportunities to extend scientific capabilities or simplify engineering.

PICO baselines TDM readout because of its relative maturity and demonstrated sensitivity and stability in relevant science missions. Lab tests of Frequency Domain Multiplexing (FDM) suggest comparable performance with higher multiplexing factors and lower loads on cryogenic stages relative to TDM. Suborbital experiments such as SPT-3G have used frequency division multiplexing (FDM) to readout focal planes comparable in size to PICO.

Microwave frequency SQUID multiplexing can increase the multiplexing density and reduce the number of lines between the 4K and ambient temperature stages [228, 229]. Kinetic Induc-

tance Detectors (KIDs) and Thermal KIDs (TKIDs) can further reduce the wire count, obviate the SQUIDs, and dramatically simplify integration by performing multiplexing on the same substrate as the detectors themselves [230, 231]. The cost to develop these technologies is \$3–4M/year, with a high chance of reaching TRL-5 before Phase A.

DRAFT

6 Project management, heritage, risk, and cost

6.1 PICO Study Participants

The PICO study was open to the entire mm/sub-mm science community and included more than 150 scientists. Seven working groups were led by members of PICO's Executive Committee, which met weekly under the leadership of PI Shaul Hanany. More than 60 people participated in-person in two community workshops (November 2017 and May 2018).

The PICO engineering concept definition package was generated by Team X (the JPL concurrent design lab). The Team X study was supported by inputs from a JPL engineering team and Lockheed Martin.

The full list of study report contributors and endorsers follows the cover page.

6.2 Project management plan

PICO benefits from the experience of predecessor missions such as *Planck* and *WMAP*, as well as many years of investment in technology development and a multitude of suborbital experiments. In addition to demonstrated science and engineering capabilities, this heritage has developed a community of people with the expertise required to field a successful mission.

This study assumes mission management by JPL with a Principal Investigator leading a single science team. A Project Manager provides project oversight for schedule, budget, and deliverables. A Project Systems Engineer leads systems engineering activities and serves as the Engineering Technical Authority. A Mission Assurance Manager serves as the Independent Technical Authority. The PICO mission development schedule is shown in Figure 6.1.

	FY24	FY25	FY26	FY27	FY28	FY29	FY30	FY31	FY32	FY33	FY34	FY35
CY 2023	CY 2024	CY 2025	CY 2026	CY 2027	CY 2028	CY 2029	CY 30	CY 31	CY 32	CY 33	CY 34	
PH A (12 mths)	PH B (12 mths)	PHASE C (22 mths)	PHASE D(18 mths)	PHASE E (5 yrs)		F 4 mths						
◆ 10/23 KDP-A	◆ 10/24 KDP-B	◆10/25 KDP-C	◆ 8/27 KDP-D	◆ 2/29 PLAR (Start of Ph E)	KDP-F 2/34 ◆							
Reviews	10/25 PDR ◆		◆ 7/26 CDR	◆ 7/27 ARR	Launch 1/29★							

Figure 6.1: The PICO baseline schedule is based on historical actuals from similarly-sized missions such as Juno and SMAP. Per NASA direction, Probe studies assume a Phase A start in October 2023.
[fig:Schedule](#)

Probes are medium-class missions, similar in cost scope to NASA's New Frontiers missions, which are Category 1 and Risk Classification A or B, with Phase A–D costs capped at $\sim \$850M$ (not including the launch vehicle). JPL is well-prepared to manage Probe missions, having managed the Juno New Frontiers mission (launched 2011) and also the development of the medium-class *Spitzer* Space Telescope (launched 2003). JPL delivered the bolometric detectors for the *Planck* HFI instrument (launched 2009). Presently, JPL is managing NEOCam, a Discovery class infrared space telescope.

The PICO spacecraft provider will be selected during mission formulation. Multiple organizations are capable of providing a spacecraft bus to meet PICO's requirements. Lockheed Martin contributed to the PICO concept study, leveraging their experience with New Frontiers missions Juno and OSIRIS-REx.

6.3 Heritage

The successful *Planck* mission provides science heritage for PICO. Technical heritage traces to multiple missions.

Because PICO observes in the mm/sub-mm regime, the surface accuracy requirement for the reflectors is relatively easy to meet. PICO's reflectors are similar to *Planck*'s, but somewhat larger (270 cm × 205 cm primary vs. 189 cm × 155 cm) [232]. *Herschel* observed at wavelengths more demanding than PICO's and was larger (350 cm diameter primary) [233].

The heritage of the PICO detectors and readout electronics (§ 3.2, § 3.3) is described in § 5.

PICO's detectors are cooled by a cADR (3.4.1) with requirements that are within the capabilities of current ADRs developed by Goddard Space Flight Center. These systems have been applied to several JAXA missions, including *Hitomi* [208].

PICO's 4 K cryocooler (§ 3.4.2) is a direct extension of the JWST MIRI design [209, 210]. PICO benefits from a simpler and more reliable implementation of the J-T system than was required for MIRI, in that no deployment of cooling lines is required, and all flow valving is performed on the warm spacecraft. Cooling multiple independent points with a J-T loop has been demonstrated on *Planck* with the JPL-supplied 18 K cooler [234].

Structures similar to PICO's V-groove radiator assembly (§ 3.4.3) are a standard approach for passive cooling first described more than thirty years ago [235]. PICO has baselined a simple honeycomb material construction like that successfully flown by the *Planck* mission [234, 236].

Most requirements on the PICO spacecraft are well within typical ranges and can be met with standard high heritage systems (§ 4.3). PICO's spin architecture and data volume requirements are less typical, and discussed below.

The PICO zero-momentum control architecture (§ 4.3.1) has heritage from the SMAP mission's successful control architecture. PICO has a slower spin rate and less cancelled angular momentum than SMAP. SMAP requires 359 N m s to cancel the momentum of a 6 m instrument antenna spun at 14.6 rpm [237]. Based on mass properties derived from the PICO CAD model, PICO requires XXX N m s to cancel the momentum of the instrument and spacecraft spun module (XXX kg including contingency) at 1 rpm.

Though PICO's data volume is notable by current standards, it is already enveloped by missions in development. PICO produces 6.1 Tb/day of raw data which is compressed to 1.5 Tb/day (§ 3.3). PICO downlinks data daily, but baselines storage of 3 days of (compressed) data to mitigate missed telecom passes. This requires 4.5 Tb of onboard storage, in family with the 3.14 Tb solid state recorder currently in use by Landsat 8 and much smaller than the 12 Tb flash memory planned for NISAR [239]. The PICO baseline 150 Mb/s Ka-band data downlink is an existing DSN catalog service [218]. The baseline PICO mission generates ~ 2,200 Tb of raw (uncompressed) data per year, less than the ~ 6,800 Tb/year currently returned by Landsat 8 and ~ 9,300 Tb/yr planned by NISAR [239].

6.4 Risk assessment

6.4.1 Pre-mission risks

Technology development (§ 5) is performed prior to the beginning of mission development, and is outside of the mission cost (per NASA direction), so associated risks do not represent threats to the cost of mission development. Rather, these technology development risks affect the availability of the described baseline mission. A technology-related mission descope is described in § 5.6.

{sec:heritage}

{sec:risk_assessme}

{sec:premission_ri}

6.4.2 Development risks

PICO's healthy contingencies, margins, and reserves provide flexibility to address risks realized during mission development. PICO carries > 40% instrument sensitivity margin (Table 3.2), > 100% heat lift margin (Table 3.3), 43% system power contingency, 31% payload mass contingency, and 25% spacecraft mass contingency. The Falcon 9 launch capability (assuming ocean recovery) exceeds PICO's total launch mass (including contingency) by a ~ 50% margin. The PICO budget includes 30% cost reserves for Phases A–D (§ 6.5).

During mission development the Project Systems Engineer continually assesses risks, tracks progress toward retiring them, and updates mitigations. Mitigations for a few top risks identified during this study are described below.

- Thermal risk can be mitigated through extensive thermal modeling and review in Phase A, and design for early test verification.
- Risks associated with the instrument spin architecture can be mitigated by engaging JPL engineers who were involved in the SMAP mission.
- Detector delivery schedule risk can be mitigated by beginning fabrication early in the project life cycle and fabricating a generous number of detector wafers to ensure adequate yield. Multiple institutions (including, for example, JPL, GSFC, NIST, and ANL) would be capable of producing the PICO detectors. Suborbital programs generally achieve > 66% detector wafer yield.
- Risks associated with the integration and test of a cryogenic instrument can be mitigated through advanced planning and allocation of appropriate schedule and schedule margin.

6.4.3 Operations risks

The PICO design meets the requirements associated with the NASA Class B risk classification. For Class B missions, essential spacecraft and instrument functions are typically fully redundant. This increases mission cost, but significantly reduces the risk of mission failure.

The PICO mission utilizes a single instrument with a single observing mode mapping the sky using a repetitive survey pattern. The mission does not require any time-critical activities. The observatory fits in to the launch vehicle fairing in its operational configuration, so no hardware deployments are required. Because PICO observes at long wavelengths, the telescope does not require a dust cover (nor the associated mission-critical cover release).

The spacecraft incorporates a fault protection system for anomaly detection and resolution. The Sun-pointed, command receptive, thermally stable safe-mode attitude allows ground intervention for fault resolution without time constraints. PICO's high degree of hardware redundancy and onboard fault protection ensure spacecraft safety in the event of unforeseen failures and faults.

Science data analysis, including foreground separation (§ 2.5) and systematics control (§ 2.6) are discussed in the science section (§ 2).

6.5 Mission cost

We estimate PICO's total Phase A–E lifecycle cost between \$870M and \$960M, including the \$150M allocation for the Launch Vehicle (per NASA direction). These cost estimates include 30% reserves for development (Phases A–D) and 13% reserves for operations (Phase E). Pre-Phase-A technology maturation (§ 5) will be accomplished through the normal APRA and SAT processes, and is not included in the mission cost (per NASA direction).

Table 6.1 shows the mission cost breakdown, including the JPL Team X cost estimate as well

{sec:development_risks}

{sec:operations_risks}

{sec:mission_cost}

Table 6.1: Detailed breakdown of Team X and PICO Team cost estimates (in FY18\$). Costs are based on the schedule in Fig. 6.1, which includes 5 years of operations.

Work Breakdown Structure (WBS) Elements	Team X	PICO Team
Development Cost (Phases A–D)	\$724M	\$634M–\$677M
1.0, 2.0, 3.0 Management, Systems Engineering, and Mission Assurance	\$54M	\$47M–\$50M
4.0 Science	\$19M	
5.0 Payload System	\$168M	
6.0 Flight System	\$248M	\$210M–\$240M
10.0 Assembly, Test, and Launch Operations (ATLO)	\$24M	
7.0 Mission Operations Preparation	\$16M	
9.0 Ground Data Systems	\$21M	
12.0 Mission and Navigation Design	\$7M	
Development Reserves (30%)	\$167M	\$146M–\$156M
Operations Cost (Phase E)	\$84M	
1.0 Management	\$6M	
4.0 Science	\$20M	
7.0 Mission Operations	\$34M	
9.0 Ground Data Systems	\$14M	
Operations Reserves (13%)	\$10M	
Launch Vehicle Cost	\$150M	
Total Cost	\$958M	\$868M–\$911M

as the PICO team cost estimate. Team X is JPL’s concurrent design facility. Team X estimates are generally model-based, and were generated after a series of instrument and mission-level studies. Their accuracy is commensurate with the level of understanding typical to Pre-Phase-A concept development. They do not constitute an implementation or cost commitment on the part of JPL or Caltech.

The PICO team has generally adopted the Team X estimates, but also obtained a parametrically estimated cost range for the Flight System (WBS 6) and Assembly, Test and Launch Operations (ATLO, WBS 7) from Lockheed Martin Corporation to represent the cost benefits that might be realized by working with an industry partner. After adding estimated JPL overhead and Team X estimated V-groove assembly costs (not included in the Lockheed estimate), the PICO team cost is in-family with but lower than the Team X cost (Table 6.1).

Management, Systems Engineering, and Mission Assurance (WBS 1–3) development costs scale linearly with the WBS 4–12 development costs in the Team X model, and are adjusted accordingly in the PICO team estimate.

Science team (WBS 4) costs are assessed by Team X based on PICO science team estimates of the numbers and types of contributors and meetings required for each year of PICO mission development and operations. These workforce estimates are informed by recent experience with the *Planck* mission.

Payload system (WBS 5) costs are discussed in detail in § 6.5.1. PICO’s spacecraft (WBS 6) cost reflects a robust Class B architecture (§ 4.3). Mission-critical elements are redundant. Ap-

{tab:cost}

Table 6.2: Detailed breakdown of PICO instrument costs.

Instrument Elements	Cost
Management, Systems Eng., Assurance	\$18M
4 K Cooler and 0.1 K cADR	\$71M
Focal plane and electronics	\$27M
Mechanical, Thermal, Software	\$17M
Telescope	\$6M
Instrument integration and test	\$29M
Total Instrument Cost	\$168M

ropriate flight spares, engineering models and prototypes are budgeted. The V-groove assembly (§ 3.4.3) is costed in WBS 6. Mission operations (WBS 7), Ground Data Systems (WBS 9), and Mission Navigation and Design (WBS 12) costs reflect a relatively simple concept of operations (§ 4.1). PICO has a single instrument with a single science observing mode, surveying the sky continuously using a pre-planned repetitive survey pattern. Orbit maintenance activities are simple and infrequent.

6.5.1 Instrument cost

The PICO payload consists of a single instrument: an imaging polarimeter. Instrument costs are tabulated in Table 6.2.

The superconducting detectors require sub-kelvin cooling to operate. The active cooling system (the 0.1 K cADR and 4 K cryocooler, § 3.4.1 and § 3.4.2) comprises nearly half of the instrument cost. The cADR cost for this study is an estimate from NASA Goddard Space Flight Center (GSFC), and assumes the provision of both a flight model and an engineering model. GSFC has produced ADRs for multiple spaceflight missions. The 4 K cryocooler cost for this study is based on the NASA Instrument Cost Model (NICM) VIII CER Cryocooler model [240], assuming a commercial build. PICO benefits greatly from recent and ongoing investment by commercial suppliers of 4 K coolers (as described in § 3.4.2). Team X used NICM VIII to model the cost of the focal plane and dual string readout electronics (§ 3.2, § 3.3). Team X estimated the telescope cost using the Stahl model [241]. The telescope is not a major cost driver, primarily because the reflector only needs to be diffraction limited at 330 μm (900 GHz) (§ 3.1).

Based on JPL experience, 18 % of the instrument cost is allocated for integration and test. This includes integration and test of the flight focal-plane assembly with the flight cADR and then integration and test of the complete instrument including the focal-plane assembly, reflectors, structures, and coolers (§ 3.5). Integration and test of the instrument with the spacecraft is costed in WBS 10 (ATLO).

References

- [1] C. for a Decadal Survey of Astronomy and Astrophysics, *New Worlds, New Horizons in Astronomy and Astrophysics*. National Academy Press, 2010.
- [2] K. Array, BICEP2 Collaborations, : *et al.*, “BICEP2 / Keck Array x: Constraints on Primordial Gravitational Waves using Planck, WMAP, and New BICEP2/Keck Observations through the 2015 Season,” *ArXiv e-prints*, Oct. 2018.
- [3] Planck Collaboration, R. Adam, P. A. R. Ade *et al.*, “Planck intermediate results. XXX. The angular power spectrum of polarized dust emission at intermediate and high Galactic latitudes,” *Astron. Astrophys.*, vol. 586, p. A133, Feb. 2016.
- [4] U. Seljak and M. Zaldarriaga, “Signature of gravity waves in polarization of the microwave background,” *Phys. Rev. Lett.*, vol. 78, pp. 2054–2057, 1997.
- [5] M. Kamionkowski, A. Kosowsky, and A. Stebbins, “A Probe of primordial gravity waves and vorticity,” *Phys. Rev. Lett.*, vol. 78, pp. 2058–2061, 1997.
- [6] A. H. Guth, “The Inflationary Universe: A Possible Solution to the Horizon and Flatness Problems,” *Phys. Rev.*, vol. D23, pp. 347–356, 1981, [Adv. Ser. Astrophys. Cosmol.3,139(1987)].
- [7] A. D. Linde, “A New Inflationary Universe Scenario: A Possible Solution of the Horizon, Flatness, Homogeneity, Isotropy and Primordial Monopole Problems,” *Phys. Lett.*, vol. 108B, pp. 389–393, 1982, [Adv. Ser. Astrophys. Cosmol.3,149(1987)].
- [8] A. Albrecht and P. J. Steinhardt, “Cosmology for Grand Unified Theories with Radiatively Induced Symmetry Breaking,” *Phys. Rev. Lett.*, vol. 48, pp. 1220–1223, 1982, [Adv. Ser. Astrophys. Cosmol.3,158(1987)].
- [9] A. A. Starobinsky, “A New Type of Isotropic Cosmological Models Without Singularity,” *Phys. Lett.*, vol. B91, pp. 99–102, 1980, [,771(1980)].
- [10] V. F. Mukhanov and G. V. Chibisov, “Quantum Fluctuations and a Nonsingular Universe,” *JETP Lett.*, vol. 33, pp. 532–535, 1981, [Pisma Zh. Eksp. Teor. Fiz.33,549(1981)].
- [11] A. H. Guth and S. Y. Pi, “Fluctuations in the New Inflationary Universe,” *Phys. Rev. Lett.*, vol. 49, pp. 1110–1113, 1982.
- [12] S. W. Hawking, “The Development of Irregularities in a Single Bubble Inflationary Universe,” *Phys. Lett.*, vol. 115B, p. 295, 1982.
- [13] A. A. Starobinsky, “Dynamics of Phase Transition in the New Inflationary Universe Scenario and Generation of Perturbations,” *Phys. Lett.*, vol. 117B, pp. 175–178, 1982.
- [14] J. M. Bardeen, P. J. Steinhardt, and M. S. Turner, “Spontaneous Creation of Almost Scale - Free Density Perturbations in an Inflationary Universe,” *Phys. Rev.*, vol. D28, p. 679, 1983.
- [15] A. A. Starobinsky, “Spectrum of relict gravitational radiation and the early state of the universe,” *JETP Lett.*, vol. 30, pp. 682–685, 1979, [,767(1979)].
- [16] L. M. Krauss and F. Wilczek, “Using Cosmology to Establish the Quantization of Gravity,” *Phys. Rev.*, vol. D89, no. 4, p. 047501, 2014.
- [17] The Polarbear Collaboration: P. A. R. Ade, Y. Akiba, A. E. Anthony *et al.*, “A Measurement of the Cosmic Microwave Background B-mode Polarization Power Spectrum at Sub-degree Scales with POLARBEAR,” *Ap. J.*, vol. 794, p. 171, Oct. 2014.
- [18] R. Keisler, S. Hoover, N. Harrington *et al.*, “Measurements of Sub-degree B-mode Polarization in the Cosmic Microwave Background from 100 Square Degrees of SPTpol Data,” *Ap. J.*, vol. 807, p. 151, Jul. 2015.
- [19] T. Louis, E. Grace, M. Hasselfield *et al.*, “The Atacama Cosmology Telescope: two-season ACTPol spectra and parameters,” *JCAP*, vol. 6, p. 031, Jun. 2017.
- [20] P. A. R. Ade *et al.*, “Improved Constraints on Cosmology and Foregrounds from BICEP2 and Keck Array Cosmic Microwave Background Data with Inclusion of 95 GHz Band,” *Phys. Rev. Lett.*, vol. 116, p. 031302, 2016.
- [21] Planck Collaboration, Y. Akrami, F. Arroja *et al.*, “Planck 2018 results. I. Overview and the cosmological legacy of Planck,” *ArXiv e-prints*, Jul. 2018.
- [22] A. B. Goncharov and A. D. Linde, “Chaotic Inflation in Supergravity,” *Phys. Lett.*, vol. 139B, pp. 27–30, 1984.
- [23] U. Seljak and C. M. Hirata, “Gravitational lensing as a contaminant of the gravity wave signal in the CMB,” *Phys. Rev. D.*, vol. 69, no. 4, p. 043005, Feb. 2004.

- [24] K. M. Smith, D. Hanson, M. LoVerde, C. M. Hirata, and O. Zahn, “Delensing CMB polarization with external datasets,” *JCAP*, vol. 6, p. 014, Jun. 2012.
- [25] M. Alvarez, T. Baldauf, J. R. Bond *et al.*, “Testing Inflation with Large Scale Structure: Connecting Hopes with Reality,” *ArXiv e-prints*, Dec. 2014.
- [26] G. Steigman, “Cosmology confronts particle physics.” *Annual Review of Nuclear and Particle Science*, vol. 29, pp. 313–338, 1979.
- [27] M. Bolz, A. Brandenburg, and W. Buchmuller, “Thermal production of gravitinos,” *Nucl. Phys.*, vol. B606, pp. 518–544, 2001, [Erratum: *Nucl. Phys.*B790,336(2008)].
- [28] P. J. E. Peebles, S. Seager, and W. Hu, “Delayed recombination,” *Astrophys. J.*, vol. 539, pp. L1–L4, 2000.
- [29] X.-L. Chen and M. Kamionkowski, “Particle decays during the cosmic dark ages,” *Phys. Rev.*, vol. D70, p. 043502, 2004.
- [30] N. Padmanabhan and D. P. Finkbeiner, “Detecting dark matter annihilation with CMB polarization: Signatures and experimental prospects,” *Phys. Rev.*, vol. D72, p. 023508, 2005.
- [31] M. S. Madhavacheril, N. Sehgal, and T. R. Slatyer, “Current Dark Matter Annihilation Constraints from CMB and Low-Redshift Data,” *Phys. Rev.*, vol. D89, p. 103508, 2014.
- [32] D. Green, P. D. Meerburg, and J. Meyers, “Aspects of Dark Matter Annihilation in Cosmology,” *ArXiv e-prints*, Apr. 2018.
- [33] X. Chen, S. Hannestad, and R. J. Scherrer, “Cosmic microwave background and large scale structure limits on the interaction between dark matter and baryons,” *ArXiv Astrophysics e-prints*, Feb. 2002.
- [34] K. Sigurdson, M. Doran, A. Kurylov, R. R. Caldwell, and M. Kamionkowski, “Dark-matter electric and magnetic dipole moments,” *Phys. Rev. D.*, vol. 70, no. 8, p. 083501, Oct. 2004.
- [35] C. Dvorkin, K. Blum, and M. Kamionkowski, “Constraining Dark Matter-Baryon Scattering with Linear Cosmology,” *Phys. Rev.*, vol. D89, no. 2, p. 023519, 2014.
- [36] V. Gluscevic and K. K. Boddy, “Constraints on Scattering of keV-TeV Dark Matter with Protons in the Early Universe,” *Physical Review Letters*, vol. 121, no. 8, p. 081301, Aug. 2018.
- [37] K. K. Boddy and V. Gluscevic, “First Cosmological Constraint on the Effective Theory of Dark Matter-Proton Interactions,” *ArXiv e-prints*, Jan. 2018.
- [38] W. L. Xu, C. Dvorkin, and A. Chael, “Probing sub-GeV dark matter-baryon scattering with cosmological observables,” *Phys. Rev. D.*, vol. 97, no. 10, p. 103530, May 2018.
- [39] K. K. Boddy, V. Gluscevic, V. Poulin, E. D. Kovetz, M. Kamionkowski, and R. Barkana, “A Critical Assessment of CMB Limits on Dark Matter-Baryon Scattering: New Treatment of the Relative Bulk Velocity,” *ArXiv e-prints*, Jul. 2018.
- [40] T. R. Slatyer and C.-L. Wu, “Early-Universe constraints on dark matter-baryon scattering and their implications for a global 21 cm signal,” *Phys. Rev. D.*, vol. 98, no. 2, p. 023013, Jul. 2018.
- [41] J. D. Bowman, A. E. E. Rogers, R. A. Monsalve, T. J. Mozdzen, and N. Mahesh, “An absorption profile centred at 78 megahertz in the sky-averaged spectrum,” *Nature*, vol. 555, pp. 67–70, Mar. 2018.
- [42] Planck Collaboration, N. Aghanim, Y. Akrami *et al.*, “Planck 2018 results. VI. Cosmological parameters,” *ArXiv e-prints*, Jul. 2018.
- [43] Planck Collaboration, N. Aghanim, M. Ashdown *et al.*, “Planck intermediate results. XLVI. Reduction of large-scale systematic effects in HFI polarization maps and estimation of the reionization optical depth,” *ArXiv e-prints*, May 2016.
- [44] M. Kaplinghat, L. Knox, and Y.-S. Song, “Determining neutrino mass from the CMB alone,” *Phys. Rev. Lett.*, vol. 91, p. 241301, 2003.
- [45] M. Levi *et al.*, “The DESI Experiment, a whitepaper for Snowmass 2013,” *ArXiv e-prints*, 2013.
- [46] L. M. Widrow, “Origin of galactic and extragalactic magnetic fields,” *Rev. Mod. Phys.*, vol. 74, pp. 775–823, 2002.
- [47] L. M. Widrow, D. Ryu, D. R. G. Schleicher, K. Subramanian, C. G. Tsagas, and R. A. Treumann, “The First Magnetic Fields,” *Space Sci. Rev.*, vol. 166, pp. 37–70, 2012.
- [48] D. Grasso and H. R. Rubinstein, “Magnetic fields in the early universe,” *Phys. Rept.*, vol. 348, pp. 163–266, 2001.
- [49] T. Vachaspati, “Magnetic fields from cosmological phase transitions,” *Phys. Lett.*, vol. B265, pp. 258–261, 1991.

- [50] M. S. Turner and L. M. Widrow, “Inflation Produced, Large Scale Magnetic Fields,” *Phys. Rev.*, vol. D37, p. 2743, 1988.
- [51] B. Ratra, “Cosmological ‘seed’ magnetic field from inflation,” *Astrophys. J.*, vol. 391, pp. L1–L4, 1992.
- [52] A. Diaz-Gil, J. Garcia-Bellido, M. Garcia Perez, and A. Gonzalez-Arroyo, “Magnetic field production during preheating at the electroweak scale,” *Phys. Rev. Lett.*, vol. 100, p. 241301, 2008.
- [53] N. Barnaby, R. Namba, and M. Peloso, “Observable non-gaussianity from gauge field production in slow roll inflation, and a challenging connection with magnetogenesis,” *Phys. Rev.*, vol. D85, p. 123523, 2012.
- [54] A. J. Long, E. Sabancilar, and T. Vachaspati, “Leptogenesis and Primordial Magnetic Fields,” *JCAP*, vol. 1402, p. 036, 2014.
- [55] R. Durrer and A. Neronov, “Cosmological Magnetic Fields: Their Generation, Evolution and Observation,” *Astron. Astrophys. Rev.*, vol. 21, p. 62, 2013.
- [56] A. Zucca, Y. Li, and L. Pogosian, “Constraints on Primordial Magnetic Fields from Planck combined with the South Pole Telescope CMB B-mode polarization measurements,” *ArXiv e-prints*, 2016.
- [57] A. Kosowsky and A. Loeb, “Faraday rotation of microwave background polarization by a primordial magnetic field,” *Astrophys.J.*, vol. 469, pp. 1–6, 1996.
- [58] N. Oppermann *et al.*, “An improved map of the Galactic Faraday sky,” *Astron. Astrophys.*, vol. 542, p. A93, 2012.
- [59] S. De, L. Pogosian, and T. Vachaspati, “CMB Faraday rotation as seen through the Milky Way,” *Phys. Rev.*, vol. D88, no. 6, p. 063527, 2013.
- [60] L. Pogosian, “Searching for primordial magnetism with multifrequency cosmic microwave background experiments,” *Mon. Not. Roy. Astron. Soc.*, vol. 438, no. 3, pp. 2508–2512, 2014.
- [61] S. M. Carroll, “Quintessence and the Rest of the World: Suppressing Long-Range Interactions,” *Physical Review Letters*, vol. 81, pp. 3067–3070, Oct. 1998.
- [62] M. Kamionkowski, “How to De-Rotate the Cosmic Microwave Background Polarization,” *Phys. Rev. Lett.*, vol. 102, p. 111302, 2009.
- [63] V. Gluscevic, M. Kamionkowski, and A. Cooray, “De-Rotation of the Cosmic Microwave Background Polarization: Full-Sky Formalism,” *Phys. Rev.*, vol. D80, p. 023510, 2009.
- [64] R. R. Caldwell, V. Gluscevic, and M. Kamionkowski, “Cross-correlation of cosmological birefringence with CMB temperature,” *Phys. Rev. D.*, vol. 84, no. 4, p. 043504, Aug. 2011.
- [65] A. P. S. Yadav, R. Biswas, M. Su, and M. Zaldarriaga, “Constraining a spatially dependent rotation of the cosmic microwave background polarization,” *Phys. Rev. D.*, vol. 79, no. 12, pp. 123 009–+, Jun. 2009.
- [66] P. A. R. Ade *et al.*, “POLARBEAR Constraints on Cosmic Birefringence and Primordial Magnetic Fields,” *Phys. Rev.*, vol. D92, p. 123509, 2015.
- [67] V. Miranda, A. Lidz, C. H. Heinrich, and W. Hu, “CMB signatures of metal-free star formation and Planck 2015 polarization data,” *MNRAS*, vol. 467, pp. 4050–4056, Jun. 2017.
- [68] E. Calabrese, R. Hložek, N. Battaglia *et al.*, “Precision epoch of reionization studies with next-generation CMB experiments,” *JCAP*, vol. 8, p. 010, Aug. 2014.
- [69] R. A. Monsalve, A. E. E. Rogers, J. D. Bowman, and T. J. Mozdzen, “Results from EDGES High-band. I. Constraints on Phenomenological Models for the Global 21 cm Signal,” *Ap. J.*, vol. 847, p. 64, Sep. 2017.
- [70] X. Fan, M. A. Strauss, R. H. Becker *et al.*, “Constraining the Evolution of the Ionizing Background and the Epoch of Reionization with $z \sim 6$ Quasars. II. A Sample of 19 Quasars,” *Astronomical Journal*, vol. 132, pp. 117–136, Jul. 2006.
- [71] Planck Collaboration, R. Adam, N. Aghanim *et al.*, “Planck intermediate results. XLVII. Planck constraints on reionization history,” *Astron. Astrophys.*, vol. 596, p. A108, Dec. 2016.
- [72] K. M. Smith and S. Ferraro, “Detecting Patchy Reionization in the Cosmic Microwave Background,” *Physical Review Letters*, vol. 119, no. 2, p. 021301, Jul. 2017.
- [73] C. Dvorkin and K. M. Smith, “Reconstructing patchy reionization from the cosmic microwave background,” *Phys. Rev. D.*, vol. 79, no. 4, p. 043003, Feb. 2009.
- [74] Planck Collaboration, N. Aghanim, Y. Akrami *et al.*, “Planck 2018 results. VIII. Gravitational lensing,” *ArXiv e-prints*, Jul. 2018.
- [75] U. Seljak, “Extracting Primordial Non-Gaussianity without Cosmic Variance,” *Physical Review Letters*, vol. 102, no. 2, p. 021302, Jan. 2009.

- [76] M. Schmittfull and U. Seljak, “Parameter constraints from cross-correlation of CMB lensing with galaxy clustering,” *Phys. Rev. D.*, vol. 97, no. 12, p. 123540, Jun. 2018.
- [77] N. Dalal, O. Doré, D. Huterer, and A. Shirokov, “Imprints of primordial non-Gaussianities on large-scale structure: Scale-dependent bias and abundance of virialized objects,” *Phys. Rev. D.*, vol. 77, no. 12, p. 123514, Jun. 2008.
- [78] E. J. Baxter, R. Keisler, S. Dodelson *et al.*, “A Measurement of Gravitational Lensing of the Cosmic Microwave Background by Galaxy Clusters Using Data from the South Pole Telescope,” *Ap. J.*, vol. 806, p. 247, Jun. 2015.
- [79] M. Madhavacheril, N. Sehgal, R. Allison *et al.*, “Evidence of lensing of the cosmic microwave background by dark matter halos,” *Phys. Rev. Lett.*, vol. 114, p. 151302, Apr 2015. URL: <https://link.aps.org/doi/10.1103/PhysRevLett.114.151302>
- [80] Planck Collaboration, P. A. R. Ade, N. Aghanim *et al.*, “Planck 2015 results. XXIV. Cosmology from Sunyaev-Zeldovich cluster counts,” *Astron. Astrophys.*, vol. 594, p. A24, Sep. 2016.
- [81] J.-B. Melin and J. G. Bartlett, “Measuring cluster masses with CMB lensing: a statistical approach,” *Astron. Astrophys.*, vol. 578, p. A21, Jun. 2015.
- [82] Y. B. Zeldovich and R. A. Sunyaev, “The Interaction of Matter and Radiation in a Hot-Model Universe,” *ApSS*, vol. 4, pp. 301–316, Jul. 1969.
- [83] R. A. Sunyaev and Y. B. Zeldovich, “The Observations of Relic Radiation as a Test of the Nature of X-Ray Radiation from the Clusters of Galaxies,” *Comments on Astrophysics and Space Physics*, vol. 4, p. 173, Nov. 1972.
- [84] J. Delabrouille, J.-F. Cardoso, M. Le Jeune, M. Betoule, G. Fay, and F. Guilloux, “A full sky, low foreground, high resolution CMB map from WMAP,” *Astron. Astrophys.*, vol. 493, pp. 835–857, Jan. 2009.
- [85] J. L. Sievers, R. A. Hlozek, M. R. Nolta *et al.*, “The Atacama Cosmology Telescope: cosmological parameters from three seasons of data,” *JCAP*, vol. 10, p. 060, Oct. 2013.
- [86] E. M. George, C. L. Reichardt, K. A. Aird *et al.*, “A measurement of secondary cosmic microwave background anisotropies from the 2500 square-degree spt-sz survey,” *The Astrophysical Journal*, vol. 799, no. 2, p. 177, 2015. URL: <http://stacks.iop.org/0004-637X/799/i=2/a=177>
- [87] Planck Collaboration, R. Adam, P. A. R. Ade *et al.*, “Planck 2015 results. I. Overview of products and scientific results,” *Astron. Astrophys.*, vol. 594, p. A1, Sep. 2016.
- [88] Planck Collaboration, N. Aghanim, Y. Akrami *et al.*, “Planck 2018 results. XII. Galactic astrophysics using polarized dust emission,” *ArXiv e-prints*, p. arXiv:1807.06212, Jul. 2018.
- [89] D. T. Chuss, B.-G. Andersson, J. Bally *et al.*, “HAWC+/SOFIA Multiwavelength Polarimetric Observations of OMC-1,” *ArXiv e-prints*, p. arXiv:1810.08233, Oct. 2018.
- [90] B. S. Hensley and P. Bull, “Mitigating Complex Dust Foregrounds in Future Cosmic Microwave Background Polarization Experiments,” *Ap. J.*, vol. 853, p. 127, Feb. 2018.
- [91] C. H. Smith, C. M. Wright, D. K. Aitken, P. F. Roche, and J. H. Hough, “Studies in mid-infrared spectropolarimetry - II. An atlas of spectra,” *MNRAS*, vol. 312, pp. 327–361, Feb. 2000.
- [92] J. E. Chiar, A. J. Adamson, D. C. B. Whittet *et al.*, “Spectropolarimetry of the 3.4 μm Feature in the Diffuse ISM toward the Galactic Center Quintuplet Cluster,” *Ap. J.*, vol. 651, pp. 268–271, Nov. 2006.
- [93] R. E. Mason, G. S. Wright, A. Adamson, and Y. Pendleton, “Spectropolarimetry of the 3.4 μm Absorption Feature in NGC 1068,” *Ap. J.*, vol. 656, pp. 798–804, Feb. 2007.
- [94] Planck Collaboration Int. XXII, “Planck intermediate results. XXII. Frequency dependence of thermal emission from Galactic dust in intensity and polarization,” *Astron. Astrophys.*, vol. 576, p. A107, Apr. 2015.
- [95] P. C. Ashton, P. A. R. Ade, F. E. Angilè *et al.*, “First Observation of the Submillimeter Polarization Spectrum in a Translucent Molecular Cloud,” *Ap. J.*, vol. 857, p. 10, Apr. 2018.
- [96] A. M. Meisner and D. P. Finkbeiner, “Modeling Thermal Dust Emission with Two Components: Application to the Planck High Frequency Instrument Maps,” *Ap. J.*, vol. 798, p. 88, Jan. 2015.
- [97] V. Guillet, L. Fanciullo, L. Verstraete *et al.*, “Dust models compatible with Planck intensity and polarization data in translucent lines of sight,” *Astron. Astrophys.*, vol. 610, p. A16, Feb. 2018.
- [98] B. T. Draine and B. Hensley, “Magnetic Nanoparticles in the Interstellar Medium: Emission Spectrum and Polarization,” *Ap. J.*, vol. 765, p. 159, Mar. 2013.
- [99] C. F. McKee and E. C. Ostriker, “Theory of Star Formation,” *Ann. Rev. Astron. Astrophys.*, vol. 45, pp. 565–687, Sep. 2007.

- [100] R. M. Crutcher, B. Wandelt, C. Heiles, E. Falgarone, and T. H. Troland, “Magnetic Fields in Interstellar Clouds from Zeeman Observations: Inference of Total Field Strengths by Bayesian Analysis,” *Ap. J.*, vol. 725, pp. 466–479, Dec. 2010.
- [101] S. E. Clark, J. E. G. Peek, and M. E. Putman, “Magnetically Aligned H I Fibers and the Rolling Hough Transform,” *Ap. J.*, vol. 789, p. 82, Jul. 2014.
- [102] S. E. Clark, J. C. Hill, J. E. G. Peek, M. E. Putman, and B. L. Babler, “Neutral Hydrogen Structures Trace Dust Polarization Angle: Implications for Cosmic Microwave Background Foregrounds,” *Physical Review Letters*, vol. 115, no. 24, p. 241302, Dec. 2015.
- [103] P. M. W. Kalberla, J. Kerp, U. Haud, B. Winkel, N. Ben Bekhti, L. Flöer, and D. Lenz, “Cold Milky Way HI Gas in Filaments,” *Ap. J.*, vol. 821, p. 117, Apr. 2016.
- [104] P. M. W. Kalberla and J. Kerp, “Anisotropies in the HI gas distribution toward 3C 196,” *Astron. Astrophys.*, vol. 595, p. A37, Oct. 2016.
- [105] T. P. Ellsworth-Bowers, E. Rosolowsky, J. Glenn, A. Ginsburg, N. J. Evans, II, C. Battersby, Y. L. Shirley, and B. Svoboda, “The Bolocam Galactic Plane Survey. XII. Distance Catalog Expansion Using Kinematic Isolation of Dense Molecular Cloud Structures with $^{13}\text{CO}(1-0)$,” *Ap. J.*, vol. 799, p. 29, Jan. 2015.
- [106] J. D. Soler, P. Hennebelle, P. G. Martin, M.-A. Miville-Deschénes, C. B. Netterfield, and L. M. Fissel, “An Imprint of Molecular Cloud Magnetization in the Morphology of the Dust Polarized Emission,” *Ap. J.*, vol. 774, p. 128, Sep. 2013.
- [107] C.-Y. Chen, P. K. King, and Z.-Y. Li, “Change of Magnetic Field-gas Alignment at the Gravity-driven Alfvénic Transition in Molecular Clouds: Implications for Dust Polarization Observations,” *Ap. J.*, vol. 829, p. 84, Oct. 2016.
- [108] J. D. Soler, P. A. R. Ade, F. E. Angilè *et al.*, “The relation between the column density structures and the magnetic field orientation in the Vela C molecular complex,” *Astron. Astrophys.*, vol. 603, p. A64, Jul. 2017.
- [109] Planck Collaboration Int. XXXV, “*Planck* intermediate results. XXXV. Probing the role of the magnetic field in the formation of structure in molecular clouds,” *Astron. Astrophys.*, vol. 586, p. A138, 2016.
- [110] L. M. Fissel, P. A. R. Ade, F. E. Angilè *et al.*, “Balloon-Borne Submillimeter Polarimetry of the Vela C Molecular Cloud: Systematic Dependence of Polarization Fraction on Column Density and Local Polarization-Angle Dispersion,” *Ap. J.*, vol. 824, p. 134, Jun. 2016.
- [111] P. K. King, L. M. Fissel, C.-Y. Chen, and Z.-Y. Li, “Modelling dust polarization observations of molecular clouds through MHD simulations,” *MNRAS*, vol. 474, pp. 5122–5142, Mar. 2018.
- [112] D. F. González-Casanova and A. Lazarian, “Velocity Gradients as a Tracer for Magnetic Fields,” *Ap. J.*, vol. 835, p. 41, Jan. 2017.
- [113] K. H. Yuen and A. Lazarian, “Tracing Interstellar Magnetic Field Using Velocity Gradient Technique: Application to Atomic Hydrogen Data,” *Ap. J. Lett.*, vol. 837, p. L24, Mar. 2017.
- [114] A. Lazarian and K. H. Yuen, “Tracing Magnetic Fields with Spectroscopic Channel Maps,” *Ap. J.*, vol. 853, p. 96, Jan. 2018.
- [115] L. Davis, Jr. and J. L. Greenstein, “The Polarization of Starlight by Aligned Dust Grains.” *Ap. J.*, vol. 114, p. 206, Sep. 1951.
- [116] S. Chandrasekhar and E. Fermi, “Magnetic Fields in Spiral Arms.” *Ap. J.*, vol. 118, p. 113, Jul. 1953.
- [117] R. H. Hildebrand, L. Kirby, J. L. Dotson, M. Houde, and J. E. Vaillancourt, “Dispersion of Magnetic Fields in Molecular Clouds. I,” *Ap. J.*, vol. 696, pp. 567–573, May 2009.
- [118] M. Houde, J. E. Vaillancourt, R. H. Hildebrand, S. Chitsazzadeh, and L. Kirby, “Dispersion of Magnetic Fields in Molecular Clouds. II.” *Ap. J.*, vol. 706, pp. 1504–1516, Dec. 2009.
- [119] B. G. Andersson, A. Lazarian, and J. E. Vaillancourt, “Interstellar Dust Grain Alignment,” *Annual Review of Astronomy and Astrophysics*, vol. 53, pp. 501–539, Aug. 2015.
- [120] D. Seifried, S. Walch, S. Reissl, and J. C. Ibáñez-Mejía, “SILCC-Zoom: Polarisation and depolarisation in molecular clouds,” *MNRAS*, Oct. 2018.
- [121] M.-A. Miville-Deschénes, N. Murray, and E. J. Lee, “Physical Properties of Molecular Clouds for the Entire Milky Way Disk,” *Ap. J.*, vol. 834, p. 57, Jan. 2017.
- [122] HI4PI Collaboration, “HI4PI: A full-sky H I survey based on EBHIS and GASS,” *Astron. Astrophys.*, vol. 594, p. A116, Oct. 2016.
- [123] J. E. G. Peek, B. L. Babler, Y. Zheng *et al.*, “The GALFA-H I Survey Data Release 2,” *Ap. J. Suppl.*, vol. 234,

p. 2, Jan. 2018.

- [124] N. M. McClure-Griffiths, S. Stanimirovic, C. Murray *et al.*, “Galactic and Magellanic Evolution with the SKA,” in *Advancing Astrophysics with the Square Kilometre Array (AASKA14)*, Apr. 2015, p. 130.
- [125] A. Allen, Z.-Y. Li, and F. H. Shu, “Collapse of Magnetized Singular Isothermal Toroids. II. Rotation and Magnetic Braking,” *Ap. J.*, vol. 599, pp. 363–379, Dec. 2003.
- [126] Z.-Y. Li, R. Krasnopolsky, H. Shang, and B. Zhao, “On the Role of Pseudodisk Warping and Reconnection in Protostellar Disk Formation in Turbulent Magnetized Cores,” *Ap. J.*, vol. 793, p. 130, Oct. 2014.
- [127] S. Xu and A. Lazarian, “Magnetohydrodynamic turbulence and turbulent dynamo in a partially ionized plasma,” *New Journal of Physics*, Oct. 2018.
- [128] A. Lazarian, “Enhancement and Suppression of Heat Transfer by MHD Turbulence,” *Ap. J. Lett.*, vol. 645, pp. L25–L28, Jul. 2006.
- [129] A. Lazarian, “Damping of Alfvén Waves by Turbulence and Its Consequences: From Cosmic-ray Streaming to Launching Winds,” *Ap. J.*, vol. 833, p. 131, Dec. 2016.
- [130] A. Lazarian and E. T. Vishniac, “Reconnection in a Weakly Stochastic Field,” *Ap. J.*, vol. 517, pp. 700–718, Jun. 1999.
- [131] Planck Collaboration XXVI, “Planck 2015 results. XXVI. The Second Planck Catalogue of Compact Sources,” *Astron. Astrophys.*, vol. 594, p. A26, Sep. 2016.
- [132] A. M. Swinbank, I. Smail, S. Longmore *et al.*, “Intense star formation within resolved compact regions in a galaxy at $z = 2.3$,” *Nature*, vol. 464, pp. 733–736, Apr. 2010.
- [133] F. Combes, M. Rex, T. D. Rawle *et al.*, “A bright $z = 5.2$ lensed submillimeter galaxy in the field of Abell 773. HLSJ091828.6+514223,” *Astron. Astrophys.*, vol. 538, p. L4, Feb. 2012.
- [134] M. Negrello, S. Amber, A. Amvrosiadis *et al.*, “The Herschel-ATLAS: a sample of 500 μm -selected lensed galaxies over 600 deg^2 ,” *MNRAS*, vol. 465, pp. 3558–3580, Mar. 2017.
- [135] M. Negrello, J. Gonzalez-Nuevo, G. De Zotti *et al.*, “On the statistics of proto-cluster candidates detected in the Planck all-sky survey,” *ArXiv e-prints*, May 2017.
- [136] J. Silk and G. A. Mamon, “The current status of galaxy formation,” *Research in Astronomy and Astrophysics*, vol. 12, pp. 917–946, Aug. 2012.
- [137] R. S. Somerville and R. Davé, “Physical Models of Galaxy Formation in a Cosmological Framework,” *ARAA*, vol. 53, pp. 51–113, Aug. 2015.
- [138] S. Fujimoto, M. Ouchi, K. Kohno *et al.*, “ALMA 26 Arcmin 2 Survey of GOODS-S at One Millimeter (ASAGAO): Average Morphology of High- z Dusty Star-forming Galaxies in an Exponential Disk ($n \simeq 1$),” *Ap. J.*, vol. 861, p. 7, Jul. 2018.
- [139] R. Cañameras, N. Nesvadba, R. Kneissl *et al.*, “Planck’s dusty GEMS. IV. Star formation and feedback in a maximum starburst at $z = 3$ seen at 60-pc resolution,” *Astron. Astrophys.*, vol. 604, p. A117, Aug. 2017.
- [140] S. Dye, C. Furlanetto, L. Dunne *et al.*, “Modelling high-resolution ALMA observations of strongly lensed highly star-forming galaxies detected by Herschel,” *MNRAS*, vol. 476, pp. 4383–4394, Jun. 2018.
- [141] C. Lamarche, A. Verma, A. Vishwas *et al.*, “Resolving Star Formation on Sub-Kiloparsec Scales in the High-Redshift Galaxy SDP.11 Using Gravitational Lensing,” *ArXiv e-prints*, Sep. 2018.
- [142] P. Sharda, C. Federrath, E. da Cunha, A. M. Swinbank, and S. Dye, “Testing star formation laws in a starburst galaxy at redshift 3 resolved with ALMA,” *MNRAS*, vol. 477, pp. 4380–4390, Jul. 2018.
- [143] J. S. Spilker, M. Aravena, M. Béthermin *et al.*, “Fast molecular outflow from a dusty star-forming galaxy in the early Universe,” *Science*, vol. 361, pp. 1016–1019, Sep. 2018.
- [144] T. Treu, “Strong Lensing by Galaxies,” *Ann. Rev. Astr. Ap.*, vol. 48, pp. 87–125, Sep. 2010.
- [145] M. Negrello, R. Hopwood, G. De Zotti *et al.*, “The Detection of a Population of Submillimeter-Bright, Strongly Lensed Galaxies,” *Science*, vol. 330, p. 800, Nov. 2010.
- [146] R. A. Overzier, “The realm of the galaxy protoclusters. A review,” *Astron. Astrophys. Rev.*, vol. 24, p. 14, Nov. 2016.
- [147] Planck Collaboration XXXIX, “Planck intermediate results. XXXIX. The Planck list of high-redshift source candidates,” *Astron. Astrophys.*, vol. 596, p. A100, Dec. 2016.
- [148] R. J. Ivison, A. M. Swinbank, I. Smail *et al.*, “Herschel-ATLAS: A Binary HyLIRG Pinpointing a Cluster of Starbursting Protoellipticals,” *Ap. J.*, vol. 772, p. 137, Aug. 2013.
- [149] T. Wang, D. Elbaz, E. Daddi *et al.*, “Discovery of a Galaxy Cluster with a Violently Starbursting Core at $z =$

2.506,” *Ap. J.*, vol. 828, p. 56, Sep. 2016.

- [150] I. Oteo, R. J. Ivison, L. Dunne *et al.*, “An Extreme Protocluster of Luminous Dusty Starbursts in the Early Universe,” *Ap. J.*, vol. 856, p. 72, Mar. 2018.
- [151] B. D. Metzger, P. K. G. Williams, and E. Berger, “Extragalactic Synchrotron Transients in the Era of Wide-field Radio Surveys. I. Detection Rates and Light Curve Characteristics,” *Ap. J.*, vol. 806, p. 224, Jun. 2015.
- [152] Planck Collaboration, P. A. R. Ade, N. Aghanim *et al.*, “Planck 2013 results. XXX. Cosmic infrared background measurements and implications for star formation,” *Astronomy and Astrophysics*, vol. 571, p. A30, Nov. 2014.
- [153] Planck Collaboration, P. A. R. Ade, N. Aghanim *et al.*, “Planck 2013 results. XVIII. The gravitational lensing-infrared background correlation,” *Astronomy and Astrophysics*, vol. 571, p. A18, Nov. 2014.
- [154] P. Madau and M. Dickinson, “Cosmic Star-Formation History,” *ARA&A*, vol. 52, pp. 415–486, Aug. 2014.
- [155] H.-Y. Wu and O. DorÃ©, “Optimizing future experiments of cosmic far-infrared background: a principal component approach,” *Mon. Not. Roy. Astron. Soc.*, vol. 467, no. 4, pp. 4150–4160, 2017.
- [156] J. H. Kang, P. Ade, Z. Ahmed *et al.*, “2017 upgrade and performance of bicep3: a 95ghz refracting telescope for degree-scale cmb polarization,” in *Millimeter, Submillimeter, and Far-Infrared Detectors and Instrumentation for Astronomy IX*, vol. 10708. International Society for Optics and Photonics, 2018, p. 107082N.
- [157] A. S. Rahlin, P. A. R. Ade, M. Amiri *et al.*, “Pre-flight integration and characterization of the SPIDER balloon-borne telescope,” in *Millimeter, Submillimeter, and Far-Infrared Detectors and Instrumentation for Astronomy VII*, ser. SPIE Proceedings, vol. 9153, Jul. 2014, p. 915313.
- [158] N. Krachmalnicoff, E. Carretti, C. Baccigalupi *et al.*, “The S-PASS view of polarized Galactic Synchrotron at 2.3 GHz as a contaminant to CMB observations,” *ArXiv e-prints*, p. arXiv:1802.01145, Feb. 2018.
- [159] U. Fuskeland, I. K. Wehus, H. K. Eriksen, and S. K. Næss, “Spatial Variations in the Spectral Index of Polarized Synchrotron Emission in the 9 yr WMAP Sky Maps,” *Ap. J.*, vol. 790, p. 104, Aug. 2014.
- [160] Planck Collaboration, A. Abergel, P. A. R. Ade *et al.*, “Planck 2013 results. XI. All-sky model of thermal dust emission,” *Astron. Astrophys.*, vol. 571, p. A11, Nov. 2014.
- [161] T. Trombetti, C. Burigana, G. De Zotti, V. Galluzzi, and M. Massardi, “Average fractional polarization of extragalactic sources at Planck frequencies,” *Astron. Astrophys.*, vol. 618, p. A29, Oct. 2018.
- [162] G. Puglisi, V. Galluzzi, L. Bonavera *et al.*, “Forecasting the Contribution of Polarized Extragalactic Radio Sources in CMB Observations,” *Ap. J.*, vol. 858, p. 85, May 2018.
- [163] Y. Fantaye, F. Stivoli, J. Grain, S. M. Leach, M. Tristram, C. Baccigalupi, and R. Stompor, “Estimating the tensor-to-scalar ratio and the effect of residual foreground contamination,” *JCAP*, vol. 8, p. 1, Aug. 2011.
- [164] C. Armitage-Caplan, J. Dunkley, H. K. Eriksen, and C. Dickinson, “Impact on the tensor-to-scalar ratio of incorrect Galactic foreground modelling,” *MNRAS*, vol. 424, pp. 1914–1924, Aug. 2012.
- [165] A. Kogut and D. J. Fixsen, “Foreground Bias from Parametric Models of Far-IR Dust Emission,” *Ap. J.*, vol. 826, p. 101, Aug. 2016.
- [166] M. Remazeilles, C. Dickinson, H. K. K. Eriksen, and I. K. Wehus, “Sensitivity and foreground modelling for large-scale cosmic microwave background B-mode polarization satellite missions,” *MNRAS*, vol. 458, pp. 2032–2050, May 2016.
- [167] R. Stompor, J. Errard, and D. Poletti, “Forecasting performance of CMB experiments in the presence of complex foreground contaminations,” *Phys. Rev. D.*, vol. 94, no. 8, p. 083526, Oct. 2016.
- [168] B. Thorne, J. Dunkley, D. Alonso, and S. Næss, “The Python Sky Model: software for simulating the Galactic microwave sky,” *MNRAS*, vol. 469, pp. 2821–2833, Aug. 2017.
- [169] K. M. Górski, E. Hivon, A. J. Banday, B. D. Wandelt, F. K. Hansen, M. Reinecke, and M. Bartelmann, “HEALPix: A Framework for High-Resolution Discretization and Fast Analysis of Data Distributed on the Sphere,” *Ap. J.*, vol. 622, pp. 759–771, Apr. 2005.
- [170] J. Delabrouille, M. Betoule, J. B. Melin *et al.*, “The pre-launch Planck Sky Model: a model of sky emission at submillimetre to centimetre wavelengths,” *Astron. Astrophys.*, vol. 553, p. A96, May 2013.
- [171] J. Errard, S. M. Feeney, H. V. Peiris, and A. H. Jaffe, “Robust forecasts on fundamental physics from the foreground-obscured, gravitationally-lensed CMB polarization,” *JCAP*, vol. 3, p. 052, Mar. 2016.
- [172] W. Hu, M. M. Hedman, and M. Zaldarriaga, “Benchmark parameters for CMB polarization experiments,” *Phys. Rev. D.*, vol. 67, pp. 043 004–+, Feb. 2003, astro-ph/0210096.
- [173] M. Shimon, B. Keating, N. Ponthieu, and E. Hivon, “CMB polarization systematics due to beam asymmetry: Impact on inflationary science,” *Phys. Rev. D.*, vol. 77, no. 8, pp. 083 003–+, Apr. 2008.

- [174] A. P. S. Yadav, M. Su, and M. Zaldarriaga, “Primordial B-mode diagnostics and self-calibrating the CMB polarization,” *Phys. Rev. D.*, vol. 81, no. 6, pp. 063512–+, Mar. 2010.
- [175] Y. D. Takahashi, P. A. R. Ade, D. Barkats *et al.*, “Characterization of the BICEP Telescope for High-precision Cosmic Microwave Background Polarimetry,” *Ap. J.*, vol. 711, pp. 1141–1156, Mar. 2010.
- [176] Bicep2 Collaboration, P. A. R. Ade, R. W. Aikin *et al.*, “Bicep2 III: Instrumental Systematics,” *Ap. J.*, vol. 814, p. 110, Dec. 2015.
- [177] C. L. Bennett, D. Larson, J. L. Weiland *et al.*, “Nine-year Wilkinson Microwave Anisotropy Probe (WMAP) Observations: Final Maps and Results,” *The Astrophysical Journal Supplement Series*, vol. 208, p. 20, Oct. 2013.
- [178] M. Hazumi, J. Borrill, Y. Chinone *et al.*, “LiteBIRD: a small satellite for the study of B-mode polarization and inflation from cosmic background radiation detection,” in *Space Telescopes and Instrumentation 2012: Optical, Infrared, and Millimeter Wave*, vol. 8442, Sep. 2012, p. 844219.
- [179] C. G. R. Wallis, M. L. Brown, R. A. Battye, and J. Delabrouille, “Optimal scan strategies for future CMB satellite experiments,” *Monthly Notices of the Royal Astronomical Society*, vol. 466, no. 1, pp. 425–442, 2017. URL: <http://dx.doi.org/10.1093/mnras/stw2577>
- [180] P. Natoli, M. Ashdown, R. Banerji *et al.*, “Exploring cosmic origins with CORE: Mitigation of systematic effects,” *Journal of Cosmology and Astro-Particle Physics*, vol. 2018, p. 022, Apr. 2018.
- [181] Planck Collaboration, P. A. R. Ade, N. Aghanim *et al.*, “Planck 2015 results. XII. Full focal plane simulations,” *Astron. Astrophys.*, vol. 594, p. A12, Sep. 2016.
- [182] L. Pogosian and A. Zucca, “Searching for primordial magnetic fields with CMB B-modes,” *Classical and Quantum Gravity*, vol. 35, no. 12, p. 124004, May 2018.
- [183] Planck collaboration, “Planck intermediate results. XLIX. Parity-violation constraints from polarization data,” *Astronomy and Astrophysics*, vol. 596, p. A110, Dec. 2016.
- [184] C. Rosset, M. Tristram, N. Ponthieu *et al.*, “Planck pre-launch status: High Frequency Instrument polarization calibration,” *A&A*, vol. 520, pp. A13+, Sep. 2010.
- [185] J. Aumont, J. F. Macías-Pérez, A. Ritacco, N. Ponthieu, and A. Mangilli, “Absolute calibration of the polarisation angle for future CMB B-mode experiments from current and future measurements of the Crab nebula,” *ArXiv e-prints*, May 2018.
- [186] Planck Collaboration, Y. Akrami, F. Argüeso *et al.*, “Planck 2018 results. II. Low Frequency Instrument data processing,” *ArXiv e-prints*, Jul. 2018.
- [187] K. Young, M. Alvarez, N. Battaglia *et al.*, “Optical design of PICO: a concept for a space mission to probe inflation and cosmic origins,” in *Society of Photo-Optical Instrumentation Engineers (SPIE) Conference Series*, vol. 10698, Aug. 2018, p. 1069846.
- [188] P. de Bernardis, P. A. R. Ade, J. J. A. Baselmans *et al.*, “Exploring cosmic origins with CORE: The instrument,” *Journal of Cosmology and Astro-Particle Physics*, vol. 2018, p. 015, Apr. 2018.
- [189] A. Suzuki, K. Arnold, J. Edwards *et al.*, “Multi-Chroic Dual-Polarization Bolometric Detectors for Studies of the Cosmic Microwave Background,” *Journal of Low Temperature Physics*, vol. 176, pp. 650–656, Sep. 2014.
- [190] R. Datta, J. Hubmayr, C. Munson *et al.*, “Horn Coupled Multichroic Polarimeters for the Atacama Cosmology Telescope Polarization Experiment,” *Journal of Low Temperature Physics*, vol. 176, pp. 670–676, Sep. 2014.
- [191] S. M. Duff, J. Austermann, J. A. Beall *et al.*, “Advanced ACTPol Multichroic Polarimeter Array Fabrication Process for 150 mm Wafers,” *Journal of Low Temperature Physics*, vol. 184, pp. 634–641, Aug. 2016.
- [192] BICEP2 Collaboration, Keck Array Collaboration, SPIDER Collaboration *et al.*, “Antenna-coupled TES Bolometers Used in BICEP2, Keck Array, and Spider,” *Ap. J.*, vol. 812, p. 176, Oct. 2015.
- [193] J. M. Edwards, R. O’Brien, A. T. Lee, and G. M. Rebeiz, “Dual-Polarized Sinuous Antennas on Extended Hemispherical Silicon Lenses,” *IEEE Transactions on Antennas and Propagation*, vol. 60, pp. 4082–4091, Sep. 2012.
- [194] R. O’Brien, P. Ade, K. Arnold *et al.*, “A dual-polarized broadband planar antenna and channelizing filter bank for millimeter wavelengths,” *Applied Physics Letters*, vol. 102, no. 6, p. 063506, Feb. 2013.
- [195] E. D. Shirokoff, “The South Pole Telescope bolometer array and the measurement of secondary Cosmic Microwave Background anisotropy at small angular scales,” Ph.D. dissertation, University of California, Berkeley, Jan. 2011.
- [196] L. Bleem, P. Ade, K. Aird *et al.*, “An Overview of the SPTpol Experiment,” *Journal of Low Temperature*

- Physics*, vol. 167, pp. 859–864, Jun. 2012.
- [197] A. D. Turner, J. J. Bock, J. W. Beeman *et al.*, “Silicon nitride Micromesh Bolometer Array for Submillimeter Astrophysics,” *Appl. Optics*, vol. 40, pp. 4921–4932, Oct. 2001.
- [198] A. D. Beyer, M. E. Kenyon, P. M. Echternach *et al.*, “Ultra-sensitive transition-edge sensors for the background limited infrared/sub-mm spectrograph (BLISS),” *Journal of Low Temperature Physics*, vol. 167, pp. 182–187, May 2012.
- [199] A. S. Rahlin, P. A. R. Ade, M. Amiri *et al.*, “Pre-flight integration and characterization of the SPIDER balloon-borne telescope,” in *Millimeter, Submillimeter, and Far-Infrared Detectors and Instrumentation for Astronomy VII*, vol. 9153, Jul. 2014, p. 915313.
- [200] S. W. Henderson, R. Allison, J. Austermann *et al.*, “Advanced ACTPol Cryogenic Detector Arrays and Readout,” *Journal of Low Temperature Physics*, vol. 184, pp. 772–779, Aug. 2016.
- [201] H. Hui, P. A. R. Ade, Z. Ahmed *et al.*, “BICEP Array: a multi-frequency degree-scale CMB polarimeter,” in *Society of Photo-Optical Instrumentation Engineers (SPIE) Conference Series*, vol. 10708, Jul. 2018, p. 1070807.
- [202] The EBEX Collaboration, A. Aboobaker, P. Ade *et al.*, “The EBEX Balloon-borne Experiment—Gondola, Attitude Control, and Control Software,” *The Astrophysical Journal Supplement Series*, vol. 239, p. 9, Nov. 2018.
- [203] F. Pajot, “Planck compression,” Private communication.
- [204] Planck HFI Core Team, P. A. R. Ade, N. Aghanim *et al.*, “Planck early results. IV. First assessment of the High Frequency Instrument in-flight performance,” *Astron. Astrophys.*, vol. 536, p. A4, Dec. 2011.
- [205] M. Donabedian, A. I. of Aeronautics, and Astronautics, *Spacecraft Thermal Control Handbook, Vol. 2: Cryogenics*, ser. EngineeringPro collection. Aerospace Press, 2003. URL: <https://books.google.com/books?id=nsLqjwEACAAJ>
- [206] R. G. Ross, “Estimation of thermal conduction loads for structural supports of cryogenic spacecraft assemblies,” *Cryogenics*, vol. 44, pp. 421–424, Jun. 2004.
- [207] P. J. Shirron, M. O. Kimball, D. J. Fixsen, A. J. Kogut, X. Li, and M. J. DiPirro, “Design of the PIXIE adiabatic demagnetization refrigerators,” *Cryogenics*, vol. 52, pp. 140–144, Apr. 2012.
- [208] P. J. Shirron, M. O. Kimball, B. L. James *et al.*, “Thermodynamic performance of the 3-stage ADR for the Astro-H Soft-X-ray Spectrometer instrument,” *Cryogenics*, vol. 74, pp. 24–30, Mar. 2016.
- [209] D. Durand, R. Colbert, C. Jaco, M. Michaelian, T. Nguyen, M. Petach, and J. Raab, “Mid Infrared Instrument (miri) Cooler Subsystem Prototype Demonstration,” in *Advances in Cryogenic Engineering*, ser. American Institute of Physics Conference Series, J. G. Weisend, J. Barclay, S. Breon *et al.*, Eds., vol. 52, Mar. 2008, pp. 807–814.
- [210] J. Rabb, “Ngas scw-4k,” Presentation at the 2013 Space Cryogenics Workshop, 2013.
- [211] D. S. Glaister, W. Gully, R. Ross, P. Hendershott, E. Marquardt, and V. Kotsubo, “Ball Aerospace 4-6 K Space Cryocooler,” in *Advances in Cryogenic Engineering: Transactions of the Cryogenic Engineering Conference*, ser. American Institute of Physics Conference Series, I. Weisend, J. G., J. Barclay, S. Breon *et al.*, Eds., vol. 823, Apr. 2006, pp. 632–639.
- [212] F. Pajot, P. A. R. Ade, J. L. Beney *et al.*, “Planck pre-launch status: HFI ground calibration,” *Astron. Astrophys.*, vol. 520, p. A10, Sep. 2010.
- [213] C. L. Bennett, M. Bay, M. Halpern *et al.*, “The Microwave Anisotropy Probe Mission,” *Ap. J.*, vol. 583, pp. 1–23, Jan. 2003.
- [214] J. A. Tauber, H. U. Nørgaard-Nielsen, P. A. R. Ade *et al.*, “Planck pre-launch status: The optical system,” *Astronomy and Astrophysics*, vol. 520, p. A2, Sep. 2010.
- [215] Space Exploration Technologies Corp., *Falcon 9 Launch Vehicle: Payload User’s Guide, Rev 2*. Space Exploration Technologies Corp., October 2015. URL: https://www.spacex.com/sites/spacex/files/falcon_9_users_guide_rev_2.0.pdf
- [216] W. Hu, M. M. Hedman, and M. Zaldarriaga, “Benchmark parameters for CMB polarization experiments,” *Phys. Rev. D.*, vol. 67, p. 043004, Feb. 2003.
- [217] H. Kurki-Suonio, E. Keihänen, R. Keskitalo, T. Poutanen, A. S. Sirviö, D. Maino, and C. Burigana, “Destriping CMB temperature and polarization maps,” *Astron. Astrophys.*, vol. 506, pp. 1511–1539, Nov. 2009.
- [218] Deep Space Network, Jet Propulsion Laboratory, California Institute of Technology, “Deep space network

- services catalog 820-100, rev. f.” February 2015. URL: <https://deepspace.jpl.nasa.gov/files/820-100-F1.pdf>
- [219] R. Gualtieri, J. P. Filippini, P. A. R. Ade *et al.*, “SPIDER: CMB Polarimetry from the Edge of Space,” *Journal of Low Temperature Physics*, Oct. 2018.
- [220] M. H. Abitbol, Z. Ahmed, D. Barron *et al.*, “CMB-S4 Technology Book, First Edition,” *ArXiv e-prints*, Jun. 2017.
- [221] W. S. Holland, D. Bintley, E. L. Chapin *et al.*, “SCUBA-2: the 10 000 pixel bolometer camera on the James Clerk Maxwell Telescope,” *MNRAS*, vol. 430, pp. 2513–2533, Apr. 2013.
- [222] D. Dutcher, P. A. R. Ade, Z. Ahmed *et al.*, “Characterization and performance of the second-year SPT-3G focal plane,” in *Society of Photo-Optical Instrumentation Engineers (SPIE) Conference Series*, vol. 10708, Jul. 2018, p. 107081Z.
- [223] Y. Li, J. E. Austermann, J. A. Beall *et al.*, “Performance of the advanced ACTPol low frequency array,” in *Society of Photo-Optical Instrumentation Engineers (SPIE) Conference Series*, vol. 10708, Jul. 2018, p. 107080A.
- [224] Keck Array and BICEP2 Collaborations, P. A. R. Ade, Z. Ahmed *et al.*, “BICEP2 / Keck Array X: Constraints on Primordial Gravitational Waves using Planck, WMAP, and New BICEP2/Keck Observations through the 2015 Season,” *ArXiv e-prints*, p. arXiv:1810.05216, Oct. 2018. URL: <https://arxiv.org/abs/1810.05216>
- [225] B. Westbrook, A. Cukierman, A. Lee, A. Suzuki, C. Raum, and W. Holzapfel, “Development of the Next Generation of Multi-chroic Antenna-Coupled Transition Edge Sensor Detectors for CMB Polarimetry,” *Journal of Low Temperature Physics*, vol. 184, pp. 74–81, Jul. 2016.
- [226] S. M. Simon, J. E. Golec, A. Ali *et al.*, “Feedhorn development and scalability for Simons Observatory and beyond,” in *Society of Photo-Optical Instrumentation Engineers (SPIE) Conference Series*, vol. 10708, Jul. 2018, p. 107084B.
- [227] J. T. Sayre, P. Ade, K. A. Aird *et al.*, “Design and characterization of 90 GHz feedhorn-coupled TES polarimeter pixels in the SPTPol camera,” in *Millimeter, Submillimeter, and Far-Infrared Detectors and Instrumentation for Astronomy VI*, vol. 8452, Sep. 2012, p. 845239.
- [228] B. Dober, D. T. Becker, D. A. Bennett *et al.*, “Microwave SQUID multiplexer demonstration for cosmic microwave background imagers,” *Applied Physics Letters*, vol. 111, p. 243510, Dec. 2017.
- [229] K. D. Irwin and K. W. Lehnert, “Microwave SQUID multiplexer,” *Applied Physics Letters*, vol. 85, p. 2107, Sep. 2004.
- [230] H. McCarrick, M. H. Abitbol, P. A. R. Ade *et al.*, “Development of dual-polarization LEKIDs for CMB observations,” in *Millimeter, Submillimeter, and Far-Infrared Detectors and Instrumentation for Astronomy VIII*, vol. 9914, Jul. 2016, p. 99140O.
- [231] B. A. Steinbach, J. J. Bock, H. T. Nguyen, R. C. O’Brient, and A. D. Turner, “Thermal Kinetic Inductance Detectors for Ground-Based Millimeter-Wave Cosmology,” *Journal of Low Temperature Physics*, vol. 193, pp. 88–95, Nov. 2018.
- [232] P. Gloesener, “Large Aluminium Convex Mirror for the Cryo-Optical Test of the Planck Primary Reflector,” in *ESA Special Publication*, vol. 621, Jun. 2006, p. 43.
- [233] Y. Toulemont, T. Passvogel, G. Pillbrat, D. de Chambure, D. Pierot, and D. Castel, “The 3.5m all SiC telescope for Herschel,” in *5th International Conference on Space Optics*, B. Warmbein, Ed., vol. 554, Jun. 2004, pp. 341–348.
- [234] Planck Collaboration, P. A. R. Ade, N. Aghanim *et al.*, “Planck early results. II. The thermal performance of Planck,” *Astron. Astrophys.*, vol. 536, p. A2, Dec. 2011.
- [235] S. Bard, “Development of a High-Performance Cryogenic Radiator with V-Groove Radiation Shields,” *Journal of Spacecraft and Rockets*, vol. 24, pp. 193–197, May 1987.
- [236] European Space Agency, “Planck cooling system,” September 2009. URL: <http://sci.esa.int/planck/45498-cooling-system/?fbodylongid=2123>
- [237] T. S. Brown, *A GNC Perspective of the Launch and Commissioning of NASA’s New SMAP (Soil Moisture Active Passive) Spacecraft*. American Institute of Aeronautics and Astronautics, 2018/11/19 2016. URL: <https://doi.org/10.2514/6.2016-0479>
- [238] European Space Agency, “Cmb polarisation mission study – cdf summary presentation,” May 2016. URL: <http://sci.esa.int/trs/57803-cmb-polarisation-study---cdf-summary-presentation/>
- [239] L. E. Z. Jasper and P. Xaypraseuth, “Data production on past and future nasa missions,” in *2017 IEEE Aerospace Conference*, March 2017, pp. 1–11.

- [240] J. Mrozinski and M. DiNicola, “NICM: Cryocooler,” NASA 2017 Cost Symposium Presentations, August 2017. URL: https://www.nasa.gov/offices/ocfo/cost_symposium/2017_presentations
- [241] H. P. Stahl and T. Henrichs, “Multivariable parametric cost model for space and ground telescopes,” in *Modeling, Systems Engineering, and Project Management for Astronomy VI*, ser. Society of Photo-Optical Instrumentation Engineers (SPIE) Conference Series, vol. 9911, Sep. 2016, p. 99110L.

DRAFT